First measurements of OH-C exchange and temperature-dependent partitioning of OH and halogens in the system apatite – silicate melt

Jenny Riker[1,2], Madeleine C.S. Humphreys[1*], Richard A. Brooker[2], Jan C.M. De Hoog[3] and EIMF[3]

REVISION 2

[1] Department of Earth Sciences, Durham University, Science Labs, Durham, DH1 3LE, United Kingdom

[2] Department of Earth Sciences, University of Bristol, Queen's Road, Bristol, BS8 1RJ, United Kingdom

[3] Edinburgh Ion Microprobe Facility, School of GeoSciences, University of Edinburgh, The King's Buildings, James Hutton Road, Edinburgh, EH9 3FE, United Kingdom

* Corresponding author: madeleine.humphreys@durham.ac.uk

Keywords: Apatite; volatiles; partitioning; carbon; halogens; water

ABSTRACT

We present the first integrated study of carbonate, hydroxyl, fluoride and chloride ion partitioning in the apatite-melt system. We determined volatile partitioning behaviour between apatite and silicate melt for both haplobasaltic andesite and trachyte bulk compositions at 0.5-1 GPa and 1250 °C using the piston cylinder apparatus. All volatile species were analysed directly in both apatite and glass using secondary ion mass spectrometry (SIMS) and electron probe microanalysis. Distribution coefficients for OH-halogen exchange are similar to those from previous studies, and together with literature

data, reveal a significant log-linear relationship with temperature, while the effects of pressure and melt composition are minimal. Meanwhile, halogen-free experiments generate very high C contents (up to 5000 ppm) in apatite. Stoichiometry calculations and infrared spectra indicate that this C is mainly incorporated onto the channel volatile site together with hydroxyl. In halogen-bearing experiments, apatite crystals contain significantly lower C ($\leq$ 500 ppm) which may be partly incorporated onto the phosphate site while the channel volatile site is filled by OH+F+Cl+C. Our experiments give the first constraints on H_2O-CO_2 exchange between apatite and silicate melt, with a K_D of 0.355 ± 0.05 for the trachyte and 0.629 ± 0.08 for the haplobasaltic andesite. The new constraints on the temperature-dependence of partitioning will enable quantitative modelling of apatite-volatile exchange in igneous systems, while this new partitioning data and method for direct, *in situ* analysis of C in apatite mark a significant advance that will permit future studies of magmatic C and other volatiles. This has a broad range of potential applications including magmatic differentiation, fractionation, and degassing; quantification of volatile budgets in extra-terrestrial and deep earth environments; and mineralisation processes.

INTRODUCTION

Volatile-bearing minerals such as apatite represent a useful source of information about the volatile compositions of the systems from which they crystallise. Apatite has a very flexible mineral structure and igneous apatites can accommodate all the major volatile species of magmatic importance, i.e. H, C, F, Cl and S, as well as other trace volatile species such as Br and I (e.g. Peng et al. 1997; Pan and Fleet 2002; Marks et al. 2012;

48 Konecke et al. 2017). With some knowledge of the partitioning properties of these
49 volatiles, apatite may therefore be able to provide quantitative information about multi-
50 component degassing, and other processes, in terrestrial magmas. The apatite crystal
51 formula is $Ca_5(PO_4)_3X$, where X represents the channel volatile site that runs parallel to
52 the crystallographic c-axis and is typically occupied by OH, F and Cl. While there are
53 several existing studies focusing on exchange between OH and halogens in the channel
54 site (e.g. Mathez and Webster 2005; Webster et al. 2009, 2017; Doherty et al. 2014; Li
55 and Hermann 2015, 2017; McCubbin et al. 2015; Potts et al. 2015), we are not aware of
56 any previous work quantitatively examining the partitioning behaviour of C between
57 apatite and a silicate melt. Knowledge of the C partitioning behaviour would be
58 particularly valuable for studies of terrestrial volcanism because magmatic CO_2 contents
59 are difficult to infer using traditional methods such as melt inclusions. The solubility of
60 CO_2 in silicate melts is strongly dependent on pressure, which means that CO_2 is typically
61 degassed very early during the magma ascent, and the highest (primary) CO_2 contents are
62 generally thought not to be trapped in melt inclusions or are lost to shrinkage bubbles
63 (e.g. Bureau et al. 1999; Wallace 2005; Blundy et al. 2010; Hartley et al. 2014; Moore et
64 al. 2015; Wallace et al. 2015; Aster et al. 2016). Furthermore, it is commonly not clear as
65 to the extent to which melt inclusions have been affected either by post-entrapment
66 diffusive modification (e.g. Gaetani et al. 2012) or by fluxing of CO_2-rich fluids through
67 the magma reservoir during entrapment (e.g. Spilliaert et al. 2006; Collins et al. 2009;
68 Blundy et al. 2010). The existing work on quantitative determination of carbonate
69 contents of apatite is based on FTIR using doubly polished, oriented wafers. This level of
70 sample preparation is almost prohibitively difficult for magmatic apatites, which are

typically small microphenocrysts or inclusions in other magmatic mineral phases. Here we successfully determine C in apatite using secondary ion mass spectrometry, and present data from a series of high pressure, high temperature experiments allowing us to constrain the combined partitioning behaviour of H, C, F, and Cl between apatite and silicate melts.

EXPERIMENTAL METHODS

Our experimental approach was to examine volatile partitioning and exchange equilibria between apatite and silicate melts, with a particular focus on C and OH. We added halogens (F and Cl) in a subset of runs, in order to evaluate the extent to which this affects the partitioning of C and/or OH. The terminal run pressures (1.0 and 0.5 GPa) and temperatures (1250 °C) employed represent reasonable storage conditions for mid- to lower-crustal mafic magmas. Our chosen run conditions have the added advantages that (a) apatite + melt are commonly the only phases present, and (b) the glass fraction of run products is typically greater than 50% (e.g. Prowatke and Klemme 2006). These conditions simplify interpretation of the partitioning data and ensure that suitably sized areas of glass are available for ion microprobe analysis. Furthermore, it is helpful to avoid crystallisation of other volatile-bearing phases (e.g. amphibole), which could complicate analysis of the partitioning behaviour of volatiles between apatite and melt.

Experimental starting materials

We used two sets of synthetic starting materials ('BA' and 'BM'; Table 1), allowing us to investigate the possible compositional effects on volatile partitioning. Both starting

materials are based on compositions used in previous experimental studies and were chosen in order to take advantage of existing phase equilibrium constraints. Composition 'BA' is a haplobasaltic andesite equivalent to composition SH3 of Prowatke and Klemme (2006). This composition produced large apatite crystals in trace element partitioning experiments at similar temperatures and pressures (Prowatke and Klemme, 2006) and enabled us to consider volatile partitioning in a simplified, Fe-free system in the first instance. Composition 'BM' is a trachyte equivalent to the natural 'ZAC' obsidian composition from Campi Flegrei, Naples, Italy (Fabbrizio and Carroll, 2008). The nominal compositions of both starting materials are given in Table 1.

Starting materials were prepared as mechanical mixtures of reagent grade oxides (Al_2O_3, SiO_2, MgO, MnO, FeO, Fe_2O_3, TiO_2) and carbonates (Na_2CO_3, K_2CO_3, $CaCO_3$) subsequently doped with varying amounts of phosphate (added as $Ca_3(PO_4)_2$) and volatiles (added as described below). Prior to mixing, all components were dried overnight at 100 °C; the oxide powders SiO_2, Al_2O_3, MgO and TiO_2 were additionally fired at 1000 °C to drive off residual moisture. Dried components were then mixed in the desired proportions, ground under ethanol to produce homogenous powders, and slowly decarbonated in a box furnace (600 °C to 1000 °C over 6 hours). For starting material 'BA,' four such powders were produced: a P-bearing split doped with ~25% $Ca_3(PO_4)_2$; a P-free split equivalent to that reported in Table 1, but with added Ca; and carbonated equivalents of both the P-free and P-bearing splits. Calcium was added to the P-free splits such that all splits had equal bulk CaO contents. In the case of C-bearing splits, the carbonate component was added following the decarbonation step. In this way, the bulk proportions of P and C in each run were varied by varying the proportions of the different

splits added to each capsule. Fluorine and Cl were added directly to each capsule as Ca-, K-, or Na-fluorides and chlorides. Because the quantity of F and Cl added was small (typically < 1 wt%), these additions did not significantly affect the proportions of the other components. Hydrogen, where present, was added as liquid water as described below.

Starting material 'BM' was prepared as above, but with an additional glassing step following decarbonation: splits were heated to 1400 °C for 30 minutes in a gas mixing furnace, then ground dry to homogenise. The gas mixture was held near Ni-NiO buffer conditions at the furnace temperature. This heating and grinding process was repeated 1–3 times for each split. Fluorides and chlorides were added to prior to glassing, with carbonate added afterward as above, and splits were mixed to yield the desired bulk volatile proportions (excepting water) before being added to each capsule. These additional steps were employed to ensure the thorough homogenisation of starting materials as needed to aid apatite growth and equilibration in a companion study at lower experimental temperatures and pressures. As we observe no systematic textural differences between the apatites produced by the BA and BM starting materials, we assume that the starting powders were sufficiently homogenised during equilibration at high temperatures so as to negate any potential differences owing to the different preparations of the two starting materials.

Piston cylinder experiments

Starting powders were loaded into 3 mm diameter Pt capsules. In water-bearing experiments, distilled, deionised water was first added to the base of each capsule using a

140 micro-syringe. Capsules were welded shut, then pressed into cylinders approximately
141 4mm in length, and placed into 4 mm diameter outer Pt capsules containing identical
142 proportions of starting powders ± H_2O. The outer capsule was then welded shut and
143 pressed into a cylindrical shape approximately 7 – 8mm in length. Pressing of inner and
144 outer capsules helped to ensure an even distribution of surrounding materials in the
145 nested assembly. The double-capsule technique employed is essential when using Pt
146 capsules, in order to reduce gradients in the chemical potentials of H and C adjacent to
147 the sample, and thus limit the rate of H_2 and C exchange between the sample and the
148 apparatus (Hall et al. 2004, Brooker 1998). In lieu of a solid buffer, this method also
149 helps to maintain a fixed fO_2 (or fH_2) in the inner capsule and helps to minimise volatile
150 loss or gain during runs. After each welding step (inner and outer capsule), capsules were
151 weighed to check for water loss, then heated and reweighed to ensure the integrity of the
152 weld seal.

153 All experiments were run in end-loaded piston cylinder apparatus (Boyd and
154 England 1960) at the University of Bristol. A conventional ½ inch diameter bomb and
155 piston was used for runs at 1 GPa. A ¾ inch diameter bomb was used for two runs at
156 lower pressure (0.5 GPa). The complete sample assembly consisted of the 4 mm diameter
157 outer Pt capsule surrounded by crushable MgO (½ inch diameter setup; for the geometry
158 of this setup, see McDade et al., 2002, their figure 1d) or Al_2O_3 (¾ inch diameter setup,
159 for the geometry of this setup, see McDade et al., 2002, their figure 1e) spacers
160 positioned to centre the capsule in the hot spot of the graphite furnace. The furnace +
161 capsule assembly was fitted within a pyrex sheath and an outer NaCl (½ inch) or talc (¾
162 inch) sleeve. Loaded assemblies were then heated and pressurised according to a 'hot

163 piston in' routine. After applying an initial pressure load, the assembly was allowed to
164 settle for at least 20 minutes. Temperature and pressure were then increased
165 simultaneously, with the final pressure applied upon reaching the run temperature. This
166 routine is in keeping with that used to determine the talc- and salt-pyrex friction
167 correction for set pressures (~3%, McDade et al. 2002). Pressure was maintained by
168 means of an automated pressure regulator to within ±1 psi of the target run pressure,
169 yielding pressure variations of <<1% relative. Run temperature was monitored using
170 $W_{97}Re_3$–$W_{75}Re_{25}$ (D-type) thermocouples, inserted along the assembly axis adjacent to
171 the top of the charge. Temperature was maintained by automated adjustment of the
172 operating power via a Eurotherm, with typical deviations from target of <1 °C. No
173 attempt was made to correct temperatures for a pressure-dependence of e.m.f., although
174 this effect is generally considered negligible for the type of thermocouple used here
175 (Brooker and Kjarsgaard 2011).

176 To encourage growth of experimental apatites, runs were first heated to super-
177 liquidus temperatures (1450–1500 °C), then cooled at a constant rate to a terminal
178 temperature of 1250 °C, following Prowatke and Klemme (2006). Super-liquidus heating
179 reduces the availability of nuclei and/or secondary nucleation sites for crystallising
180 phases, fostering the growth of fewer, larger crystals. A slow cooling ramp results in
181 lower degrees of undercooling and thus further favours crystal growth over nucleation
182 (e.g. Swanson 1977). Typical cooling rates were 20 °C/hr or 50 °C/hr, depending on the
183 bulk water content. Even lower cooling rates (≤ 10 °C/hr) were applied to some runs with
184 lower bulk phosphate contents or nominally zero bulk OH contents (Table 2). Samples
185 were then allowed to equilibrate at the final run temperature, during which time a small

186 temperature cycle was applied (±10 °C at 1 °C per minute) to enhance crystal growth
187 (e.g. Mills and Glazner 2013). Total run times ranged from 20–24 hours and were chosen
188 to provide sufficient time for crystal-melt equilibration, as evidenced by experiments at
189 similar conditions (Prowatke and Klemme 2006), whilst minimising the time available
190 for diffusive exchange at high temperatures. At the end of each run, charges were
191 quenched isobarically by cutting the operating power while manually maintaining the
192 terminal run pressure.

193 Following quench, capsules were removed from the assembly and sectioned using
194 a micro-saw. In order to preserve the double capsule assembly, it was not possible to
195 pierce inner capsules to test for the presence of a free fluid phase, and instead we take the
196 absence of vesicles or gas pockets in most experiments as evidence of volatile
197 undersaturation (three 'BM' samples containing minor vesicles are indicated in Table 2).
198 Sectioned capsules were ground using abrasive SiC papers (220 to 1200 grit) and
199 progressively polished using diamond suspensions (6, 3, and 1 μm). Polished capsules
200 were then mounted either in In metal or a thin layer of EpoFix resin, with the aim of
201 minimising H backgrounds during subsequent ion microprobe analysis.
202
203 ## ANALYTICAL METHODS
204 ### Electron probe microanalysis
205 Apatite and glass major element compositions were determined by electron probe
206 microanalysis using a Cameca SX100 5-spectrometer instrument at the University of
207 Bristol. Glasses were analysed using a 15 kV, 2 nA electron beam defocused to a 15 μm
208 spot, with Na analysed first to minimise alkali migration (Morgan and London 1996;

209 Humphreys et al. 2006). Apatites were analysed using a 15 kV, 10 nA beam defocused to
210 10 μm to minimise migration of halogens yet still enable accurate determination of minor
211 elements (e.g. Goldoff et al. 2012; Stock et al. 2015; see supplementary methods for
212 details of analytical protocol). Calibration standards were albite for Na and Si; St. Johns
213 olivine for Mg; sanidine for Al and K; Durango apatite for P; wollastonite or Durango
214 apatite for Ca; ilmenite for Ti and Fe; Mn metal for Mn; MgF_2 for F; and NaCl for Cl.
215 Count times were 30 s on peak for all elements except Fe and Mn (60 s on peak) and Cl
216 and F (120 s on peak). Resulting detection limits for volatile elements in apatite were
217 typically ~120 ppm for Cl and ~500 ppm for F, whereas in glass the detection limits were
218 typically ~300 ppm for Cl and ~900 ppm for F (for full analytical conditions see
219 supplementary materials). Raw data were processed using a PAP matrix correction
220 scheme. Accuracy and precision of the analytical setup were monitored by repeated
221 analysis of well-characterised secondary standards (KN18, BCR2, and synthetic F-
222 bearing haplobasalt for glasses; oriented Durango and Wilberforce apatite crystals for
223 apatite).
224
225 **Secondary ion mass spectrometry**
226 Volatile compositions of apatite and coexisting glass were determined by secondary ion
227 mass spectrometry using a Cameca ims-4f instrument at the NERC ion microprobe
228 facility at the University of Edinburgh. The instrument is run utilizing Charles Evans and
229 Associates PXT interface and software.
230 For apatite, a 5 nA $^{16}O^-$ primary beam with a net impact energy of 14.5 keV was
231 accelerated onto the sample. An energy window of 75 ± 20 V was applied. The spot size

232 was ~15 – 20 μm. A circular field aperture with an effective radius of 8 μm was used to
233 lower H and C backgrounds coming from the edge of the sputtering pit. Backgrounds
234 were monitored using either end-member (H-free) apatites from Schettler et al. (2011) or
235 a piece of quartz embedded within each sample mount.

236 In addition, a 4-minute pre-sputter period at a raster size of 20 μm was employed
237 to minimise contamination from the sample surface. The secondary ions $^{1}H^{+}$, $^{12}C^{+}$,
238 $^{25}Mg^{2+}$, $^{19}F^{+}$, $^{23}Na^{+}$, $^{26}Mg^{+}$, $^{30}Si^{+}$, $^{31}P^{+}$, $^{35}Cl^{+}$, $^{39}K^{+}$, and $^{44}Ca^{+}$ were collected for 5s, 10s,
239 6s, 10s, 2s, 5s, 2s, 2s, 10s, 3s, and 2s, respectively, for each 6 cycles of the magnet. Only
240 H_2O, CO_2, F, P_2O_5, and Cl were quantified. Other elements were used to monitor for
241 contamination with the silicate glass. The OH and CO_3^{2-} contents of apatite were
242 determined using daily working curves of $^{1}H/^{44}Ca$ vs. OH and $^{12}C/^{44}Ca$ vs. C acquired for
243 a suite of natural apatite standards (supplementary information), after correction for
244 isobaric interference by $^{24}Mg^{2+}$ on ^{12}C (correction generally < 5%, except in the most C-
245 poor samples up to 15%). The same approach was taken for both F and Cl, with 95%
246 prediction intervals calculated for every calibration line (supplementary materials). For a
247 small subset of apatite crystals (< 15 μm in smallest dimension), the beam current was
248 reduced to 2 nA resulting in a spot size of <10 μm. This process reduced the number of
249 ions counted, but had no appreciable effect on the calibration curve slopes. Halogens
250 were also quantified for halogen-free experiments as a check for contamination. No effect
251 of apatite orientation (parallel vs. perpendicular to the c-axis) on working curves for H_2O,
252 CO_2, F, and Cl was detected, consistent with the findings of Stock et al. (2015).

253 For the glass, a similar analytical setup and procedures were used as for apatite,
254 apart from using a 50 ± 20 V energy window for C analysis (a 75 ± 20 V energy window

was used for analysis of H and other elements). To ensure accurate determination of C contents in the Mg-rich glass, an initial set of analyses was collected at sufficient mass resolution to separate the $^{12}C^{+}$ and $^{24}Mg^{2+}$ peaks, with secondary ions collected at $^{24}Mg^{2+}$, $^{12}C^{+}$, $^{26}Mg^{+}$, and $^{30}Si^{+}$ for 5s, 10s, 3s, and 2s, respectively, for each of 10 cycles of the magnet. In a second set of analyses on the same spot (with a 2-minute pre-sputter period and 20 μm raster), the secondary ions $^{1}H^{+}$, $^{11}B^{+}$, $^{19}F^{+}$, $^{26}Mg^{+}$, $^{30}Si^{+}$, and $^{35}Cl^{+}$ were collected for 3s, 3s, 6s, 2s, 2s, and 6s, respectively (over 10 magnet cycles). As with apatite, H_2O and CO_2 contents of the glasses were determined using daily working curves of $^{1}H/^{30}Si$ vs. H_2O and $^{12}C/^{30}Si*SiO_2$ vs. CO_2, respectively, generated from standard glasses including basalts and phonolites. The calibration glasses included samples from Shishkina et al. (2010), Hauri et al. (2002), Mangan and Sisson (2000), and Brooker et al. (1999), (see supplementary information for details). A field aperture was used to reduce backgrounds for H and C, which were monitored using either a volatile-free glass from Shishkina et al. (2010) or a piece of quartz embedded within each sample mount. Halogens were calculated using Lipari glass (Hunt and Hill 1993) as the primary calibration standard for Cl, and NIST SRM610 glass as the primary calibration standard for F. Halogens were also quantified for halogen-free experiments as a check for possible contamination. Values were checked against internal secondary glass standards and synthetic halogen-rich glasses synthesised using the starting material SH3. SIMS glass halogen concentrations were also checked and compared against EPMA.

Secondary electron microscopy (SEM)

Back-scattered SEM images of polished, mounted samples were collected using a Hitachi S-3500N scanning electron microscope at the University of Bristol, with a 15 – 20 kV accelerating voltage and 15 mm working distance. All samples were imaged prior to SIMS analysis in order to identify the phases present, produce image maps for sample navigation, and locate areas of apatite and glass suitable for ion microprobe work (sufficiently large and free from cracks and inclusions). To avoid contaminating the sample surface with C in advance of SIMS analysis, samples were not C coated prior to imaging in low vacuum mode. Run products were imaged again following ion microprobe work to confirm the location of sputter craters.

Apatite stoichiometry

We followed the calculation scheme of Ketcham (2015) for stoichiometric calculations, with formula proportions calculated on a 25-oxygen basis. We placed Mg, Mn, Fe, and Na on the Ca site, and Si onto the phosphate site. Any deficiency in P on the phosphate site was filled with carbonate where possible; any remaining carbonate was placed onto the channel volatile site together with F, Cl, and hydroxyl (Table 3). Stoichiometric totals are generally good, with the Ca-site contents 9.967 ± 0.070, P-site contents 6.037 ± 0.030, and average X-site totals for the halogen-bearing experiments of 1.913 ± 0.087 (Table 3), although halogen-free experiments have lower totals (see below). There is also a correlation between the measured OH and OH calculated by difference (see later discussion).

RESULTS

Experimental run products

Experimental run products for both starting materials typically comprise microlite-free glass + apatite, with a minority of samples also containing clinopyroxene ± fluid (see Table 2; Fig. 1). The experiments were designed to be volatile-undersaturated, because of the difficulty of constraining the composition of any fluid(s). The two experiments run at 0.5 GPa contain sparse vesicles, which may indicate that these samples had just reached volatile saturation. Apatites are large and euhedral (typically up to 100 μm perpendicular to c-axis and up to 1 mm parallel to the c-axis) and commonly contain melt inclusions that are visible in sections cut perpendicular to the c-axis (Fig. 1). Experiments run at lower pressures or higher cooling rates formed apatites with more skeletal or hopper textures.

Glasses

Experimental glasses from the "BA" experiments are Al-rich haplobasalts with ~5 wt% total alkalis, 9 – 10 wt% MgO, 14 – 16 wt% Al_2O_3, and 18 – 30 wt% CaO on an anhydrous basis (Table 4). Silica contents are 44.4 – 49.6 wt% SiO_2, normalised to 100% on an H- and C-free basis. The glasses have high volatile concentrations, as expected given the experimental run pressure of 1 GPa and nominal bulk volatile compositions (Table 2). Some CO_2 was found even in the nominally C-free runs, which we attribute to infiltration of C through the Pt capsule walls during the course of the experiment (Brooker et al. 1998) or possibly incomplete decarbonation of the starting material and/or atmospheric contamination. H_2O contents are in the range 0.7 – 7.1 wt%, and CO_2 concentrations range from 300 ppm to 1.3 wt% (Table 4). Halogen concentrations in the glass are 0.8 – 1.6 wt% F and ~0.8 wt% Cl (Table 4).

323 The "BM" experiments formed phonolitic glasses with 57.2 – 61.8 wt% SiO_2 and
324 12.6 – 16.3 wt% total alkalis (Table 4). For the halogen-bearing "BM" experiments,
325 halogens were added in the form of NaCl and NaF, so the melts for these experiments
326 have correspondingly higher Na_2O contents (Table 4). H_2O concentrations are in the
327 range 1.3 – 7.1 wt% and CO_2 concentrations are 1600 – 7100 ppm, consistent with
328 volatile concentrations in the BA experimental glasses. Fluorine contents are also similar
329 to those in the BA glasses (0.85 – 1.0 wt% F) but Cl concentrations are higher (1.25 wt%
330 Cl) for the same nominal bulk Cl added. Glasses are homogeneous throughout each
331 sample, with typical relative standard deviations of approximately 1.2% for CO_2, H_2O, F,
332 and Cl. This is smaller than the analytical uncertainty, and we therefore used the
333 analytical uncertainty to estimate and propagate errors in the partitioning data.
334 *Apatites*
335 Experimental apatites from the halogen-free BA experiments are hydroxy-apatites with
336 0.7 – 1.7 wt% H_2O and a wide range of C contents up to 1.80 wt% (C expressed as CO_2)
337 (Table 3). Apatites from the halogen-bearing experiments are hydroxyl-bearing fluor-
338 apatite, with ≥ 2 wt% F and compositions systematically shifted to lower OH and C
339 contents (≤ 0.8 wt% H_2O and ≤ 0.22 wt% CO_2, Table 3). Apatites from these halogen-
340 bearing experiments have volatile contents of F > Cl >> OH > C, even when these
341 components were added in the same concentrations to the starting mixture (e.g. BA12,
342 which had 1 wt% each of F, Cl, and OH in the starting material, Tables 2 and 3). In the
343 halogen-free experiments, the apatite H_2O and CO_2 contents increase with increasing
344 dissolved H_2O and CO_2 in the coexisting glass, respectively, and the CO_2 content
345 increases with increasing $CO_2/(H_2O+CO_2)$ in the glass (Fig. 2). The same pattern is

346 observed in the halogen-bearing experiments, but with lower overall OH and C contents
347 as described above. Similarly, experimental apatites from the BM experiments show high
348 H_2O and CO_2 contents in the halogen-free runs, (0.7–1.2 wt% H_2O and up to 1.2 wt%
349 CO_2) and significantly lower concentrations in the halogen-bearing experiments, which
350 routinely produced fluor-apatite with >2.5 wt% F (Table 3). Carbon contents increase
351 with increasing concentration of the minor elements (Mg, Na, and Si; Fig. 3).

352 The stoichiometry calculations suggest that, for the halogen-free experiments,
353 there is no space on the phosphate site for carbonate, such that all the carbonate and
354 hydroxyl are accommodated on the channel site (Table 3). In contrast, for some of the
355 halogen-bearing experiments, there is sufficient space on the phosphate site to assign
356 some of the carbonate, with the channel site occupied by the remaining carbonate,
357 halogens, and hydroxyl.

358 Minor element concentrations in the apatites are clearly related to the host melt
359 composition. Apatites from the BM experiments typically contain higher alkalis and
360 lower Mg compared with those from the BA experiments (Table 3).

361

362 **Partitioning data**

363 We used the experimental apatite and glass compositions to calculate the apparent Nernst
364 partition coefficients, $D_i = \frac{C_i^{ap}}{C_i^m}$, where C is the concentration of element i in wt%. This
365 representation allows the distribution of volatile species between apatite and melt to be
366 directly compared with other literature data (in the case of H, F, and Cl), and to give the
367 first experimentally-determined partitioning data for C between apatite and silicate melts.
368 Note that to maintain consistency with previous studies (e.g. McCubbin et al. 2015), we

have calculated the partition coefficients between volatile abundances in apatite and melt as the same species, i.e. OH in apatite is calculated as the equivalent H_2O content, whereas CO_3^{2-} in apatite is calculated as the equivalent CO_2 content, on a concentration (wt%) basis. Our calculated Ds show, as expected, that F is highly compatible in apatite, with D_F between 1.3 and 3.6 (average = 2.2). Chlorine is moderately compatible (D_{Cl} = 0.7 to 2.2), and OH is generally incompatible (D_{OH} = 0.06 to 0.97; average = 0.27) (Table 5), although its compatibility varies with a bulk mixed volatile content. $D_{CO_3^{2-}}$ is variable, with values ranging from 0.05 to 2.1. Notably, CO_3^{2-} was actually compatible in apatite in several of the halogen-free experiments. Both $D_{CO_3^{2-}}$ and D_{OH} are significantly higher in the halogen-free runs.

Although Nernst partition coefficients (D) have been widely reported in studies of volatile partitioning in apatite, the more appropriate measure of partitioning for major chemical components competing for the same crystallographic site, such as F, Cl, and OH in apatite, is the exchange coefficient, K_D (e.g. Roeder and Emslie 1970), defined as the ratio of partition coefficients of two species, e.g.:

$$K_D^{OH\text{-}Cl} = (OH_{ap}/OH_m)/(Cl_{ap}/Cl_m) = (OH_{ap}/Cl_{ap})/(OH_m/Cl_m) \quad (1)$$

According to the strict definition of these distribution coefficients, the volatile components should be calculated using activity (or mole fraction if assuming ideal behaviour). However, it is not obvious that this approach brings greater clarity to the results of these experiments. In particular, the high pressures and range of melt compositions used means that there is some considerable uncertainty concerning the validity of models describing the distribution of dissolved water and C species in the melt (e.g. Brooker et al. 1999; Sowerby and Keppler 1999; Morizet et al. 2002; Hui et al.

2008), even if the apatite behaviour is ideal at high pressure and temperature (see Li and Hermann 2017 for a discussion). For completeness, we give apatite-melt $K_D^{OH\text{-}Cl}$, $K_D^{OH\text{-}F}$, and $K_D^{Cl\text{-}F}$ in mole fraction form (supplementary information) using the same water speciation model as Li and Hermann (2017) for consistency with their approach, though this may not be the most appropriate for the range of melt compositions included. These K_D's are calculated by normalising the volatile site contents such that $X_{OH} + X_F + X_{Cl} = 1$, excluding carbonate (supplementary information). For OH-carbonate exchange, however, we present only K_D's calculated on a concentration basis in order to avoid introducing errors as a result of the poorly understood variation in C speciation in silicate melts (e.g., Morizet et al. 2002).

From our experiments, the resulting distribution coefficients (calculated following McCubbin et al. 2015 as the ratio of partition coefficients) are $K_D^{H2O\text{-}F} = 0.023–0.08$, $K_D^{H2O\text{-}Cl} = 0.08–0.11$, and $K_D^{Cl\text{-}F} = 0.27–0.98$ (Table 5). Apatite-melt distribution coefficients for H_2O-CO_2 exchange are defined more rigorously in Figure 4 through $\log K_D^{H2O\text{-}CO2} = \log D_{H2O} - \log D_{CO2}$, where $\log K_D$ is the intercept. This gives $K_D^{H2O\text{-}CO2} = 0.355 \pm 0.05$ for the 'BM' experiments and 0.629 ± 0.08 for the 'BA' experiments (uncertainties represent a 95% prediction interval). This suggests a dependence on the melt major element composition, with systematically higher K_D's (as calculated for individual experiments) in the BM system (Fig. 4). The gradient in Figure 4 is approximately 0.65 for both the BM and BA experiments, whereas for an ideal system it should be equal to 1.0. This suggests that C-H partitioning may be non-ideal for high-temperature igneous apatites, which would be consistent with the development of significant vacancy concentrations in the more carbonate-rich apatites (see below).

DISCUSSION

CO_3^{2-} in apatite

Our primary focus was to define the carbonate partitioning behaviour between hydroxyl-bearing apatite and hydrous silicate melt. The apatites themselves contain quite high carbonate concentrations, typically several hundred to a few thousand ppm, even in the halogen-bearing experiments. This is in contrast with natural silicate melts, which commonly record magmatic volatile concentrations only after significant degassing of CO_2, either into a fluid phase or during post-entrapment modification and formation of a shrinkage bubble, resulting in lower CO_2 contents of typically a few hundred ppm (Wallace 2005; Blundy et al. 2010; Hudgins et al. 2015; Tuohy et al. 2016; Maclennan 2017). The K_D's for OH-carbonate exchange ($K_D^{H2O\text{-}CO2}$) appear to be dependent on the melt major element composition, with higher values in the BM experiments than in the BA experiments (see Fig. 4; Table 5). In contrast, the apparent carbonate-halogen exchange coefficients are very low, with $K_D{}^{CO_2-Cl} < 0.17$ and $K_D{}^{CO_2-F} < 0.11$ (Table 5). To the best of our knowledge, these are the first experimental constraints on carbonate partitioning in igneous apatite, so we are unable to compare our data with those of other studies. The advantage of SIMS analysis is that the total C concentration is technically easy to measure *in situ* on unoriented grains, although it cannot provide structural information related to site occupancy, which requires techniques such as FTIR, XRD or NMR (e.g., Fleet, 2017).

Incorporation of CO_3^{2-} in experimental igneous apatites

Previous work has identified that carbonate can be accommodated in apatite *via* two key substitution mechanisms. In 'Type A' apatite, carbonate is incorporated by exchange of a hydroxyl ion for a carbonate anion within the c-axis channel site, plus an OH^- vacancy for charge compensation (e.g. LeGeros et al. 1969; Bonel 1972; Young et al. 1981):

$$CO_3^{2-} + \square = 2(OH^-,F^-,Cl^-) \quad (2)$$

In 'Type B' carbonate, the CO_3^{2-} ion is substituted for PO_4^{3-}, as demonstrated by substantially lower P concentrations in carbonated apatite. This substitution may be charge-balanced according to the mechanism

$$PO_4^{3-} = CO_3^{2-} + F^- \quad (3)$$

(e.g. Binder and Troll 1989), although NMR work shows that the charge-balancing F^- is not directly interacting with carbonate as a tetrahedal complex (Mason et al. 2009). Various other substitution mechanisms are also possible (e.g. Pan and Fleet 2002):

$$Ca^{2+} + 2PO_4^{3-} = \square^{Ca} + 2CO_3^{2-} \quad (4)$$

$$Ca^{2+} + PO_4^{3-} = Na^+ + CO_3^{2-} \quad (5)$$

$$Ca^{2+} + F^- = REE^{3+} + CO_3^{2-} \quad (6)$$

Apatite data from our halogen-free experiments indicate that the Type A substitution mechanism is the dominant one for the carbonate anion. Both the carbonate and OH contents of apatite vary systematically with increasing $CO_2/(H_2O+CO_2)$ in the host melt (see Fig. 2). This indicates that the apatite carbonate concentrations are directly linked to the volatile composition of the melt. Since OH is well known to occupy the channel site, this indicates that carbonate is also incorporated into the channel site. The stoichiometry calculations also indicate that there is insufficient space on the phosphate site to

accommodate any significant Type B carbonate, and therefore the carbonate should sit on the X-site (Type A; see Table 3). This has been confirmed using FTIR (see supplementary Figure 1) where the positions of the carbonate ν3 vibrational peaks are consistent with dominantly A site occupation (e.g. Fleet et al. 2004; Fleet 2017). However, while OH calculated by charge balance in the channel site is equivalent to measured OH in the most OH-rich samples, for samples with higher carbonate contents the measured OH is significantly lower than OH calculated by charge balance (Fig. 5). This suggests that the incorporation of carbonate into igneous apatite at high temperatures may involve the creation of vacancies, significantly greater than the number of OH^- vacancies predicted to charge balance CO_3^{2-} via equation (2). The presence of structural H_2O in the channel site (e.g. Mason et al. 2009; Yoder et al. 2012) seems unlikely given the high run temperatures of the experiments.

In fact, the under-occupancy of the X-site suggests the formation of a significant "oxyapatite" component, with O^{2-} (and a vacancy) substituting for $2OH^-$ within the channel site (Trombe and Montel 1978; Young et al. 1981; Schettler et al., 2011). First principles calculations support the idea that significant defects on the channel site can be formed at high temperatures (> 1000K), including the formation of oxyapatite coupled to OH^- vacancies, resulting in significant non-stoichiometry at high temperatures (Matsunaga and Kuwabara 2007; Kubota et al. 2014). This deviation from stoichiometric mineral formulae is consistent with our interpretation that C-H exchange is non-ideal.

Our observations are also consistent with experiments that resulted in the formation of Type A carbonate apatite by the reaction of hydroxyapatite with dry CO_2 (Bonel 1972); and with first principles calculations that indicate a greater stability of the

Type A substitution at high temperatures (Kubota et al. 2014). The lack of negative correlation between CO_3^{2-} and Ca or P also argues against a significant B-type substitution (de Maeyer et al. 1993). However, the highest total carbonate contents are also associated with high minor element concentrations (e.g. Mg, Na), which suggests a subsidiary Type B substitution similar to (5) or (6). Peroos et al. (2006) showed that although the Type A substitution was energetically favourable, a Type B substitution, charge balanced by Na^+, was also favourable when Type-A carbonate was already present.

In contrast, the stoichiometry of apatites from our halogen-bearing experiments suggests the additional formation of some B-type carbonate apatite. In some of these apatites, the phosphate site has enough space to accommodate some carbonate, and the channel site incorporates the remainder plus halogens and OH (Table 3). In contrast with apatites from the halogen-free experiments, there is good agreement between OH contents calculated by difference and measured OH for the halogen-bearing experiments (Fig. 5). This suggests that these calculated site assignments are reasonable, and consistent with calculations showing that at high temperatures the Type A carbonate substitution should be more stable than Type B (e.g. Kubota et al. 2014). However, we suggest that in the presence of abundant halogens, the formation of F-Cl-OH apatite is the most energetically favourable, and that carbonate can be shifted onto the phosphate site.

OH-Cl-F distribution between apatite and silicate melt

The OH-F-Cl apatite-melt exchange coefficients calculated from our experimental data are consistent with those of other studies, but with some significant differences. There are

only two other experimental Cl-OH-F apatite-melt partitioning studies with direct measurements of all channel site components. The extended abstract by Potts et al. (2015) reported experiments conducted at 1 GPa and 1350 – 1450 °C with a composition similar to the mesostasis of lunar basalts, while McCubbin et al. (2015) performed apatite-melt experiments at 1 – 1.2 GPa and 950 – 1000 °C using an Fe-rich basalt. Our calculated nominal D_F, D_{Cl}, and D_{OH} are within the range reported by these and other previous studies (Fig. 6; Table 7). This includes experiments without direct measurement of OH, for which we calculated nominal D_{OH} 'by difference' (see Table 7; Doherty et al. 2014, rhyodacite at 50 MPa, 850 – 950 °C; Webster et al. 2009, rhyodacite at 200 MPa, ~900 °C; Mathez and Webster 2005, basalt, 1050-1150 °C; Webster et al. 2017, rhyolite at 50 – 200 MPa and 700 – 1000 °C; and Li and Hermann 2015 and 2017, 'pelite' melts at 2.5 – 4.5 GPa and 600-900 °C). This was done assuming a stoichiometric channel site containing no carbonate (see earlier discussion) and calculating $H_2O_{(m)}$ by difference where necessary. These 'by difference' calculations are subject to a significant uncertainty (e.g. Devine et al. 1995; Humphreys et al. 2006), and the direct analysis of all volatile components in both melt and apatite is strongly encouraged for future work. The dataset also includes a mixture of volatile-saturated and volatile-undersaturated experiments (see Table 7), and at least some of the volatile-saturated experiments are rich enough in Cl that fluid immiscibility is likely (e.g., Webster et al. 2017). These results, perhaps not surprisingly, are strongly scattered and cover a wide compositional range (Figs. 6-8). The variation in starting materials and experimental conditions suggests that some of this variability may be due to the effects of changing melt composition or pressure and temperature. This is supported by a systematic decrease in both D_F and, to a

530 lesser extent, D_{Cl}, with increasing temperature and increasing melt CaO content in the
531 compiled literature dataset. Increasing experimental pressure causes only a minimal
532 decrease in $D_{F,Cl}^{ap\text{-}m}$.

533 As with Figure 4, the distribution coefficients for OH-halogen exchange are
534 equivalent to the intercept in Figure 6. Thus, our calculated $K_D^{OH\text{-}F}$ are slightly lower than
535 those of Potts et al. (2015) but higher than those of (McCubbin et al. 2015). Each study
536 was conducted at the same pressure (1 GPa), so we interpret these differences in K_D as
537 predominantly a result of differences in temperature (in the range 950 °C to 1450 °C).
538 This is borne out by the results of a multiple regression analysis of the full literature
539 dataset, including our new experiments (Fig. 8), to an equation of the form

540 $$\log K_D = a + b/T + c(P-1)/T \quad (7)$$

541 following the approach of Piccoli and Candela (1994). This shows a clear log-linear
542 increase in $K_D^{OH\text{-}halogen}$ with increasing temperature, which indicates a preference for the
543 OH end-member at higher temperatures for a given melt composition. Despite the
544 inclusion of both volatile-saturated and volatile-undersaturated experiments from rhyolite
545 to basalt, the relative consistency of the published K_Ds, as a function of temperature, is
546 striking, and confirms that temperature is the dominant overall control on apatite-melt
547 volatile partitioning. The CaO content in the melt was not a significant variable,
548 presumably due to covariation with temperature. The pressure term was of subsidiary
549 significance and we obtained better confidence on the parameter values by excluding the
550 third term in equation (2) (Table 6). For OH-Cl exchange, the results gave a = 1.0729 ±
551 0.2353 and b = -2938.4 ± 282.3 whereas for OH-F exchange, a = 1.2590 ± 0.2942 and b
552 = -3853.6 ± 367.8 (Fig. 8, Table 6).

553 We compared these results with earlier thermodynamic expressions derived by
554 Piccoli and Candela (1994) for the system apatite-fluid. Their $K_D^{ap\text{-}fl}$ were calculated
555 using the thermodynamic data of Zhu and Sverjensky (1991) to give the fugacity ratio for
556 the coexisting aqueous fluid, with aqueous species data derived from Robie et al. (1978)
557 and Stull and Prophet (1971). High-temperature values for $K_D^{OH\text{-}Cl}$ are up to an order of
558 magnitude lower for the apatite-fluid than for the apatite-melt K_D exchange data, but
559 there is better agreement between the two systems at low temperatures (Fig. 8). There is
560 also agreement on the direction of change of K_D with temperature (cf. Li and Hermann
561 2015). In contrast, the values for $K_D^{OH\text{-}F}$ are 2-3 orders of magnitude lower for apatite-
562 fluid (Piccoli and Candela, 1994) than for apatite-melt (see literature data compilation in
563 Fig. 8). The cause of this mismatch for $K_D^{OH\text{-}F}$ is unclear, particularly given that there is
564 relatively good agreement for $K_D^{OH\text{-}Cl}$ at low temperatures (where one or more fluid
565 phases are most likely to be present). Calculating K_Ds using OH and halogen mole
566 fractions instead of H_2O_t results in higher values in Figure 8. The experiments do not
567 contain any other phases that could incorporate significant F. Our calculations (together
568 with those of the other studies in the literature) were done using melt F concentrations
569 instead of activities, and fluoride activity varies with both melt composition (e.g. Scaillet
570 and Macdonald 2004) and temperature (e.g. Webster 1990). Piccoli and Candela (1994)
571 attempted to apply their method to the Bishop Tuff and found similar problems, with
572 good agreement between predicted (from apatite) and measured (from melt inclusions) Cl
573 concentrations, but a much wider discrepancy for F, which they interpreted as a problem
574 with the assumption that F is present only as HF in the fluid. We therefore suggest that

575 improved fluoride activity and speciation models for silicate melts and fluids may help to
576 resolve this problem.
577
578 **Implications**
579 Recent experimental students of apatite–melt partitioning have greatly enhanced the
580 potential of apatite as a tool for interpreting magmatic volatile contents, in both terrestrial
581 and planetary settings (Piccoli and Candela, 1994; Boyce and Hervig, 2008; McCubbin et
582 al. 2015). The results presented here extend this work to the important magmatic volatile
583 C, which records key information regarding deep magma storage and early degassing
584 processes. Our new partitioning experiments on haplobasaltic andesite and trachyte melts
585 provide the first constraints on partitioning mechanisms and exchange coefficients for C
586 in high-temperature igneous apatite. Stoichiometry calculations and preliminary FTIR-
587 ATR analysis indicates that carbonate is accommodated primarily in the c-axis channel in
588 our experiments. OH calculated by difference agrees relatively well with measured OH
589 for the halogen-bearing experiments but is systematically low for the halogen-free
590 experiments. This suggests the presence of a significant oxyapatite component at high
591 temperatures, and emphasises that calculations of OH by difference should be treated
592 with care. Analysis of C in apatite represents a potential new route to better
593 understanding the original CO_2 contents of melts, particularly in arc systems, where melt
594 inclusion CO_2 concentrations likely represent a significant underestimate of CO_2 in the
595 un-degassed melt. The ease of SIMS analysis, as demonstrated here, should facilitate this
596 goal, particularly for small natural crystals and inclusions within phenocrysts. We
597 encourage future work comparing CO_2 in arc melt inclusions with CO_2 inferred from

598 coexisting apatite inclusions, and suggest that this may help to improve our understanding
599 of volatile fluxes at subduction zones.

600 Regression of our new partitioning data, alongside previously published
601 experimental data in the system apatite–silicate melt, shows that while measurements of
602 Cl–OH exchange are in good agreement with existing estimates for the system apatite–
603 fluid (Piccoli and Candela, 1994), there is a large discrepancy for F–OH exchange, which
604 may be due a to relatively poor understanding of the fluoride activity and speciation in
605 silicate melts and fluids. This highlights the need for further experimental work focused
606 on clarifying the mobility and compatibility of halogens between solids, melt, and fluids
607 close to the magmatic-hydrothermal transition. Nonetheless, the current study marks a
608 significant advance in the understanding of volatile partitioning in high-temperature
609 igneous apatites and opens up the potential for quantitative analysis and modelling of
610 magmatic volatile systematics in both terrestrial and extra-terrestrial environments.
611 Apatite can accommodate the full range of volatile elements and, in our view, future
612 work should focus on the quantitative modelling of variations in apatite composition
613 during common igneous processes such as cooling, ascent, and degassing of fluid(s), with
614 the aim of fully developing apatite as a tool for investigating magmatic storage and
615 degassing processes.

616

617 **ACKNOWLEDGEMENTS**

618 This project was funded by the Natural Environment Research Council under grants
619 NE/K003852/1 and NE/K004786/1, as well as multiple visits to the NERC ion
620 microprobe facility at University of Edinburgh. MCSH was supported by a Royal Society

University Research Fellowship. We are grateful to Stuart Kearns for analytical support for the electron microprobe, and to Francis McCubbin and Victoria Smith for useful discussions. We acknowledge Bernie Wood and Andrew Matzen for access to the high-temperature gas-mixing furnace at University of Oxford, and Niccy Potts for access to her unpublished experimental distribution coefficients. We thank Francis McCubbin and Adam Simon for journal reviews that helped to clarify the manuscript, and Daniel Harlov for his editorial contributions. Finally, MCSH is grateful to Tom Sisson and Tim Grove for, in a previous decade, encouraging a study of volatiles in apatite.

REFERENCES CITED

Aster, E.M., Wallace, P.J., Moore, L.R., Watkins, J., Gazel, E., and Bodnar, R.J. (2016) Reconstructing CO_2 concentrations in basaltic melt inclusions using Raman analysis of vapor bubbles. Journal of Volcanology and Geothermal Research, 323, 148–162.

Binder, G., and Troll, G. (1989) Coupled anion substitution in natural carbon-bearing apatites. Contributions to Mineralogy and Petrology, 101, 394–401.

Blundy, J., Cashman, K.V., Rust, A., and Witham, F. (2010) A case for CO_2-rich arc magmas. Earth and Planetary Science Letters, 290, 289–301.

Bonel, G. (1972) Contribution a l'étude de la carbonatation des apatites. 1. Synthèse et étude des propriétés physico-chimiques des apatites carbonatées du Type A. Annales de Chimie, 7, 65–88.

Boyce, J.W., and Hervig, R.L. (2008) Magmatic degassing histories from apatite volatile stratigraphy. Geology, 36, 63-66

Boyd, F.R., and England, J.L. (1960) Apparatus for phase-equilibrium measurements at pressures up to 50 kilobars and temperatures up to 1750 °C. Journal of Geophysical Research, 65, 741–748.

Brooker, R., Holloway, J.R., and Hervig, R. (1998) Reduction in piston-cylinder experiments: The detection of carbon infiltration into platinum capsules. American Mineralogist, 83, 985–994.

Brooker, R.A., Kohn, S.C., Holloway, J.R., McMillan, P.F., and Carroll, M.R. (1999). Solubility, speciation and dissolution mechanisms for CO_2 in melts on the $NaAlO_2$-SiO_2 join. Geochimica et Cosmochimica Acta, 63, 3549-3565

Brooker, R.A., and Kjarsgaard, B.A. (2011) Silicate-carbonate liquid immiscibility and phase relations in the system SiO_2-Na_2O-Al_2O_3-CaO-CO_2 at 0.1-2.5 GPa with applications to carbonatite genesis. Journal of Petrology, 52, 1281–1305.

Brooker, R.A., Kohn, S.C., Holloway, J.R., McMillan, P.F., and Carroll, M.R. (1999) Solubility, speciation and dissolution mechanisms for CO_2 in melts on the NaAlO2-SiO2 join. Geochimica et Cosmochimica Acta, 63, 3549–3565.

Bureau, H., Metrich, N., Semet, M.P., and Staudacher, T. (1999) Fluid-magma decoupling in a hot-spot volcano. Geophysical Research Letters, 26, 3501–3504.

Collins, S.J., Pyle, D.M., and Maclennan, J. (2009) Melt inclusions track pre-eruption storage and dehydration of magmas at Etna. Geology, 37, 571–574.

De Maeyer, E.A.P., Verbeeck, R.M.H., and Naessens, D.E. (1993) Stoichiometry of Na^+ and CO_3^{2-} containing apatites obtained by hydrolysis of monetite. Inorganic Chemistry, 32, 5709–5714.

Devine, J.D., Gardner, J.E., Brack, H.P., Layne, G.D., and Rutherford, M.J. (1995) Comparison of microanalytical methods for estimating H_2O contents of silicic volcanic glasses. American Mineralogist, 80, 319–328.

Doherty, A.L., Webster, J.D., Goldoff, B.A., and Piccoli, P.M. (2014) Partitioning behavior of chlorine and fluorine in felsic melt–fluid(s)–apatite systems at 50MPa and 850–950°C. Chemical Geology, 384, 94–111.

Fabbrizio, A., and Carroll, M.R. (2008) Experimental constraints on the differentiation process and pre-eruptive conditions in the magmatic system of Phlegraean Fields (Naples, Italy). Journal of Volcanology and Geothermal Research, 171, 88-102

Fleet, M.E. (2017) Infrared spectra of carbonate apatites: Evidence for a connection between bone mineral and body fluids. American Mineralogist, 102, 149–157.

Fleet, M.E., Liu, X., and King, P.L. (2004) Accommodation of the carbonate ion in apatite: An FTIR and X-ray structure study of crystals synthesized at 2-4 GPa. American Mineralogist, 89, 1422–1432.

Gaetani, G.A., O'Leary, J.A., Shimizu, N., Bucholz, C.E., and Newville, M. (2012) Rapid reequilibration of H_2O and oxygen fugacity in olivine-hosted melt inclusions. Geology, 40, 915–918.

Goldoff, B., Webster, J.D., and Harlov, D.E. (2012) Characterization of fluor-chlorapatites by electron probe microanalysis with a focus on time-dependent intensity variation of halogens. American Mineralogist, 97, 1103–1115.

Hall, L.J., Brodie, J., Wood, B.J., and Carroll, M.R. (2004) Iron and water losses from hydrous basalts contained in $Au_{80}Pd_{20}$ capsules at high pressure and temperature. Mineralogical Magazine, 68, 75–81.

Hartley, M.E., Maclennan, J., Edmonds, M., and Thordarson, T. (2014) Reconstructing the deep CO_2 degassing behaviour of large basaltic fissure eruptions. Earth and Planetary Science Letters, 393, 120–131.

Hauri, E., Wang, J., Dixon, J.E., King, P.L., Mandeville, C., and Newman, S. (2002) SIMS analysis of volatile in silicate glasses 1. Calibration, matrix effects and comparisons with FTIR. Chemical Geology, 183, 99-114

Hudgins, T.R., Mukasa, S.B., Simon, A.C., Moore, G., and Barifaijo, E. (2015) Melt inclusion evidence for CO_2-rich melts beneath the western branch of the East African Rift: implications for long-term storage of volatiles in the deep lithospheric mantle. Contributions to Mineralogy and Petrology, 169, 46.

701 Hui, H., Zhang, Y., Xu, Z., and Behrens, H. (2008) Pressure dependence of the speciation
702 of dissolved water in rhyolitic melts. Geochimica et Cosmochimica Acta, 72,
703 3229–3240.

704 Humphreys, M., Kearns, S., and Blundy, J. (2006) SIMS investigation of electron-beam
705 damage to hydrous, rhyolitic glasses: Implications for melt inclusion analysis.
706 American Mineralogist, 91, 667–679.

707 Hunt, J.B., and Hill, P.G. (1993) Tephra geochemistry: a discussion of some persistent
708 analytical problems. The Holocene, 3, 271–278.

709 Ketcham, R.A. (2015) Technical Note: Calculation of stoichiometry from EMP data for
710 apatite and other phases with mixing on monovalent anion sites. American
711 Mineralogist, 100, 1620-1623

712 Konecke, B.A., Fiege, A., Simon, A.C., Parat, F., and Stechern, A. (2017) Co-variability
713 of S^{6+}, S^{4+}, and S^{2-} in apatite as a function of oxidation state: Implications for a
714 new oxybarometer. American Mineralogist, 102, 548–557.

715 Kubota, T., Nakamura, A., Toyoura, K., and Matsunaga, K. (2014) The effect of
716 chemical potential on the thermodynamic stability of carbonate ions in
717 hydroxyapatite. Acta Biomaterialia, 10, 3716–3722.

718 LeGeros, R.Z., Trautz, O.R., Klein, E., and LeGeros, J.P. (1969) Two types of carbonate
719 substitution in the apatite structure. Specialia.

720 Li, H., and Hermann, J. (2015) Apatite as an indicator of fluid salinity: An experimental
721 study of chlorine and fluorine partitioning in subducted sediments. Geochimica et
722 Cosmochimica Acta, 166, 267–297.

723 ——— (2017) Chlorine and fluorine partitioning between apatite and sediment melt at
724 2.5 GPa, 800 °C: A new experimentally derived thermodynamic model. American
725 Mineralogist, 102, 580–594.

726 Maclennan, J. (2017) Bubble formation and decrepitation control the CO_2 content of
727 olivine-hosted melt inclusions. Geochemistry, Geophysics, Geosystems, 18, 597–
728 616.

729 Mangan, M., and Sisson, T. (2000) Delayed, disequilibrium degassing in rhyolite magma:
730 decompression experiments and implications for explosive volcanism. Earth and
731 Planetary Science Letters, 183, 441-455

732 Marks, M.A.W., Wenzel, T., Whitehouse, M.J., Loose, M., Zack, T., Barth, M., Worgard,
733 L., Krasz, V., Eby, G.N., Stosnach, H., and others (2012) The volatile inventory
734 (F, Cl, Br, S, C) of magmatic apatite: An integrated analytical approach. Chemical
735 Geology, 291, 241–255.

736 Mason, H.E., McCubbin, F.M., Smirnov, A., and Phillips, B.L. (2009) Solid-state NMR
737 and IR spectroscopic investigation of the role of structural water and F in
738 carbonate-rich fluorapatite. American Mineralogist, 94, 507–516.

739 Mathez, E.A., and Webster, J.D. (2005) Partitioning behavior of chlorine and fluorine in
740 the system apatite-silicate melt-fluid. Geochimica et Cosmochimica Acta, 69,
741 1275–1286.

742 Matsunaga, K., and Kuwabara, A. (2007) First principles study of vacancy formation in
743 hydroxyapatite. Physical Review B, 75, 014102.

744 McCubbin, F.M., Vander Kaaden, K., Tartese, R., Boyce, J.W., Mikhail, S., Whitson,
745 E.S., Bell, A.S., Anand, M., Franchi, I.A., Wang, J., and others (2015)
746 Experimental investigation of F, Cl, and OH partitioning between apatite and Fe-
747 rich basaltic melt at 1.0-1.2 GPa and 950-1000 °C. American Mineralogist, 100,
748 1790–1802.

749 McDade, P., Wood, B.J., van Westrenen, W., Brooker, R., Gudmundsson, G., Soulard,
750 H., Najorka, J., and Blundy, J. (2002) Pressure corrections for a selection of
751 piston-cylinder cell assemblies. Mineralogical Magazine, 66, 1021–1028.

752 Mills, R.D., and Glazner, A.F. (2013) Experimental study on the effects of temperature
753 cycling on coarsening of plagioclase and olivine in an alkali basalt. Contributions
754 to Mineralogy and Petrology, 166, 97–111.

755 Moore, L.R., Gazel, E., Tuohy, R., Lloyd, A.S., Esposito, R., Steele-MacInnis, M., Hauri,
756 E.H., Wallace, P.J., Plank, T., and Bodnar, R.J. (2015) Bubbles matter: An
757 assessment of the contribution of vapor bubbles to melt inclusion volatile budgets.
758 American Mineralogist, 100, 806–823.

759 Morgan, G.B., and London, D. (1996) Optimizing the electron microprobe analysis of
760 hydrous alkali aluminosilicate glasses. American Mineralogist, 81, 1176–1185.

761 Morizet, Y., Brooker, R.A., and Kohn, S.C. (2002) CO_2 in haplo-phonolite melt:
762 solubility, speciation and carbonate complexation. Geochimica et Cosmochimica
763 Acta, 66, 1809–1820.

764 Pan, Y., and Fleet, M.E. (2002) Compositions of the Apatite-Group Minerals:
765 Substitution Mechanisms and Controlling Factors. Reviews in Mineralogy and
766 Geochemistry, 48, 13–49.

767 Peng, G., Luhr, J.F., and McGee, J.J. (1997) Factors controlling sulfur concentrations in
768 volcanic apatite. American Mineralogist, 82, 1210–1224.

769 Peroos, S., Du, Z., and de Leeuw, N.H. (2006) A computer modelling study of the uptake,
770 structure and distribution of carbonate defects in hydroxy-apatite. Biomaterials,
771 27, 2150–2161.

772 Piccoli, P., and Candela, P. (1994) Apatite in felsic rocks: A model for the estimation of
773 initial halogen concentrations in the Bishop Tuff (Long Valley) and Tuolumne
774 Intrusive Suite (Sierra Nevada Batholith) magmas. American Journal of Science,
775 294, 92–135.

776 Potts, N.J., van Westrenen, W., Tart, R., Franchi, I.A., and Anand, M. (2015) Apatite-
777 melt volatile partitioning under lunar conditions. Proceedings of the 46th Lunar
778 and Planetary Science COnference, 1372.

779 Prowatke, S., and Klemme, S. (2006) Trace element partitioning between apatite and
780 silicate melts. Geochimica et Cosmochimica Acta, 70, 4513–4527.

781 Robie, R.A., Hemingway, B.S., and Fisher, J.F. (1978) Thermodynamic properties of
782 minerals and related substances at 298.15 K and 1 bar (10^5 Pascals) pressure and
783 at higher temperature. US Geological Survey Bulletin, 1452.

784 Roeder, P.L., and Emslie, R.F. (1970) Olivine-liquid equilibrium. Contributions to
785 Mineralogy and Petrology, 29, 275–289.

786 Scaillet, B., and Macdonald, R. (2004) Fluorite stability in silicic magmas. Contributions
787 to Mineralogy and Petrology, 147, 319–329.

788 Schettler, G., Gottschalk, M., and Harlov, D.E. (2011) A new semi-micro wet chemical
789 method for apatite analysis and its application to the crystal chemistry of
790 fluorapatite-chlorapatite solid solutions. American Mineralogist, 96, 138-152

791 Shishkina, T.A., Botcharnikov, R.E., Holtz, R., Almeev, R.R., and Portnyagin, M.V.
792 (2010) Solubility of H_2O- and CO_2-bearing fluids in tholeiitic basalts at pressures
793 up to 500 MPa. Chemical Geology, 277, 115-125

794 Sowerby, J.R., and Keppler, H. (1999) Water speciation in rhyolitic melt determined by
795 in-situ infrared spectroscopy. American Mineralogist, 84, 1843–1849.

796 Spilliaert, N., Allard, P., Metrich, N., and Sobolev, A.V. (2006) Melt inclusion record of
797 the conditions of ascent, degassing, and extrusion of volatile-rich alkali basalt
798 during the powerful 2002 flank eruption of Mount Etna (Italy). Journal of
799 Geophysical Research, 111, B04203.

800 Stock, M.J., Humphreys, M.C.S., Smith, V.C., Johnson, R.D., Pyle, D.M., and EIMF
801 (2015) New constraints on electron-beam induced halogen migration in apatite.
802 American Mineralogist, 100, 281–293.

803 Stull, D.R., and Prophet, H. (1971) JANAF thermochemical tables (No. NSRDS-NBS-
804 37). National Standard Reference Data System.

805 Swanson, S.E. (1977) Relation of nucleation and crystal-growth rate to the development
806 of granitic textures. American Mineralogist, 62, 966–978.

807 Trombe, J.C., and Montel, G. (1978) Some features of the incorporation of oxygen in
808 different oxidation states in the apatitic lattice - I. On the existence of calcium and
809 strontium oxyapatites. Journal of Inorganic and Nuclear Chemistry, 40, 15–21.

810 Tuohy, R., Wallace, P.J., Loewen, M.W., Swanson, D.A., and Kent, A.J.R. (2016)
811 Magma transport and olivine crystallization depths in Kilauea's east rift zone
812 inferred from experimentally rehomogenized melt inclusions. Geochimica et
813 Cosmochimica Acta, 185, 232–250.

814 Wallace, P.J. (2005) Volatiles in subduction zone magmas: concentrations and fluxes
815 based on melt inclusion and volcanic gas data. Journal of Volcanology and
816 Geothermal Research, 140, 217–240.

817 Wallace, P.J., Kamenetsky, V.S., and Cervantes, P. (2015) Melt inclusion CO_2 contents,
818 pressures of olivine crystallization, and the problem of shrinkage bubbles.
819 American Mineralogist, 100, 787–794.

820 Webster, J.D. (1990) Partitioning of F between H_2O and CO_2 fluids and topaz rhyolite
821 melt. Implications for mineralizing magmatic-hydrothermal fluids in F-rich
822 granitic systems. Contributions to Mineralogy and Petrology, 104, 424–438.

823 Webster, J.D., Tappen, C.M., and Mandeville, C.W. (2009) Partitioning behavior of
824 chlorine and fluorine in the system apatite–melt–fluid. II: Felsic silicate systems
825 at 200MPa. Geochimica et Cosmochimica Acta, 73, 559–581.

826 Webster, J.D., Goldoff, B.A., Flesch, R.N., Nadeau, P.A., and Silbert, Z.W. (2017)
827 Hydroxyl, Cl, and F partitioning between high-silica rhyolitic melts-apatite-
828 fluid(s) at 50-200 MPa and 700-1000 °C. American Mineralogist, 102, 61–74.

829 Yoder, C.H., Pasteris, J.D., Worcester, K.N., and Schermerhorn, D.V. (2012) Structural
830 water in carbonated hydroxylapatite and fluorapatite: confirmation by solid state
831 ^2H NMR. Calcified Tissue International, 90, 60–67.

832 Young, R.A., Bartlett, M.L., Spooner, S., Mackie, P.E., and Bonel, G. (1981) Reversible
833 high temperature exchange of carbonate and hydroxyl ions in tooth enamel and
834 synthetic hydroxyapatite. Journal of Biological Physics, 9, 1–26.

835 Zhu, C., and Sverjensky, D.A. (1991) Partitioning of F-Cl-OH between minerals and
836 hydrothermal fluids. Geochimica et Cosmochimica Acta, 55, 1837–1858.

837

838

839 Figure 1. Experimental run products from BA experiments showing glass-rich materials
840 and large, equant apatite crystals. Left: BA1 (H-C). Right: BA15 (HCFCl), the most
841 strongly crystallised experiment containing glass + clinopyroxene + apatite.
842
843 Figure 2. Apatite CO_3^{2-} content, expressed as apfu (ions per formula unit) as a function of
844 the CO_2:H_2O ratio of the host melt.
845
846 Figure 3. Apatite carbonate concentrations increase systematically with Mg, Si, and Na
847 contents in apatite. Minor element concentrations, overall, reflect the composition of the
848 host melt. (a) 'BA' haplobasaltic andesite experiments. (b) 'BM' Breccia Museo
849 (trachyte) experiments.
850
851 Figure 4. Partitioning data for H-C exchange between apatite and melt, calculated on the
852 basis of wt% CO_2 and H_2O in both phases. Circles: 'BM' (trachyte) series; squares: 'BA'
853 (haplobasaltic andesite) series. Open symbols are halogen-free experiments. Closed
854 symbols are halogen-bearing experiments. Solid line - best fit; short-dashed line - 95%
855 confidence limits on the fit. Uncertainties on individual data points represent accuracy
856 based on 95% prediction intervals from SIMS working curves (and are much larger than
857 the precision, which is very good).
858
859 Figure 5. Comparison of measured OH contents (pfu) with OH 'by difference' from the
860 sum of the volatile site. Apatite from halogen-bearing experiments (filled symbols) and
861 from halogen-free experiments, but with low carbonate contents, show reasonably good

862 correspondence, whereas the carbonate-rich apatites show a significantly lower measured
863 OH content, indicating the presence of vacancies.
864
865 Figure 6. Nominal partition coefficients for OH, Cl, and F, from this study and from the
866 literature, wt% basis. Grey dashes, Webster et al. (2017); grey crosses, Webster et al.
867 (2009); grey triangles, Doherty et al. (2014); open circles, Mathez and Webster et al.
868 (2005); filled circles, McCubbin et al. (2015); pluses, Potts et al. (2015). Black diamonds
869 - 'BA' experiments; black squares - 'BM' experiments.
870
871 Figure 7. Experimentally derived distribution coefficients for OH-halogen exchange
872 between apatite and silicate melt (calculated on a wt% basis), in comparison with K_Ds
873 from the literature. Symbols are the same as for Figure 6.
874
875 Figure 8. Regression analyses of experimentally determined halogen-OH distribution
876 coefficients for apatite-melt (wt% basis), with dependence on both P and T ($\log K_D = a +$
877 $b/T + c(P-1)/T$) or temperature only ($\log K_D = a + b/T$). Regression coefficients for T-only
878 analysis are given. Data symbols are the same as for Figure 6. Dark grey lines, predicted
879 variations at 1 GPa (solid) and 50 MPa (dashed). Light grey lines, predicted variations for
880 the system apatite-fluid from Piccoli and Candela (1994) at 1 GPa (dashed) and 50 MPa
881 (dotted). Black dotted line shows the T-only regression. Grey fields show the
882 experimental range of Li and Hermann (2017; 2.5 GPa). Dashed light grey outlines show
883 the experimental range of Li and Hermann (2015; 2.5-4.5 GPa).
884

885 Supplementary Figure 1. Infrared spectra of the carbonate region in apatite from sample
886 BA7. Melt and apatite spectra were acquired from grains mounted in In metal, using an
887 ATR attachment on a Nicolet i10 infrared microscope with the signal coming from a
888 ~8μm area. The CHAP (carbonate-bearing hydroxyapatites) spectra are from Fleet (2017)
889 who used powered samples in a KBr pellet. The AB CHAP is reported to have 66%
890 carbonate on the A site, the rest on the B site. A CHAP is pure A site carbonate. It is clear
891 that sample BA7 is dominated by A-site carbonate with only a very minor contribution
892 from B-site carbonate.
893

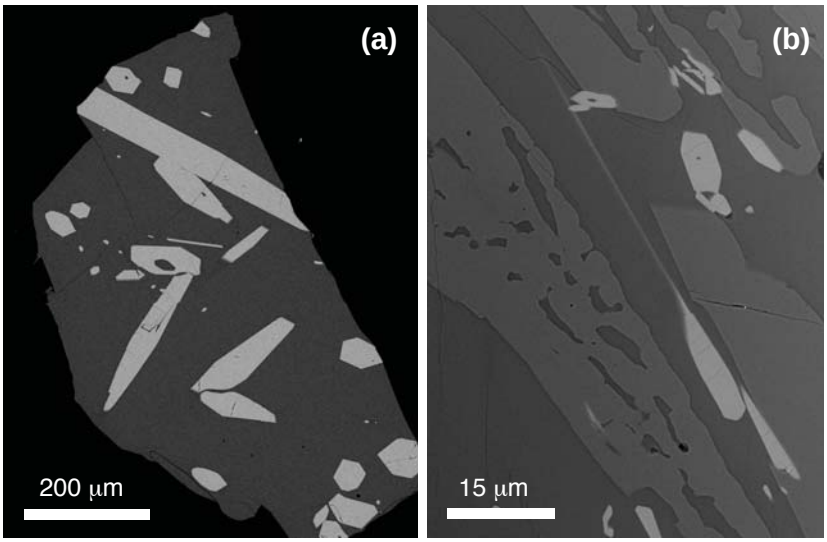

Figure 1
Experimental run products from BA experiments, showing glass-rich materials and large, equant apatite crystals. Left: BA1 (H-C). Right: BA15 (HCFCl), the most strongly crystallised experiment containing glass + clinopyroxene + apatite.

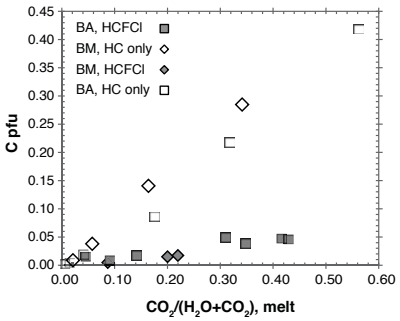

Figure 2.
Variation of apatite CO_3^{2-} content (ions per formula unit) as a function of the CO_2:H_2O ratio of the host melt.

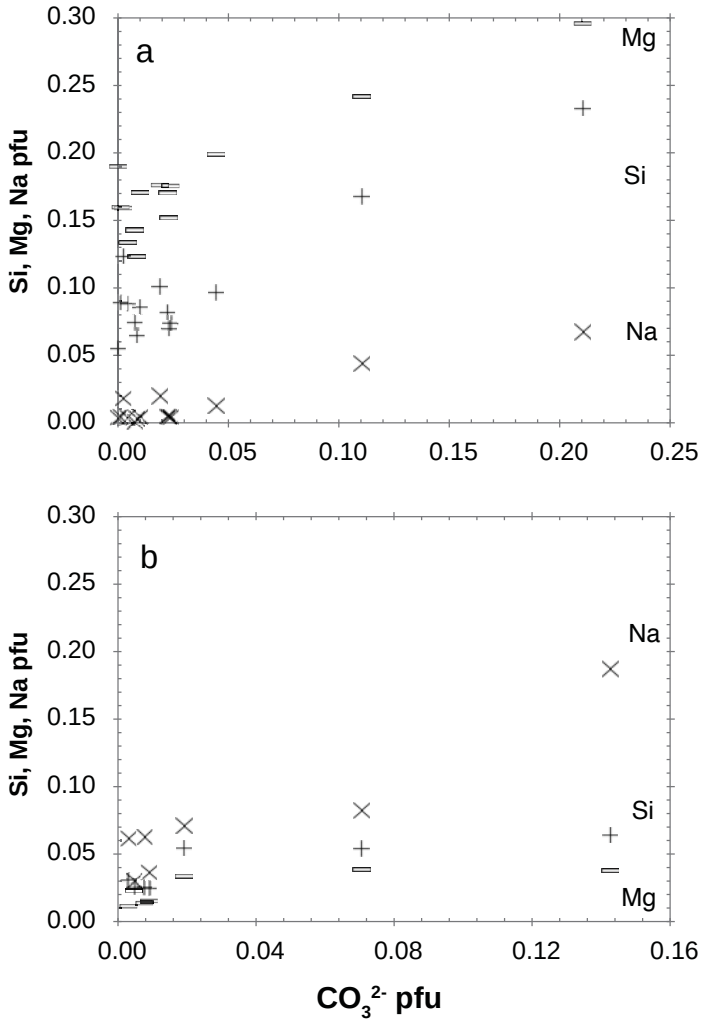

Figure 3.
Apatite carbonate concentrations increase systematically with Mg, Si and Na contents in apatite. Minor element concentrations overall reflect the composition of the host melt. (a) 'BA' haplo-basaltic andesite experiments. (b) 'BM' Breccia Museo (trachyte) experiments.

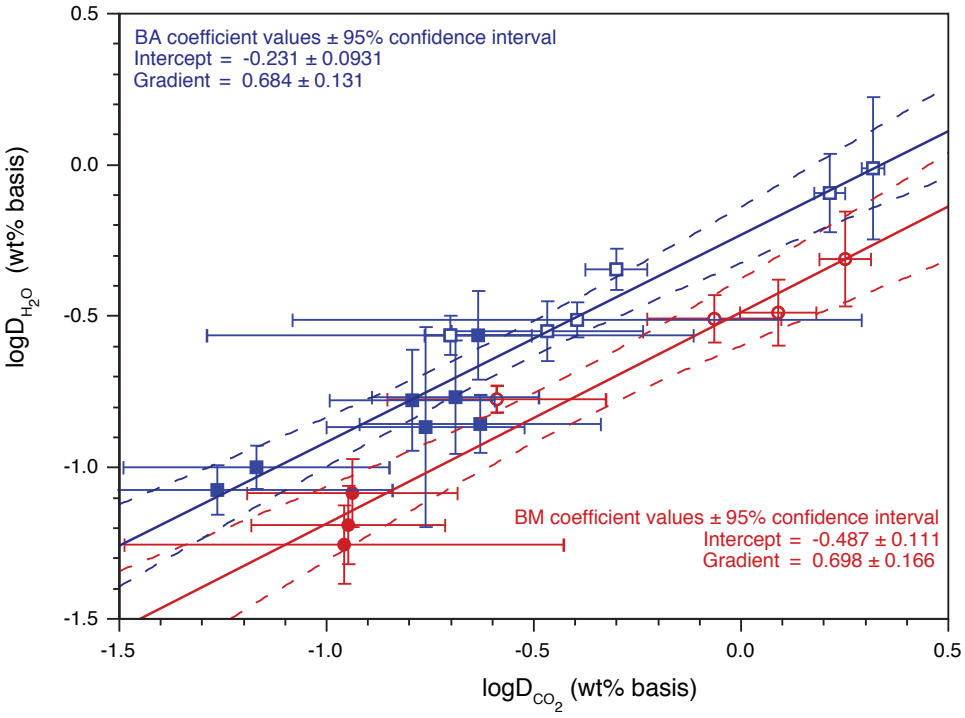

Figure 4.
Partitioning data for H-C exchange between apatite and melt, calculated on basis of wt% CO_2 and H_2O in both phases. Circles: 'BM' (trachyte) series; squares: 'BA' (haplo-basaltic andesite) series. Open symbols are halogen-free experiments; closed symbols are halogen-bearing experiments. Solid line - best fit; short-dashed line - 95% confidence limits on the fit.

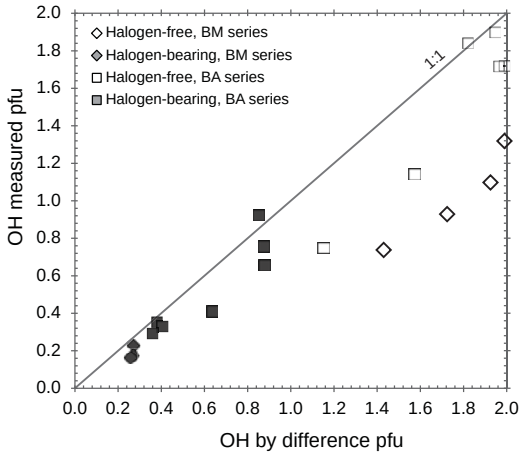

Figure 5
Comparison of measured OH contents (pfu) with OH 'by difference' from the sum of the volatile site. Apatite from halogen-bearing experiments (filled symbols) and from halogen-free experiments but with low carbonate contents show reasonably good correspondence, whereas carbonate-rich apatites show a significantly lower measured OH, indicating the presence of vacancies.

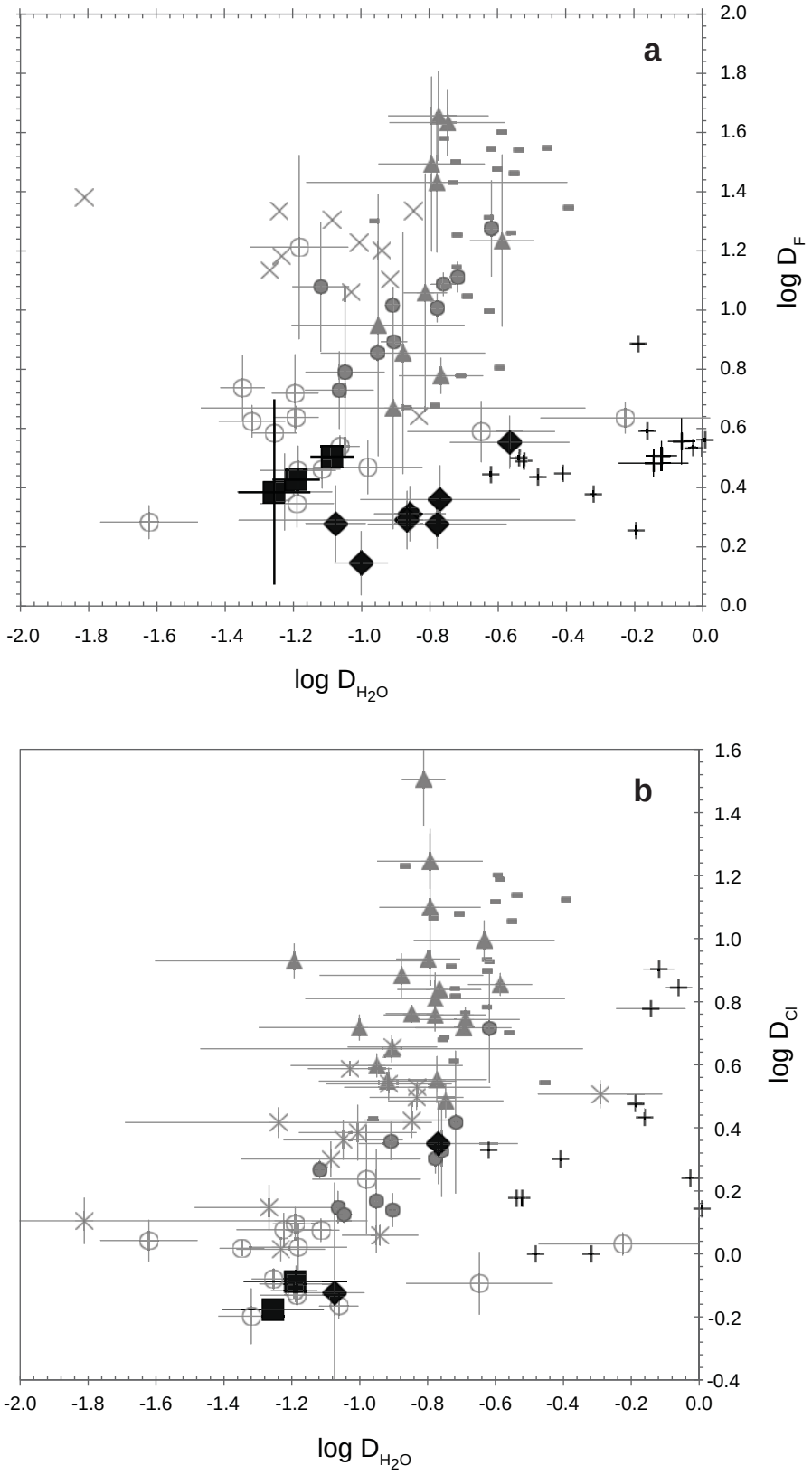

Figure 6.
Nominal partition coefficients for OH, Cl and F, from this study and from the literature, wt% basis. Grey dashes, Webster et al. (2017); grey crosses, Webster et al. (2009); grey triangles, Doherty et al. (2014); open circles, Mathez & Webster et al. (2005); filled circles, McCubbin et al. (2015); pluses, Potts et al. (2015). Black diamonds - 'BA' experiments; black squares - 'BM' experiments.

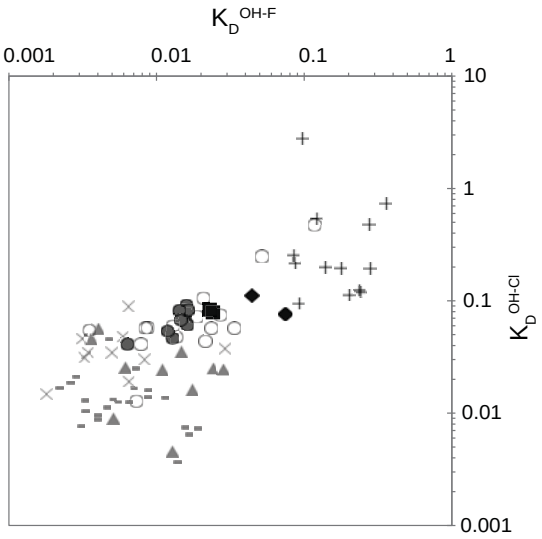

Figure 7.
Experimentally derived distribution coefficients for OH-halogen exchange between apatite and silicate melt (calculated on wt% basis), in comparison with K_Ds from the literature. Symbols as for figure 6.

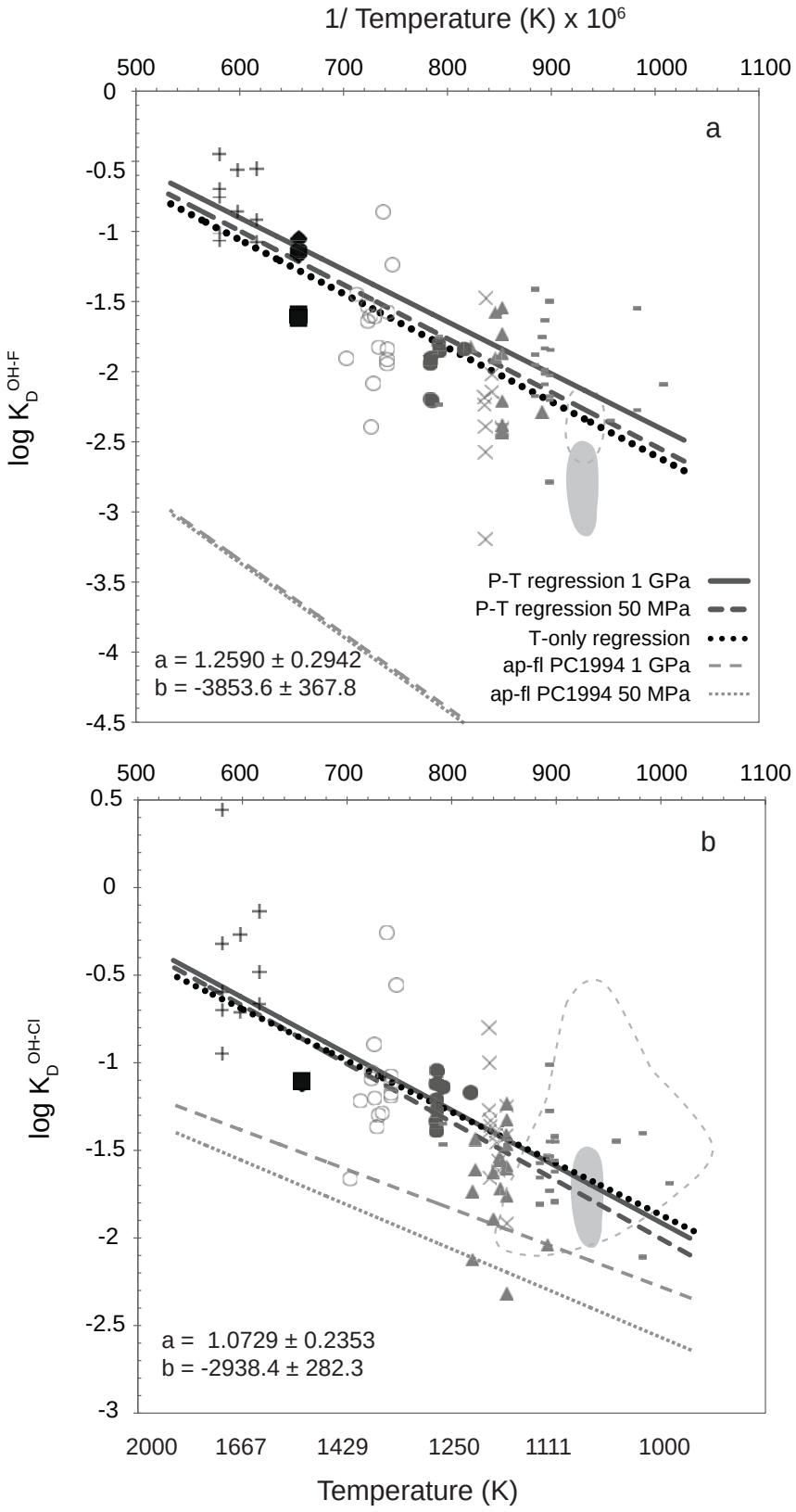

Figure 8. Regression analyses of experimentally determined halogen-OH distribution coefficients for apatite-melt (wt% basis), with dependence on both P and T ($\log K_D = a + b/T + c(P-1)/T$) or temperature only ($\log K_D = a + b/T$). Regression coefficients for T-only analysis are given. Data symbols as for figure 6. Dark grey lines, predicted variations at 1 GPa (solid) and 50 MPa (dashed). Light grey lines, predicted variations for the system apatite-fluid from Piccoli & Candela (1994) at 1 GPa (dashed) and 50 MPa (dotted). Black dotted line shows the T-only regression. Grey fields show the experimental range of Li & Hermann (2017; 2.5 GPa). Dashed light grey outlines show the experimental range of Li & Hermann (2015; 2.5-4.5 GPa).

Table 1: Target compositions for starting materials

	SH3 Prowatke & Klemme (2006)	**BM** Fabbrizio & Carroll (2008)
SiO2	53.50	62.20
TiO2		0.45
Al2O3	17.70	18.71
FeO		3.19
MgO	11.80	0.23
MnO		0.27
CaO	12.40	1.65
Na2O	2.80	6.16
K2O	1.80	7.14
Total =	100.00	100.00

Table 2: experimental run conditions

		Nominal bulk volatile contents added															
Run	Starting material(s)	Ca3(PO4)2 added (wt%)	H2O (wt%)	CO2 (wt%)	F (wt%)	Cl (wt%)	F source	Cl source	Notes	P GPa	T init (°C)	T final (°C)	Cooling rate (°C/hr)	Initial dwell time (mins)	Cooling time (hrs)	Final dwell time (mins)	Phases present	Notes
BA1	SH3	25	5							1	1450	1250	50	104	4	15	gl + ap ± cpx	
BA2	SH3/SH3C	25	3	0.2						1	1450	1250	50	74	4	16	gl + ap ± ?	
BA4	SH3/SH3C	25	1	0.4					15 cycles ± 10 °C @ 1 °C/min	1	1500	1250	20	60	12.5	11	gl + ap	
BA7	SH3/SH3C	25		0.5						1	1500	1250	10	120	25	15	gl + ap	
BA13	SH3 (glassed)	25	5							1	1450	1250	50	120	4	15	gl + ap	
BA16	SH3/SH3C	25	1	0.4					11 cycles ± 10 °C @ 1 °C/min. Doped with 3000 ppm Y	1	1500	1250	20	60	12.5	10	gl + ap	
BA3	SH3	25	5		1		CaF2			1	1450	1250	50	120	4	15	gl + ap	
BA6	SH3/SH3C	25	1	0.4	1		CaF2		8 cycles ± 10 °C @ 1 °C/min	1	1500	1250	20	60	12.5	12	gl + ap	
BA9 (rpt)	SH3	25	5		2		1 wt% CaF2 and 1 wt% KF			1	1450	1250	20	120	10	11	gl + ap	
BA10	SH3/SH3C	10	1	0.4	1		CaF2		4 cycles ± 10 °C @ 1 °C/min	1	1500	1250	20	60	12.5	12	gl ± ap	
BA11	SH3/SH3C	25	1	0.4	2		CaF2			1	1500	1250	20	60	12.5	11	gl + ap	
BA15	SH3/SH3C	5	1	0.4	1		CaF2			1	1400	(1250)	4	120	32	62	gl + cpx ± ap	
BA12	SH3/SH3C	25	1	0.4	1	1	CaF2	CaCl2	13 cycles ± 10 °C @ 1 °C/min	1	1500	1250	20	60	12.5	10	gl + ap	
BA14	SH3	25	5		1	1	CaF2	CaCl2		1	1450	1250	50	120	4	17	gl + ap	
BM10	BMP25	25	5							1	1450	1250	50	120	4	15	gl + ap	
BM11	BMCP25	25		1.0					6 cycles ± 10 °C @ 1 °C/min. Dwel time > 19 hours	1	1500	1250	10	1169	25	9	gl + ap	Ap skeletal/ hopper forms
BM12	BMCP25-5000	25	1	0.5						1	1500	1250	20	60	12.5	10	gl + ap	
BM13	BMCP25-5000	25	1	0.5	1		NaF			1	1500	1250	20	60	12.5	9	gl + ap	
BM14	BMCP25-5000	25	1	0.5	1	1	NaF	NaCl		1	1500	1250	20	60	12.5	12	gl + ap	
BM15	BMCP25-5000	25	1	0.5					3/4" talc-pyrex	0.5	1500	1250	20	60	12.5	11	gl + ap	Just volatile-saturated?
BM16	BMCP25-5000	25	1	0.5	1	1	NaF	NaCl	3/4" talc-pyrex	0.5	1500	1250	20	60	12.5	10	gl + ap	Just volatile-saturated

Table 3: Apatite compositions and formula calculations.

Experiment		BA1	BA2	BA4	BA7	BA13	BA16	BA3	BA6	BA9	BA10	BA11
Experiment type		**H(-C)**	**H-C**	**H-C**	**(H-)C**	**H(-C)**	**H-C**	**H-F(-C)**	**H-F-C**	**H-F(-C)**	**H-F-C**	**H-F-C**
	n	11	2	8	7	9	9	8	7	9	4	10
Oxide from EPMA (wt %)	**F**							2.19 (24)	3.04 (72)	2.62 (31)	3.04 (34)	3.43 (40)
	Cl											
	Na_2O		0.04 (02)	0.13 (03)	0.20 (03)							
	Al_2O_3				0.09 (03)							
	MgO	0.68 (06)	0.80 (13)	0.96 (07)	1.16 (15)	0.64 (08)	0.63 (08)	0.58 (06)	0.70 (12)	0.51 (06)	0.74 (08)	0.63 (06)
	SiO_2	0.51 (03)	0.58 (03)	0.99 (04)	1.36 (05)	0.53 (04)	0.73 (06)	0.45 (06)	0.50 (03)	0.40 (02)	0.46 (06)	0.44 (02)
	CaO	53.64	53.42	52.95	52.28	55.15	54.42	54.40	54.15	55.35	55.13	55.45
	P_2O_5	41.93	42.32	41.32	40.37	41.79	41.38	41.89	41.68	42.11	42.93	41.92
	Fe											
	Mn											
SIMS	**Y_2O_3**						1.72					
	Total	96.76	97.15	96.36	95.48	98.12	98.89	99.52	100.08	100.98	102.31	101.87
Oxide from SIMS (wt%)	**H_2O**	1.69 (04)	1.65 (03)	1.01 (04)	0.66 (04)	1.54 (12)	1.53 (12)	0.83 (04)	0.31 (04)	0.69 (11)	0.38 (09)	0.31 (11)
	CO_2	0.09 (06)	0.39 (04)	0.97 (03)	1.80 (01)	0.012 (05)	0.017 (05)	0.067 (06)	0.20 (05)	0.076 (05)	0.27 (05)	0.21 (05)
	F							2.12 (38)	2.93 (38)	2.10 (48)	2.52 (39)	2.95 (48)
	Cl											
Less O = F, Cl	**F,Cl = O ***							0.89	1.23	0.88	1.06	1.24
	Recalc Total	**98.54**	**99.19**	**98.34**	**97.97**	**99.67**	**98.72**	**99.45**	**99.25**	**100.35**	**101.33**	**100.67**
Ions Per Formula Unit (25 oxygen basis)												
Ca site	**Na**		0.013	0.044	0.067							
	Al				0.019							
	Mg	0.171	0.199	0.242	0.296	0.160	0.158	0.146	0.176	0.127	0.181	0.157
	Mn											
	Fe											
	Y						0.153					
	Ca	9.692	9.591	9.600	9.574	9.877	9.740	9.797	9.781	9.885	9.717	9.904
	Sum Ca site	*9.863*	*9.803*	*9.886*	*9.956*	*10.037*	*10.050*	*9.943*	*9.957*	*10.011*	*9.898*	*10.062*
P site	**P**	5.986	6.004	5.920	5.841	5.914	5.851	5.962	5.949	5.942	5.980	5.917
	Si	0.086	0.097	0.168	0.233	0.089	0.123	0.076	0.085	0.067	0.076	0.073
	C						0.005					0.010
	Sum P site	*6.072*	*6.101*	*6.088*	*6.074*	*6.003*	*5.978*	*6.038*	*6.034*	*6.009*	*6.056*	*6.010*
X site	**C**	0.020	0.089	0.221	0.421	0.002		0.015	0.046	0.017	0.049	0.037
	F							1.127	1.562	1.107	1.311	1.555
	Cl											
	OH (measured)	1.899	1.841	1.142	0.748	1.7197938	1.702	0.935	0.352	0.765	0.419	0.340
	OH (by difference)	1.960	1.822	1.558	1.158	1.995	1.991	0.858	0.392	0.875	0.640	0.407
	Sum X site	*1.92*	*1.93*	*1.36*	*1.17*	*1.72*	*1.70*	*2.08*	*1.96*	*1.89*	*1.78*	*1.93*

Notes: Values in parentheses give 2 sd analytical uncertainty (but for SIMS measurements, 95% prediction intervals).
Formula recalculations are done using F determined by SIMS and Cl determined by EPMA. See text for details of cation site assignments.

BA15	BA12	BA14	BM10	BM11	BM12	BM15	BM13	BM14	BM16
H-F-C	**H-F-C-Cl**	**H-F(-C)-Cl**	**H(-C)**	**H-C**	**H-C**	**H-C 0.5 GPa**	**H-F-C**	**H-F-C-Cl**	**H-F-C-Cl 0.5 GPa**
	8	8	12	11	9	10	9	10	12
3.53 (08)	2.22 (28)	1.97 (22)					3.27 (70)	2.68 (62)	2.83 (64)
	1.74 (09)	0.62 (06)						1.02 (10)	0.84 (10)
	0.06 (02)		0.09 (08)	0.57 (14)	0.25 (10)	0.22 (09)	0.12 (08)	0.20 (08)	0.20 (08)
0.81 (08)	0.73 (06)	0.55 (07)	0.09 (04)	0.15 (04)	0.15 (04)	0.13 (04)	0.06 (04)	0.06 (04)	0.05 (04)
0.35 (06)	0.62 (02)	0.54 (04)	0.16 (04)	0.38 (04)	0.32 (04)	0.32 (04)	0.15 (04)	0.15 (04)	0.19 (04)
55.19	54.78	55.42	55.17	54.12	54.43	54.61	55.67	54.98	55.23
43.17	41.55	41.77	42.89	42.05	42.27	41.78	42.86	42.07	42.20
			0.21 (10)		0.20 (10)	0.21 (10)	0.16 (10)	0.15 (10)	0.13 (10)
			0.15 (10)	0.09 (08)	0.21 (10)	0.19 (08)	0.09 (08)	0.08 (08)	0.07 (08)
103.04	101.70	100.87	98.76	97.37	97.84	97.47	102.38	101.38	101.72
	0.27 (11)	0.59 (11)	1.19 (04)	0.66 (04)	0.83 (04)	0.98 (04)	0.21 (04)	0.16 (04)	0.15 (04)
	0.17 (05)	0.038 (05)	0.04 (04)	1.24 (05)	0.62 (05)	0.17 (04)	0.082 (04)	0.069 (04)	0.027 (04)
	2.08 (48)	1.77 (48)					2.81 (58)	2.27 (35)	2.36 (35)
	1.82 (52)	0.65 (52)						0.93 (49)	0.75 (49)
1.49	1.29	0.89					1.18	1.18	1.18
101.55	**100.73**	**100.42**	**99.99**	**99.27**	**99.29**	**98.62**	**101.03**	**100.02**	**100.25**
	0.021		0.03	0.19	0.08	0.07	0.04	0.06	0.06
	0.000		0.00	0.00	0.00	0.00	0.00	0.00	0.00
	0.182	0.137	0.02	0.04	0.04	0.03	0.02	0.01	0.01
			0.02	0.01	0.03	0.03	0.01	0.01	0.01
			0.03	0.00	0.03	0.03	0.02	0.02	0.02
	9.846	9.917	9.80	9.75	9.77	9.86	9.87	9.90	9.91
	10.048	*10.054*	*9.91*	*9.99*	*9.95*	*10.02*	*9.96*	*10.01*	*10.01*
	5.901	5.906	6.02	5.99	5.99	5.96	6.00	5.99	5.98
	0.105	0.090	0.03	0.06	0.05	0.05	0.03	0.03	0.03
		0.004							
	6.006	*6.004*	*6.05*	*6.05*	*6.05*	*6.02*	*6.03*	*6.01*	*6.01*
	0.039	0.005	0.01	0.29	0.14	0.04	0.02	0.02	0.01
	1.103	0.935					1.71	1.43	1.50
	0.495	0.176						0.29	0.24
	0.299	0.663	1.32	0.74	0.93	1.10	0.23	0.18	0.17
	0.363	0.884	1.98	1.43	1.72	1.92	0.27	0.27	0.26
	1.94	*1.78*	*1.33*	*1.02*	*1.07*	*1.14*	*1.96*	*1.91*	*1.91*

Table 4. Average major element composition (EPMA) and volatile contents (H_2O and CO_2, SIMS) of experimental glasses

Electron microprobe composition (wt%)

Sample	F	Na_2O	Al_2O_3	MgO	SiO_2	K_2O	CaO	P_2O_5	Cl	TiO_2	FeO	MnO	H_2O	CO_2	Y_2O_3	Total	n
BA1_avg		2.63	14.35	9.38	44.50	1.40	16.57	3.70					5.96	0.25		98.75	14
BA2_avg		2.99	16.31	8.58	45.59	1.68	15.66	4.11					3.65	0.77		99.34	12
BA4_avg		2.72	14.88	9.64	45.36	1.46	18.21	4.80					1.25	0.58		98.90	14
BA7_avg		2.63	14.54	9.49	44.97	1.39	18.71	5.38					0.67	0.87		98.65	14
BA13_avg		2.50	14.88	9.51	45.10	1.21	17.10	3.89					5.03	0.03		99.25	14
BA16_avg		2.40	14.01	8.77	43.21	1.29	17.69	5.20					5.60	0.09	0.68	98.94	14
BA3_avg	1.02	2.61	14.03	9.11	43.84	1.36	17.88	3.63					5.99	0.29		99.76	14
BA6_avg	0.81	2.74	15.17	9.83	46.30	1.48	18.32	3.32					1.15	0.86		99.98	11
BA9_avg	1.50	2.37	13.86	8.90	41.95	2.59	17.65	3.86					4.29	0.96		97.93	14
BA10_avg	1.03	2.46	15.20	9.74	45.55	1.44	17.18	3.60					2.80	1.26		100.26	14
BA11_avg	1.56	2.56	14.84	9.47	45.24	1.38	18.82	3.40					1.83	1.30		100.40	14
BA12_avg	0.91	2.63	14.97	9.61	45.54	1.40	18.70	3.29	0.78				1.57	0.83		100.23	14
BA14_avg	0.93	2.34	13.50	8.69	41.42	1.26	18.97	4.70	0.83				7.06	0.71		100.41	14
BM10_avg		5.49	16.72	0.31	55.42	6.12	3.29	1.92		0.39	2.07	0.21	7.08	0.16		99.18	10
BM11_avg		7.65	18.39	0.30	60.76	6.61	2.43	1.08		0.43			1.34	0.70		99.69	10
BM12_avg		6.65	17.22	0.28	57.08	6.28	3.16	1.73		0.40	3.38	0.20	2.56	0.50		99.45	10
BM15_avg		6.75	17.38	0.29	57.63	6.37	3.05	1.51		0.41	2.90	0.18	3.15	0.19		99.82	10
BM13_avg	0.88	9.04	16.90	0.29	56.04	6.23	2.79	1.40		0.39	3.00	0.24	2.52	0.71		100.43	10
BM14_avg	0.85	9.85	16.44	0.30	54.23	6.02	3.18	1.73	1.24	0.37	2.91	0.19	2.43	0.61		100.36	10
BM16_avg	0.97	10.09	16.51	0.29	54.49	5.80	3.05	1.68	1.26	0.39	2.98	0.21	2.68	0.25		100.64	10

[a] normalised to 100% anhydrous

EPMA counting statistics, 1σ wt% (H_2O, CO_2 uncertainties represent 95% prediction interval, see supplementary information)

SiO_2 [a]	Total alkalis	Sample	F	Na_2O	Al_2O_3	MgO	SiO_2	K_2O	CaO	P_2O_5	Cl	TiO_2	FeO	MnO	H_2O	CO_2
48.09	4.35	**BA1_avg**		0.24	0.47	0.28	0.77	0.22	0.6	0.2					0.52	0.049
48.03	4.92	**BA2_avg**		0.26	0.52	0.26	0.78	0.25	0.57	0.21					0.47	0.057
46.73	4.31	**BA4_avg**		0.25	0.48	0.29	0.78	0.23	0.65	0.23					0.44	0.053
46.31	4.14	**BA7_avg**		0.24	0.47	0.28	0.77	0.22	0.66	0.24					0.43	0.059
47.88	3.94	**BA13_avg**		0.21	0.5	0.3	0.54	0.14	0.44	0.29					0.45	0.057
46.68	3.99	**BA16_avg**		0.21	0.47	0.28	0.52	0.15	0.45	0.33					0.46	0.058
47.42	4.25	**BA3_avg**	0.151	0.24	0.46	0.27	0.76	0.22	0.64	0.2					0.52	0.049
47.65	4.30	**BA6_avg**	0.141	0.25	0.49	0.29	0.79	0.23	0.65	0.19					0.44	0.059
46.01	5.35	**BA9_avg**	0.146	0.22	0.49	0.26	0.83	0.29	0.81	0.23					0.47	0.079
47.86	4.06	**BA10_avg**	0.124	0.22	0.54	0.28	0.91	0.23	0.81	0.22					0.42	0.086
47.27	4.05	**BA11_avg**	0.153	0.23	0.53	0.27	0.9	0.22	0.88	0.21					0.41	0.087
46.99	4.12	**BA12_avg**	0.12	0.23	0.53	0.27	0.91	0.22	0.29	0.21	0.056				0.41	0.076
45.16	3.88	**BA14_avg**	0.11	0.2	0.46	0.28	0.5	0.14	0.47	0.31	0.062				0.47	0.073
60.28	12.63	**BM10_avg**		0.788	0.46	0.41	0.05	0.05	0.14	0.18		0.27	0.1	0.09	0.62	0.044
62.22	14.61	**BM11_avg**		0.85	0.5	0.43	0.05	0.05	0.12	0.13		0.09			0.62	0.048
59.22	13.42	**BM12_avg**		0.81	0.48	0.42	0.05	0.05	0.13	0.17		0.35	0.11	0.09	0.62	0.047
59.74	13.60	**BM15_avg**		0.8	0.82	0.48	0.06	0.43	0.13	0.16		0.051	0.32	0.11	0.62	0.044
58.18	15.71	**BM13_avg**	0.14	0.99	0.8	0.47	0.42	0.05	0.05	0.12		0.024	0.32	0.11	0.63	0.048
56.22	16.31	**BM14_avg**	0.14	1.07	0.78	0.46	0.06	0.42	0.13	0.17	0.098	0.05	0.32	0.11	0.62	0.048
56.32	16.27	**BM16_avg**	0.15	1.09	0.79	0.46	0.06	0.41	0.13	0.17	0.098	0.05	0.33	0.11	0.62	0.045

Table 5 - Apatite-melt volatile experimental partitioning data.

			Mole fraction apatite volatiles				Mole fraction melt volatiles			Nominal apatite-melt partition coefficients (			
Experiment		Analytical session[a]	XF ap	XCl ap	XOH ap	XCO_3 ap	XOH m	XF melt	XCl melt	DH_2O	±	DCO_2	±
BA1	H-C	1			0.983	0.010	0.151			0.283	*0.072*	0.341	*0.24*
BA2	H-C	1			0.934	0.045	0.106			0.452	*0.078*	0.501	*0.10*
BA4	H-C	1			0.818	0.158	0.044			0.809	*0.284*	1.639	*0.15*
BA7	H-C	1			0.616	0.347	0.025			0.974	*0.697*	2.084	*0.13*
BA13	H-C	2			0.995	0.001	0.135			0.307	*0.045*	0.383	*1.55*
BA16	H-C	2			0.982	0.003	0.145			0.273	*0.043*	0.199	*0.57*
BA3	H-F-C	1	0.550		0.442	0.007	0.152	0.019		0.139	*0.034*	0.235	*0.22*
BA6	H-F-C	1	0.801		0.174	0.023	0.040	0.016		0.273	*0.110*	0.232	*0.08*
BA9	H-F-C	2	0.638		0.354	0.008	0.166	0.028		0.100	*0.018*	0.067	*0.07*
BA10	H-F-C	2	0.770		0.204	0.024	0.086	0.020		0.136	*0.155*	0.214	*0.13*
BA11	H-F-C	2	0.826		0.156	0.016	0.061	0.031		0.167	*0.078*	0.158	*0.09*
BA12	H-F-C-Cl	2	0.586	0.246	0.149	0.019	0.053	0.018	0.015	0.171	*0.092*	0.202	*0.12*
BA14	H-F-C-Cl	2	0.551	0.094	0.353	0.002	0.169	0.017	0.015	0.0843	*0.017*	0.0538	*0.09*
BM10	H	3			0.987	0.007	0.169			0.169	*0.018*	0.257	*0.214*
BM11	C	3			0.709	0.275	0.046			0.488	*0.213*	1.783	*0.276*
BM12	H-C	3			0.853	0.130	0.081			0.324	*0.091*	1.226	*0.286*
BM15	H-C 0.5 GPa	3			0.953	0.033	0.095			0.310	*0.061*	0.861	*0.386*
BM13	H-F-C	3	0.874		0.117	0.009	0.079	0.017		0.082	*0.025*	0.115	*0.092*
BM14	H-F-C-Cl	3	0.748	0.152	0.092	0.008	0.077	0.017	0.025	0.064	*0.022*	0.113	*0.080*
BM16	H-F-C-Cl 0.5 GPa	3	0.785	0.124	0.087	0.003	0.083	0.019	0.025	0.056	*0.019*	0.110	*0.263*

Notes: 1 sigma uncertainties relate to the variability of multiple analyses within a given sample. Mole fraction apatite volatile compositions are calculated from stoichiometry a Uncertainties on the partition coefficients are calculated by standard error propagation methods. Melt mole fraction calculations were done using the method of Li & Hermann Molecular weight of 36.1g was used for both halogen-bearing compositions. Water speciation is calculated using Hui et al. (2008).

[a] Analytical session refers to the calibration data provided in the supplementary information. 95% prediction intervals provided are also derived from this.

wt% basis)				Apatite-melt K_Ds (wt% basis)						Apatite-melt K_Ds (mole fraction basis)	
DF	±	DCl	±	K_D H_2O-CO_2	±	K_D H_2O-F	±	K_D H_2O-Cl	±	K_D OH-F	K_D OH-Cl
				0.830	*0.62*						
				0.901	*0.23*						
				0.493	*0.18*						
				0.467	*0.34*						
				0.802	*3.26*						
				1.368	*3.93*						
2.052	*0.44*			0.592	*0.58*	0.068	*0.02*			0.102	
3.577	*0.74*			1.178	*0.63*	0.076	*0.03*			0.087	
1.398	*0.35*			1.489	*1.66*	0.072	*0.02*			0.094	
1.954	*0.44*			0.638	*0.82*	0.070	*0.08*			0.061	
1.891	*0.36*			1.057	*0.79*	0.088	*0.04*			0.096	
2.290	*0.61*	2.342	*0.69*	0.846	*0.68*	0.074	*0.04*	0.073	*0.04*	0.086	0.17
1.900	*0.56*	0.786	*0.63*	1.566	*2.63*	0.044	*0.02*	0.107	*0.09*	0.066	0.34
				0.656	*0.55*						
				0.274	*0.13*						
				0.264	*0.10*						
				0.360	*0.18*						
3.198	*0.83*			0.713	*0.61*	0.026	*0.01*			0.029	
2.675	*0.61*	0.746	*0.40*	0.572	*0.45*	0.024	*0.01*	0.086	*0.05*	0.026	0.20
2.426	*0.52*	0.599	*0.39*	0.505	*1.22*	0.023	*0.01*	0.093	*0.07*	0.025	0.21

nd normalised assuming X-site total = 1.0 (to aid comparison with published studies).
(2017) using molecular weights of 35.42g and 34.15g for halogen-free BA and BM melts, respectively.

Table 6 - Summary of multiple regression results for literature dataset of OH-halogen K_Ds

Equation 1, $\log K_D = a + b/T + c(P-1)/T$

	OH-F	±	OH-Cl	±
a	1.33	0.2907	1.333	0.234
b	-3864	361	-3344	288
c	0.01532	0.007218	0.01038	0.002746

Equation 2, $\log K_D = a + b/T$

	OH-F	±	OH-Cl	±
a	1.259	0.2942	1.0729	0.2353
b	-3853.6	368	-2938	282

Table 7 - summary of experimental conditions for studies included in multiple regression analysis.

Reference	Bulk composition	Melt CaO (wt%)	T (°C)	P (MPa)	Apatite measured	Melt measured	Fluid measured	Volatile state
This study	Haplo-basaltic andesite	15 7 - 19.0	1250	1000	OH, F, Cl, C (SIMS); F, Cl (EPMA)	H_2O, F, Cl, C (SIMS); F, Cl (EPMA)	n/a	Volatile-undersaturated
This study	Trachyte	2.4 - 3.3	1250	1000	OH, F, Cl, C (SIMS); F, Cl (EPMA)	H_2O, F, Cl, C (SIMS); F, Cl (EPMA)	n/a	Volatile-undersaturated
Doherty et al. (2014)	Rhyodacite	0.4 - 3.1	849 - 947	50 - 52	F, Cl (EPMA)	H_2O (FTIR); F, Cl (EPMA)	Cl (mass balance)	Mostly volatile-saturated
Li & Hermann (2015)	Pelite	2.3 - 2.5	630 - 900	2500-4500	F, Cl (EPMA)	F, Cl (EPMA); H_2O (mass balance)	n/a	Volatile-undersaturated
Li & Hermann (2017)	Pelite	2.4	800	2500	F, Cl (EPMA)	F, Cl (EPMA); H_2O (mass balance)	n/a	Volatile-undersaturated
Mathez & Webster (2005)	Basalt	5.3 - 16.9	1066 - 1150	200	F, Cl (EPMA)	F, Cl (EPMA)	Cl (chloridometer)	Mostly volatile-saturated
McCubbin et al. (2014)	Fe-rich basalt	3.8 - 9.0	950 - 1000	1000 - 1200	OH, F, Cl (SIMS)	H_2O, F, Cl (SIMS)	n/a	Volatile-undersaturated
Potts et al. (2015)	Lunar basalt mesostasis	8.0 - 9.0	1350 - 1450	1000	OH, F, Cl (SIMS)	H_2O, F, Cl (SIMS)	n/a	Volatile-undersaturated
Webster et al. (2009)	Rhyodacite to rhyolite	0.5 - 2.4	900 - 923	198 - 205	F, Cl (EPMA)	F, Cl (EPMA)	Cl (chloridometer)	Volatile-saturated
Webster et al. (2017) [a]	High-Si rhyolite	0.1 - 2.1	722 - 1000	49 - 202	F, Cl (EPMA)	H_2O (FTIR); F, Cl (EPMA)	Cl (chloridometer)	Volatile-saturated

[a] *These runs typically contained <25 ppm CO_2 as contaminant (not studied)*

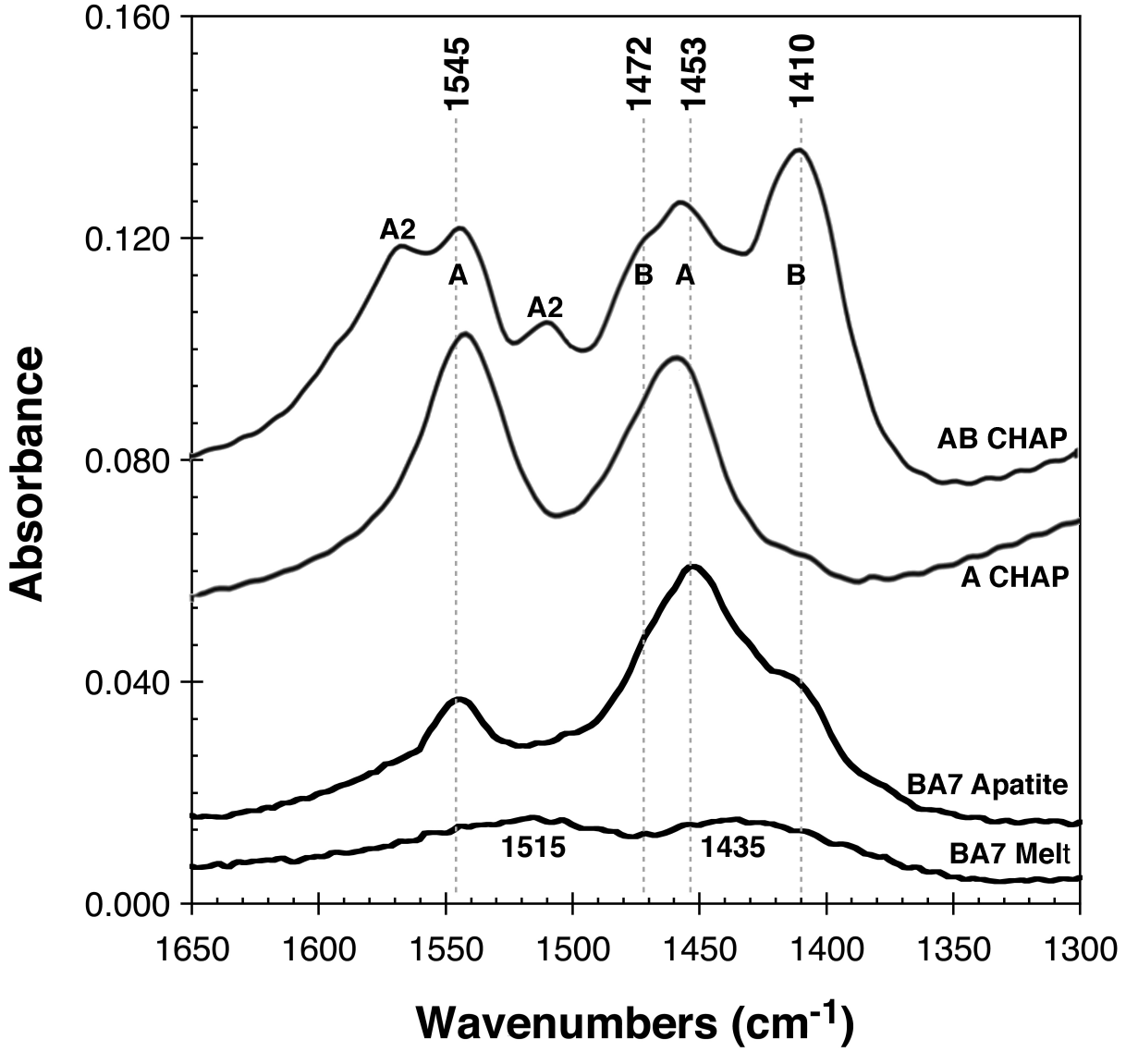
0.160
0.120
0.080
0.040
0.000
Absorbance
1545
1472
1453
1410
A2
A
A2
B
A
B
AB CHAP
A CHAP
BA7 Apatite
BA7 Melt
1515
1435
1650
1600
1550
1500
1450
1400
1350
1300
Wavenumbers (cm-1)

Supplementary materials – Riker et al.

EPMA analytical conditions - apatite

Our standard analytical setup for electron probe microanalysis of apatite using the 5-spectrometer Cameca SX-100 electron microprobe at University of Bristol was (peak counting times given for each element; background counting times half as long):

Spectrometer 1 [LPET]:	Cl (120 s)			
Spectrometer 2 [PC1]:	F (120 s)			
Spectrometer 3 [LPET]:	Ca (30 s)	P (30 s)	K (30 s)	Ti (30 s)
Spectrometer 4 [TAP]:	Na (60 s)	Si (30 s)	Al (30 s)	Mg (60 s)
Spectrometer 5 [LLIF]:	Fe (60 s)	Mn (60 s)		

A 15 kV, 10 nA, 10 μm electron beam was used as a pragmatic compromise between the need for accurate analyses and the need to mitigate sample damage (e.g. Stormer et al. 1983; Goldoff et al. 2012; Stock et al. 2015). Na was calibrated on albite; Si and Mg on St John's Island olivine; Cl on NaCl; F on MgF_2; P and Ca on Durango apatite; K and Al on sanidine; Mn on Mn metal and Ti and Fe on ilmenite. Oriented secondary standards of Durango (Young et al. 1969) and Wilberforce apatite were analysed before, during and after every run.

EPMA analytical conditions - glass

Our standard analytical setup for electron probe microanalysis of hydrous glass using the 5-spectrometer Cameca SX-100 electron microprobe at University of Bristol was (peak counting times given for each element; background counting times half as long):

Spectrometer 1 [LPET]:	Cl (120 s)			
Spectrometer 2 [PC1, or PC0 for Fe-bearing glasses]:			F (120 s)	
Spectrometer 3 [LPET]:	Ca (30 s)	P (30 s)	K (30 s)	Ti (30 s)
Spectrometer 4 [TAP]:	Na (60 s)	Si (30 s)	Al (30 s)	Mg (30 s)
Spectrometer 5 [LLIF]:	Fe (60 s)	Mn (60 s)		

We used a 15 kV, 2 nA, 15 μm electron beam to mitigate sample damage (e.g. Devine et al. 1995; Humphreys et al. 2006). Na and Si were calibrated on albite; Mg on St John's Island olivine; Cl on NaCl; F on MgF_2; P on Durango apatite; Ca on wollastonite; K and Al on sanidine; Mn on Mn metal and Ti and Fe on ilmenite. Secondary standards KN18 (Nielsen & Sigurdsson 1981) and BCR were analysed before, during and after every analytical run, together with Durango apatite and three synthetic, fluorine-bearing basaltic glasses prepared using starting material SH3.

Reference materials used for analysis of volatiles

Reference	Sample	Phase	Used for
Shishkina et al. (2010)	M5, M10, M21, M36, M40, M47, N72	Basalt glass	Glass CO_2
Shishkina et al. (2010)	M5, M36, M40, N72	Basalt glass	Glass H_2O
Mangan & Sisson (2000)	#51	Rhyolite glass	Glass CO_2 and H_2O
Hauri et al. (2002)	519-4-1	Basalt glass	Glass CO_2 and H_2O
Brooker et al. (1999)	RB480	Basalt glass	Glass CO_2
Mandeville et al. (2002)	Run84	Andesite glass	Glass H_2O
Hunt & Hill (1993)	Lipari	Rhyolite glass	Glass H_2O, F and Cl
Vetere et al. (2014)	AH1, AH2_4, St3_AH2_3,	Alkali glass	Glass CO_2 and H_2O

	St3_AH1_2		
In-house standards	DUR, TNK, LIN, YAT, BAH2, IML5, SIB1, WIL2, JUM, PAN2, MAD2	Apatite	Apatite volatiles
Schettler et al. (2011)	APS-17, APS-26, APS25	Apatite	Apatite volatiles

Volatile-exchange K_Ds (mole fraction basis)

Experiment	$logK_D^{OH-F}$	$logK_D^{OH-Cl}$	$logK_D^{Cl-F}$	XOH_m	XF_m	XCl_m
BA6	-1.070			0.041	0.016	
BA9	-1.032			0.168	0.028	
BA10	-1.228			0.088	0.02	
BA11	-1.026			0.062	0.031	
BA12	-1.074	-0.766	-0.148	0.054	0.018	0.015
BA14	-1.183	-0.468	0.627	0.171	0.017	0.015
BM13	-1.546			0.081	0.017	
BM14	-1.584	-0.716	-0.391	0.078	0.017	0.025
BM16	-1.604	-0.684	-0.276	0.085	0.019	0.025

References

Brooker, R.A., Kohn, S.C., Holloway, J.R., McMillan, P.F., and Carroll, M.R. (1999). Solubility, speciation and dissolution mechanisms for CO_2 in melts on the $NaAlO_2$-SiO_2 join. Geochimica et Cosmochimica Acta, 63, 3549-3565

Devine, J.D., Gardner, J.E., Brack, H.P., Layne, G.D., and Rutherford, M.J. (1995) Comparison of microanalytical methods for estimating H_2O contents of silicic volcanic glasses. American Mineralogist, 80, 319-328

Goldoff, B., Webster, J.D., and Harlov, D.E. (2012) Characterization of fluor-chlorapatites by electron probe microanalysis with a focus on time-dependent intensity variation of halogens. American Mineralogist, 97, 1103-1115

Hauri, E., Wang, J., Dixon, J.E., King, P.L., Mandeville, C., and Newman, S. (2002) SIMS analysis of volatile in silicate glasses 1. Calibration, matrix effects and comparisons with FTIR. Chemical Geology, 183, 99-114

Humphreys, M.C.S., Kearns, S.L., and Blundy, J.D. (2006) SIMS investigation of electron-beam damage to hydrous, rhyolitic glasses: Implications for melt inclusion analysis. American Mineralogist, 91, 667-679

Hunt, J.B., and Hill, P.G. (1993) Tephra geochemistry: a discussion of some persistent analytical problems. The Holocene, 3, 271-278

Mandeville, C.W., Webster, J.D., Rutherford, M.J., Taylor, B.E., Timbal, A., and Faure, K. (2002) Determination of molar absorptivities for infrared absorption bands of H_2O in andesitic glasses. American Mineralogist, 87, 813-821

Mangan, M., and Sisson, T. (2000) Delayed, disequilibrium degassing in rhyolite magma: decompression experiments and implications for explosive volcanism. Earth and Planetary Science Letters, 183, 441-455

Nielsen, C.H., and Sigurdsson, H. (1981) Quantitative methods for electron microprobe analysis of sodium in natural and synthetic glasses. American Mineralogist, 66, 547-552

Schettler, G., Gottschalk, M., and Harlov, D.E. (2011) A new semi-micro wet chemical method for apatite analysis and its application to the crystal chemistry of fluorapatite-chlorapatite solid solutions. American Mineralogist, 96, 138-152

Stock, M.J., Humphreys, M.C.S., Smith, V.C., Johnson, R.D., Pyle, D.M., and EIMF (2015) New constraints on electron-beam induced halogen migration in apatite. American Mineralogist, 100, 281-293

Stormer, J.C., Pierson, M.L., and Tacker, R.C. (1993) Variation of F and Cl X-ray intensity due to anisotropic diffusion in apatite during electron microprobe analysis. American Mineralogist, 78, 641-648

Vetere, F., Holtz, F., Behrens, H., Botcharnikov, R.E., and Fanara, S (2014) The effect of alkalis and polymerization on the solubility of H_2O and CO_2 in alkali-rich silicate melts. Contributions to Mineralogy and Petrology, 167, 1014

Young, E.J., Myers, A.T., Munson, E.L., and Conklin, N.M. (1969) Mineralogy and geochemistry of fluorapatite from the Cerro de Mercado, Durango, Mexico. USGS Professional Paper 650D, 84-93

Results of multiple regression analysis for literature dataset of KD for OH-halogen exchange

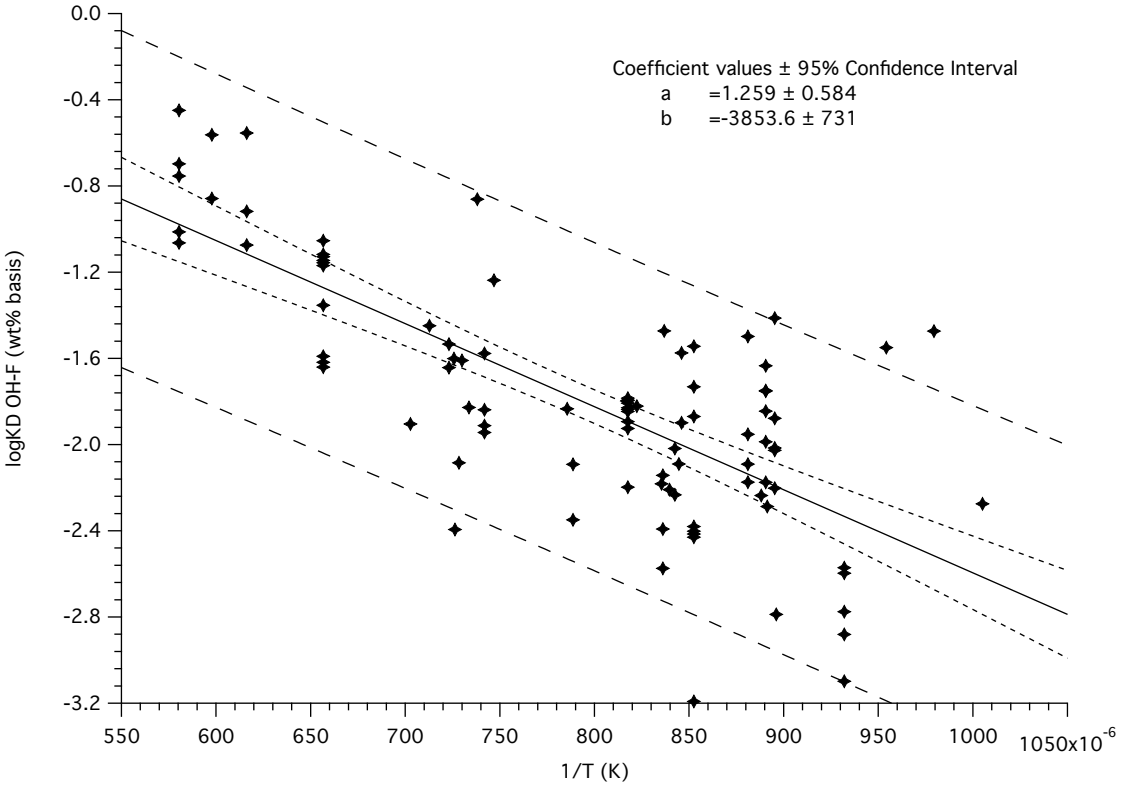

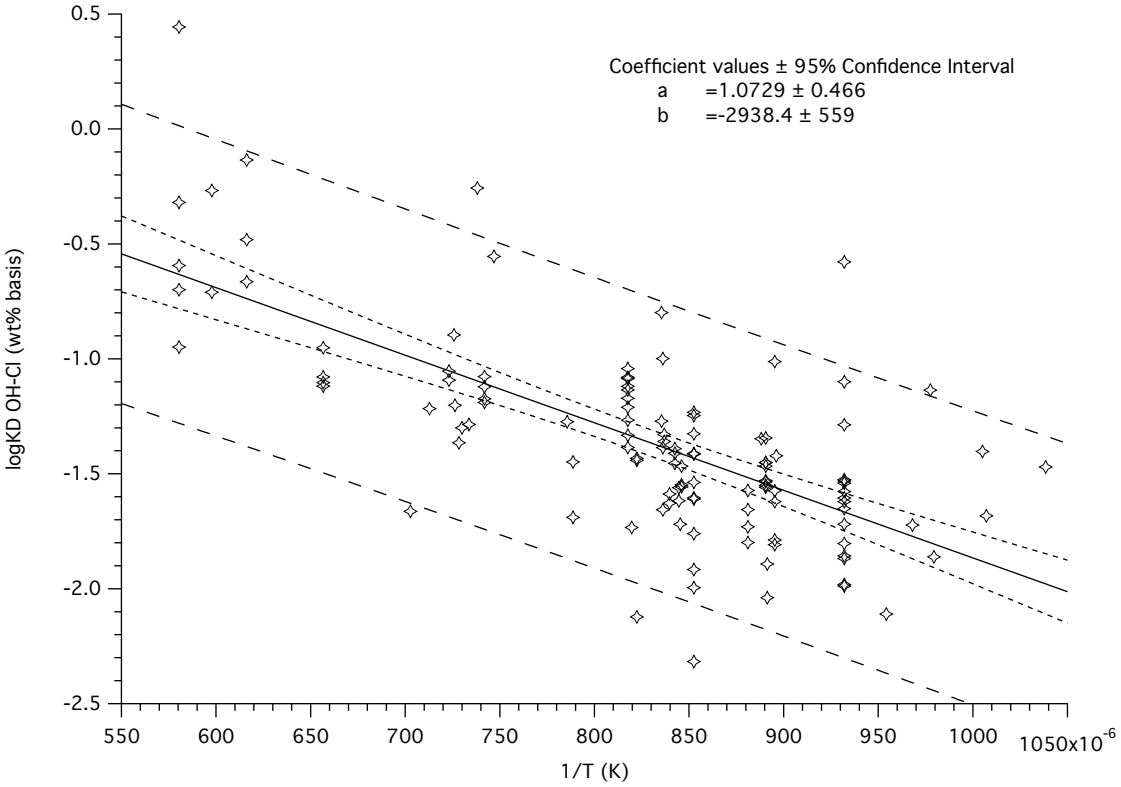

Secondary ion mass spectrometry calibration lines for analytical session 1

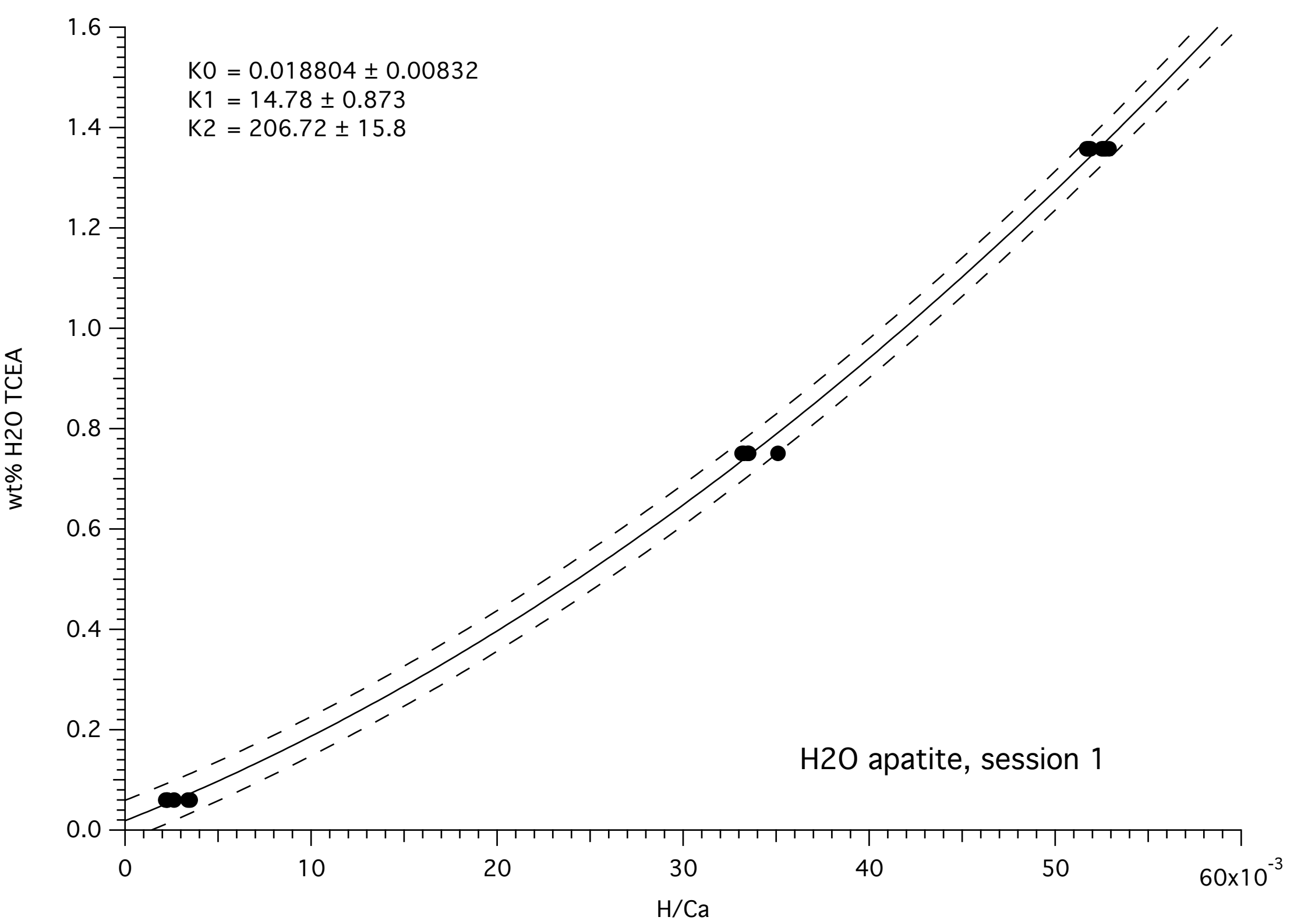
K0 = 0.018804 ± 0.00832
K1 = 14.78 ± 0.873
K2 = 206.72 ± 15.8
wt% H2O TCEA
H/Ca
60x10-3
H2O apatite, session 1
0.0
0.2
0.4
0.6
0.8
1.0
1.2
1.4
1.6
0
10
20
30
40
50

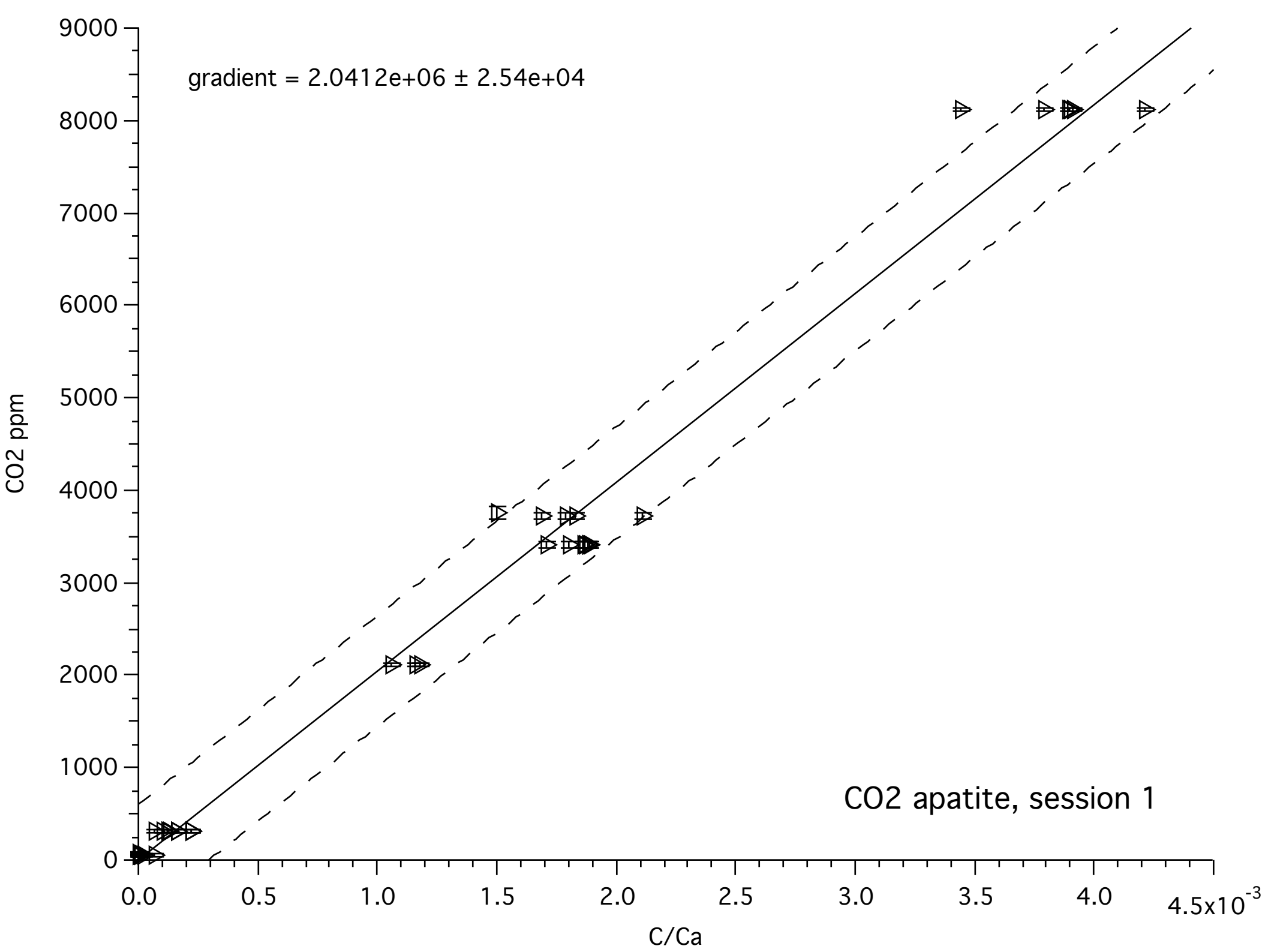
gradient = 2.0412e+06 ± 2.54e+04
CO2 apatite, session 1
CO2 ppm
C/Ca
9000
8000
7000
6000
5000
4000
3000
2000
1000
0
0.0
0.5
1.0
1.5
2.0
2.5
3.0
3.5
4.0
4.5x10-3

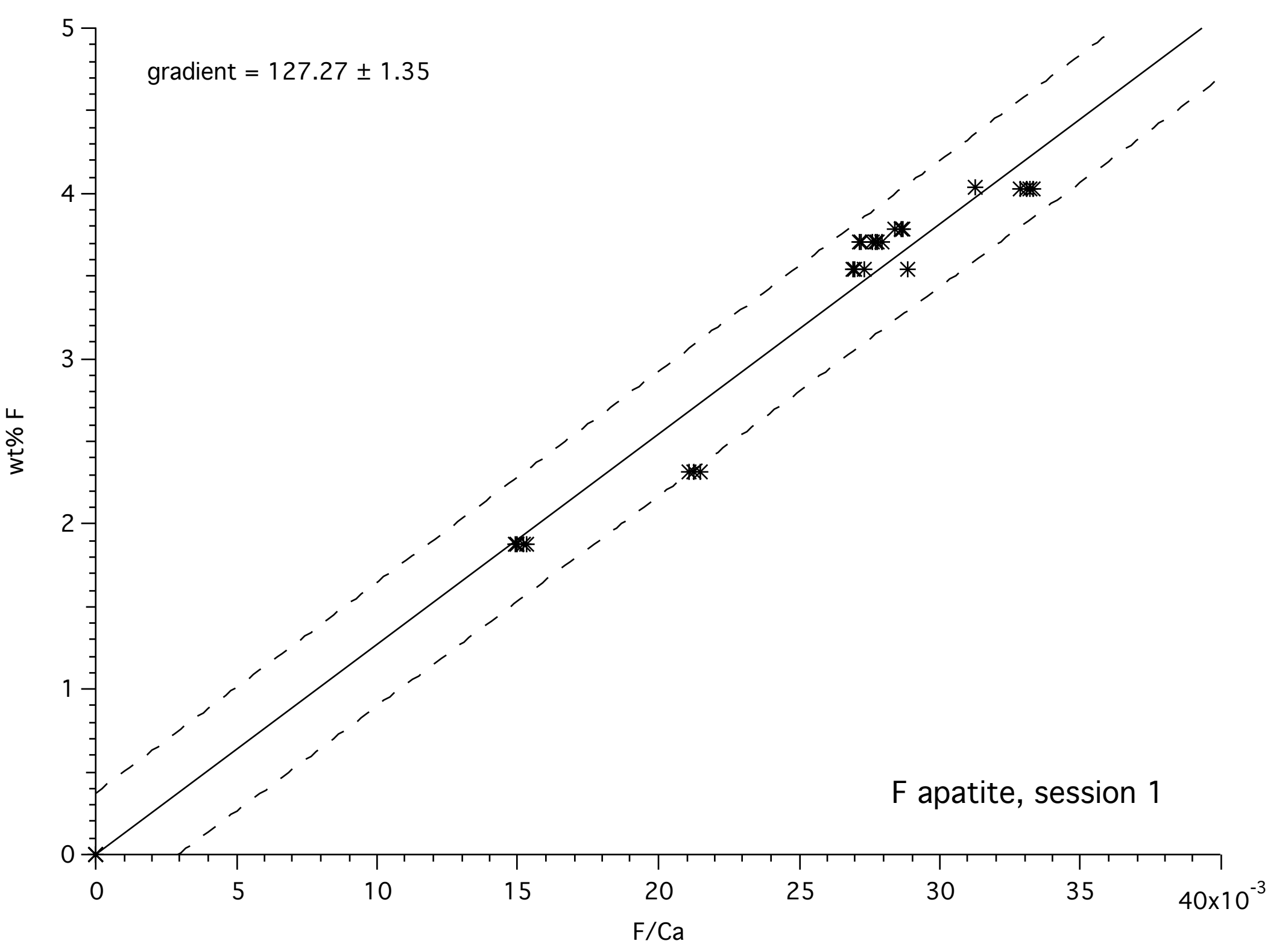
gradient = 127.27 ± 1.35
F apatite, session 1
wt% F
F/Ca
0
1
2
3
4
5
0
5
10
15
20
25
30
35
40x10-3

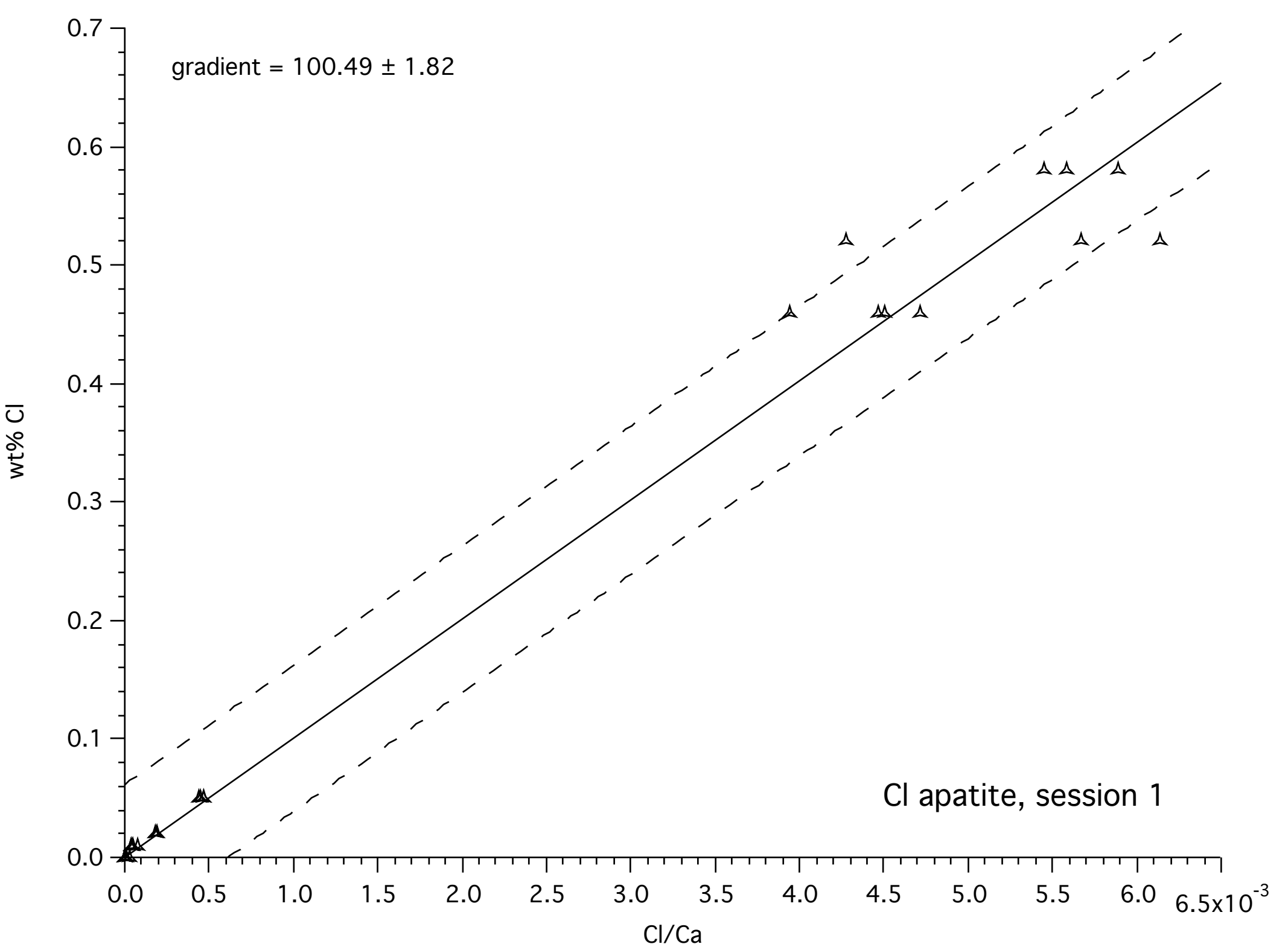
gradient = 100.49 ± 1.82
wt% Cl
Cl/Ca
Cl apatite, session 1
0.0
0.1
0.2
0.3
0.4
0.5
0.6
0.7
0.0
0.5
1.0
1.5
2.0
2.5
3.0
3.5
4.0
4.5
5.0
5.5
6.0
6.5x10-3

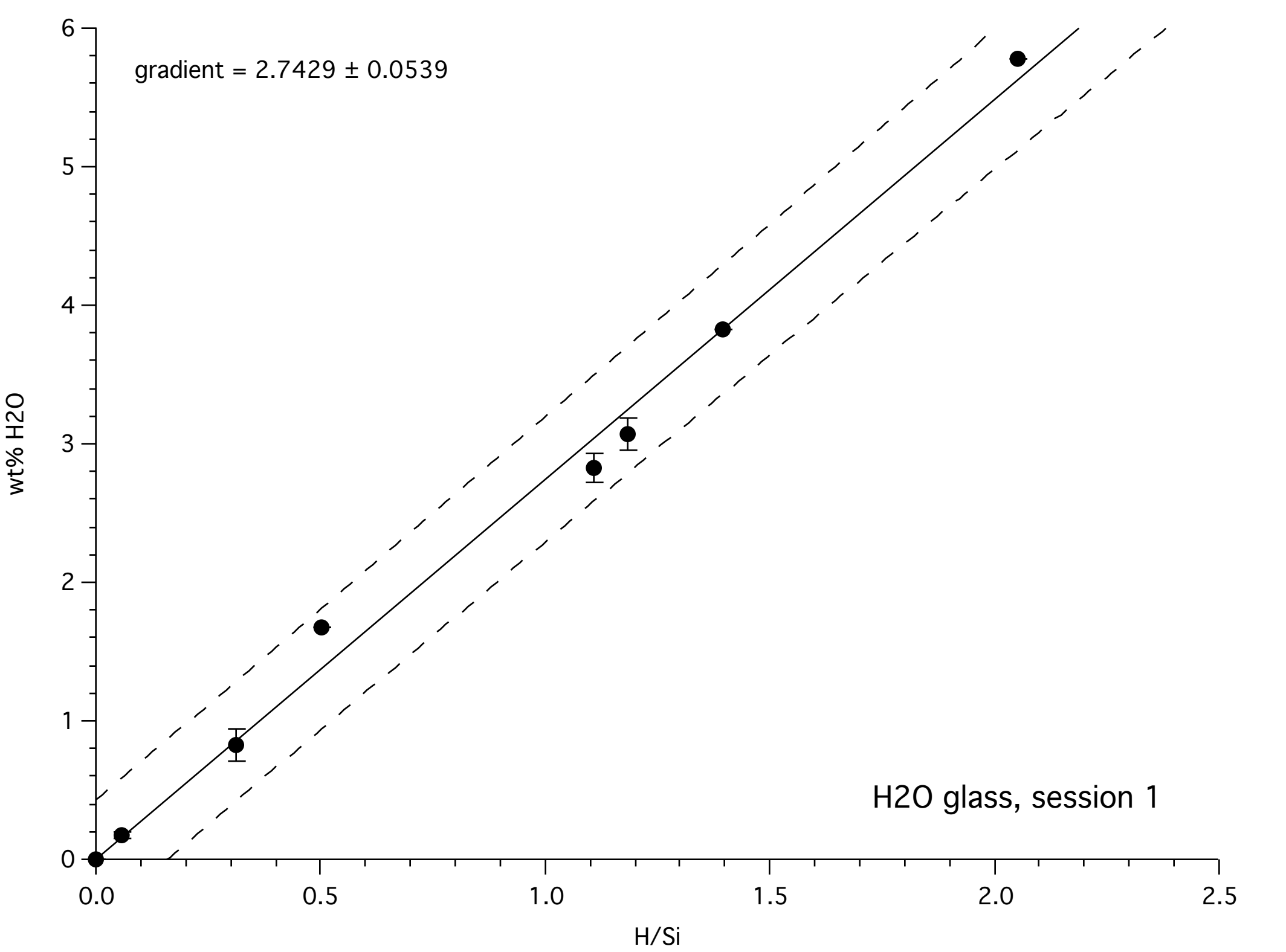
gradient = 2.7429 ± 0.0539
H2O glass, session 1
wt% H2O
H/Si
0
1
2
3
4
5
6
0.0
0.5
1.0
1.5
2.0
2.5

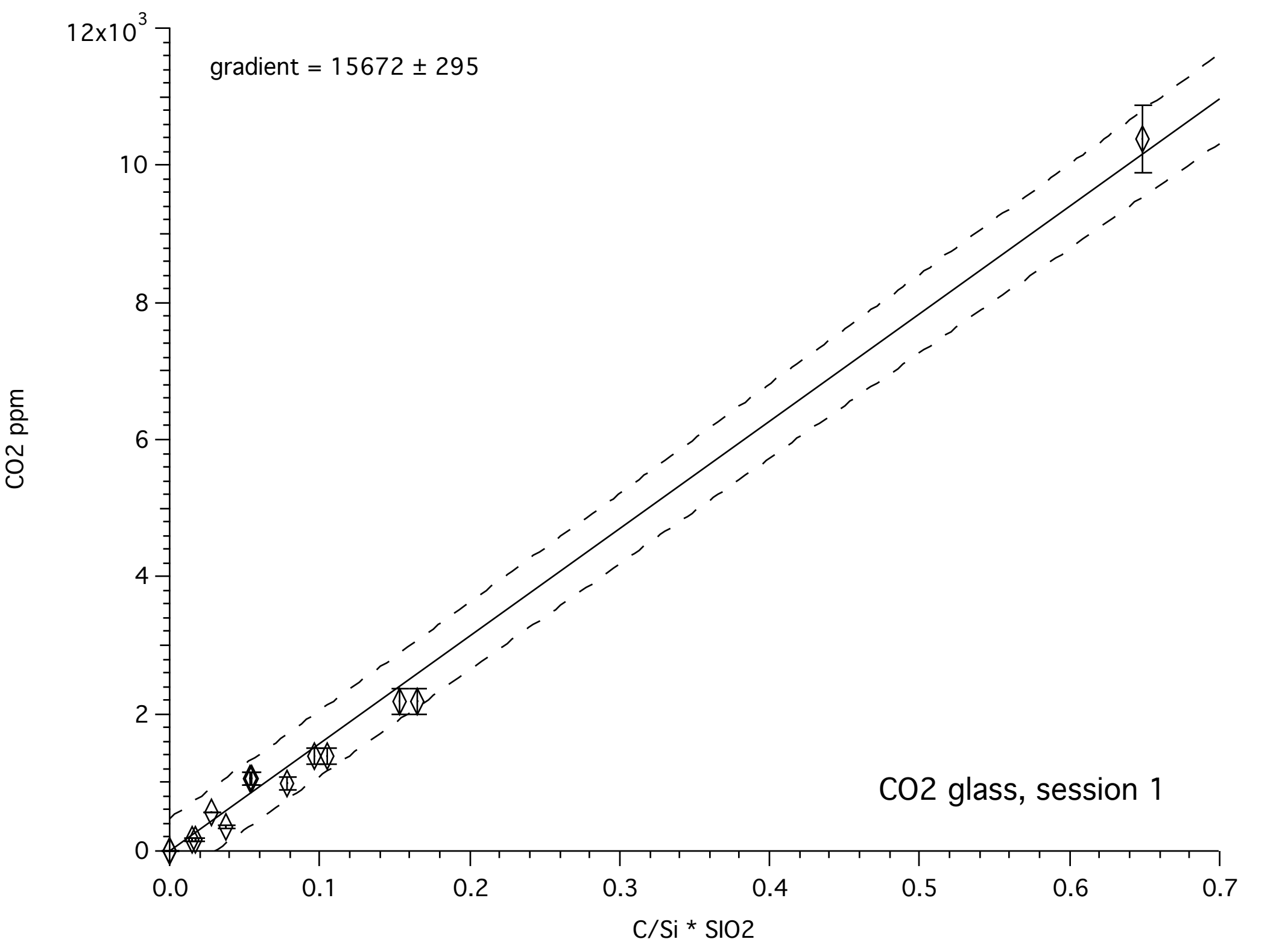
12x10^3
gradient = 15672 ± 295
10
8
6
4
2
0
CO2 ppm
0.0
0.1
0.2
0.3
0.4
0.5
0.6
0.7
C/Si * SIO2
CO2 glass, session 1

Secondary ion mass spectrometry calibration lines for analytical session 2

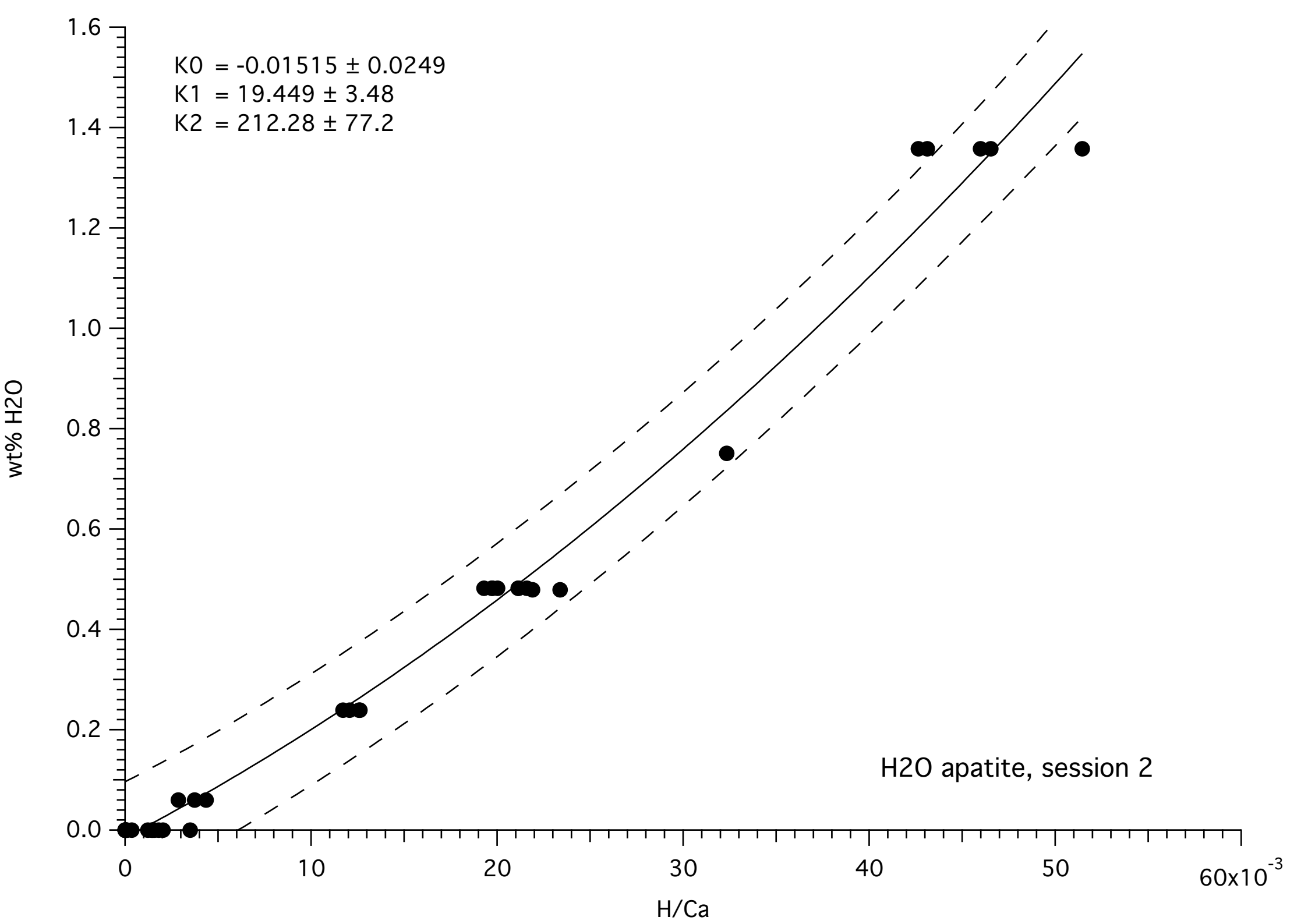
K0 = -0.01515 ± 0.0249
K1 = 19.449 ± 3.48
K2 = 212.28 ± 77.2
H2O apatite, session 2
wt% H2O
H/Ca
60x10-3
0.0
0.2
0.4
0.6
0.8
1.0
1.2
1.4
1.6
0
10
20
30
40
50

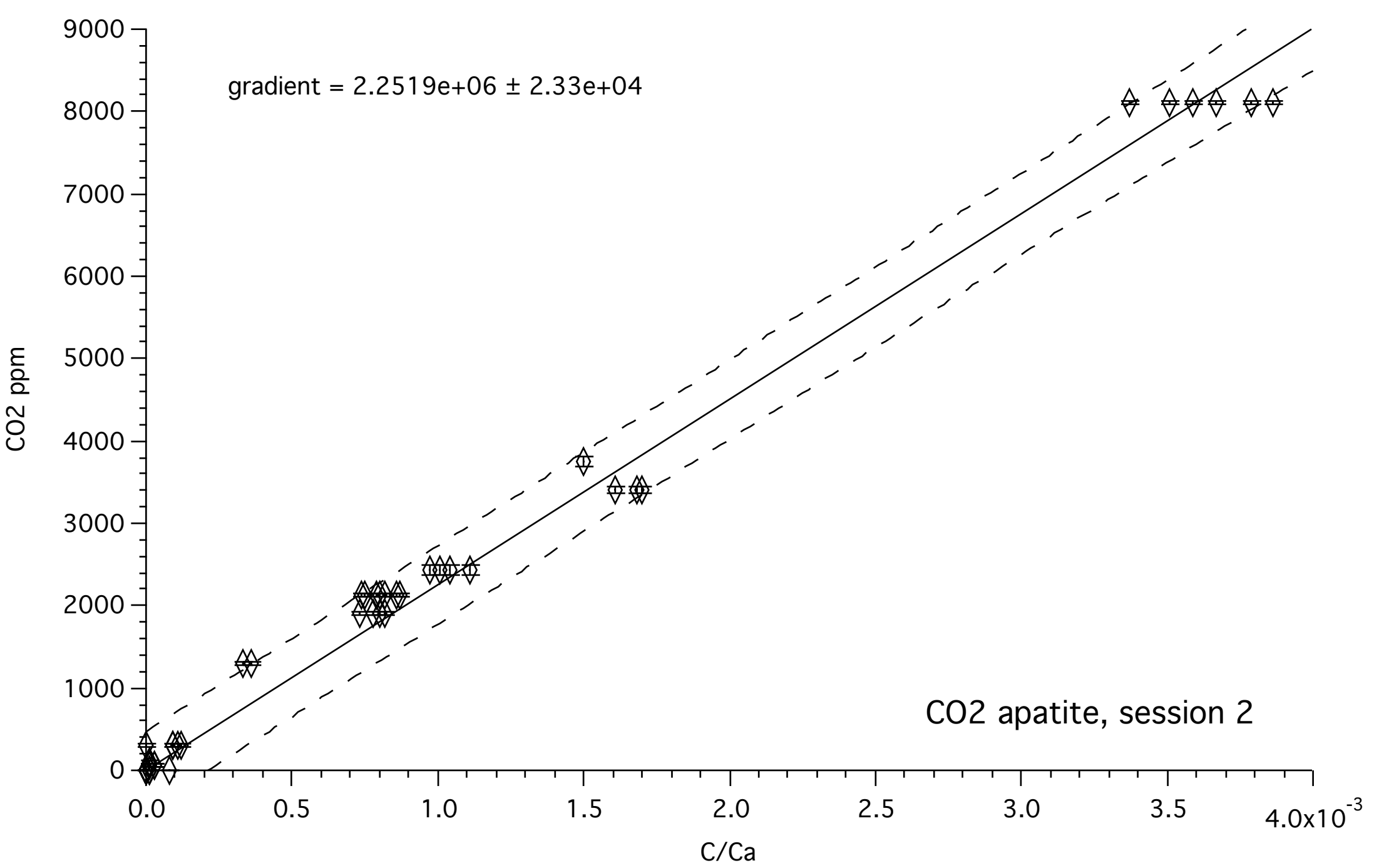
gradient = 2.2519e+06 ± 2.33e+04
CO2 apatite, session 2
CO2 ppm
C/Ca
9000
8000
7000
6000
5000
4000
3000
2000
1000
0
0.0
0.5
1.0
1.5
2.0
2.5
3.0
3.5
4.0x10-3

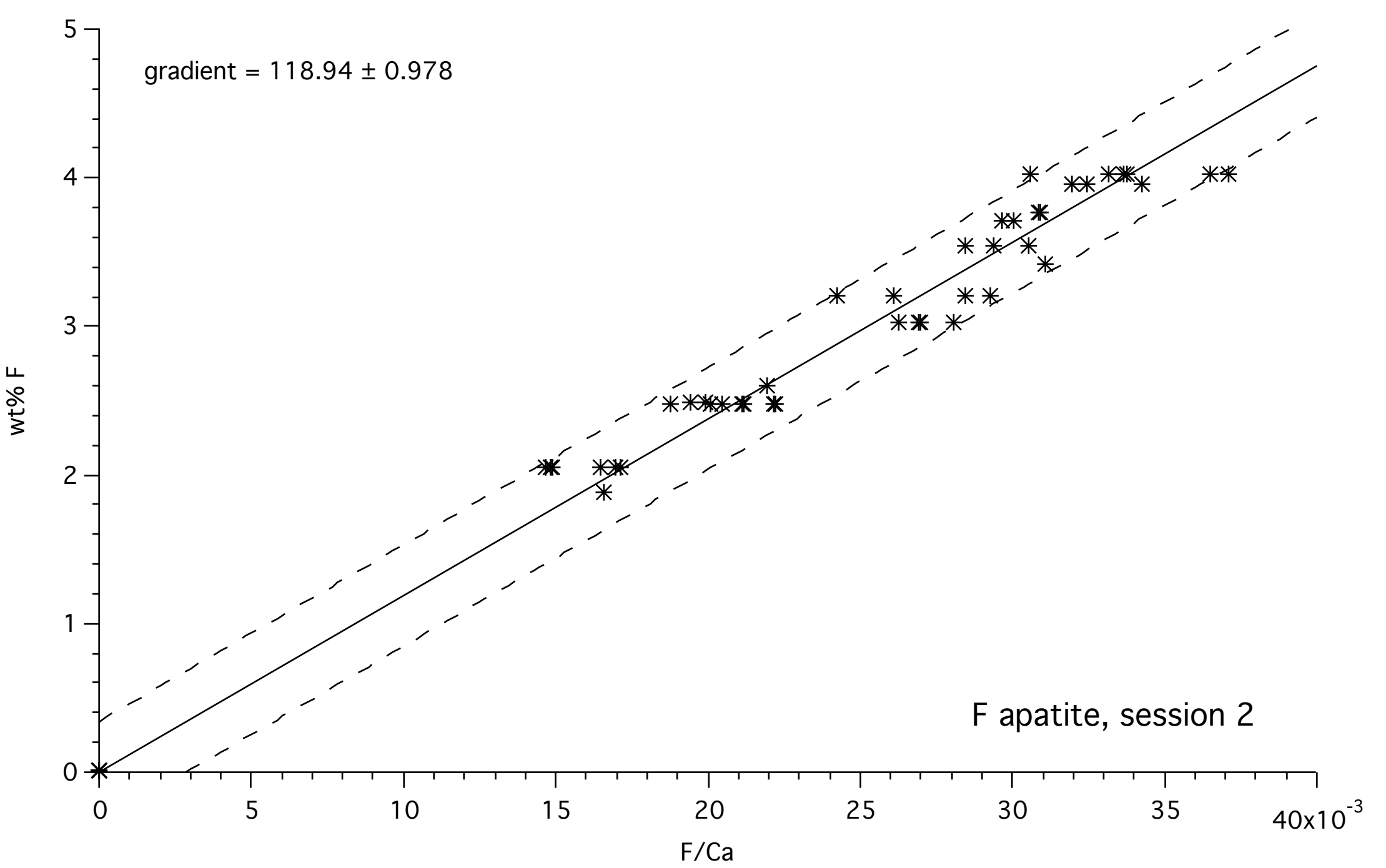
gradient = 118.94 ± 0.978
wt% F
F/Ca
F apatite, session 2
0
1
2
3
4
5
0
5
10
15
20
25
30
35
40x10-3

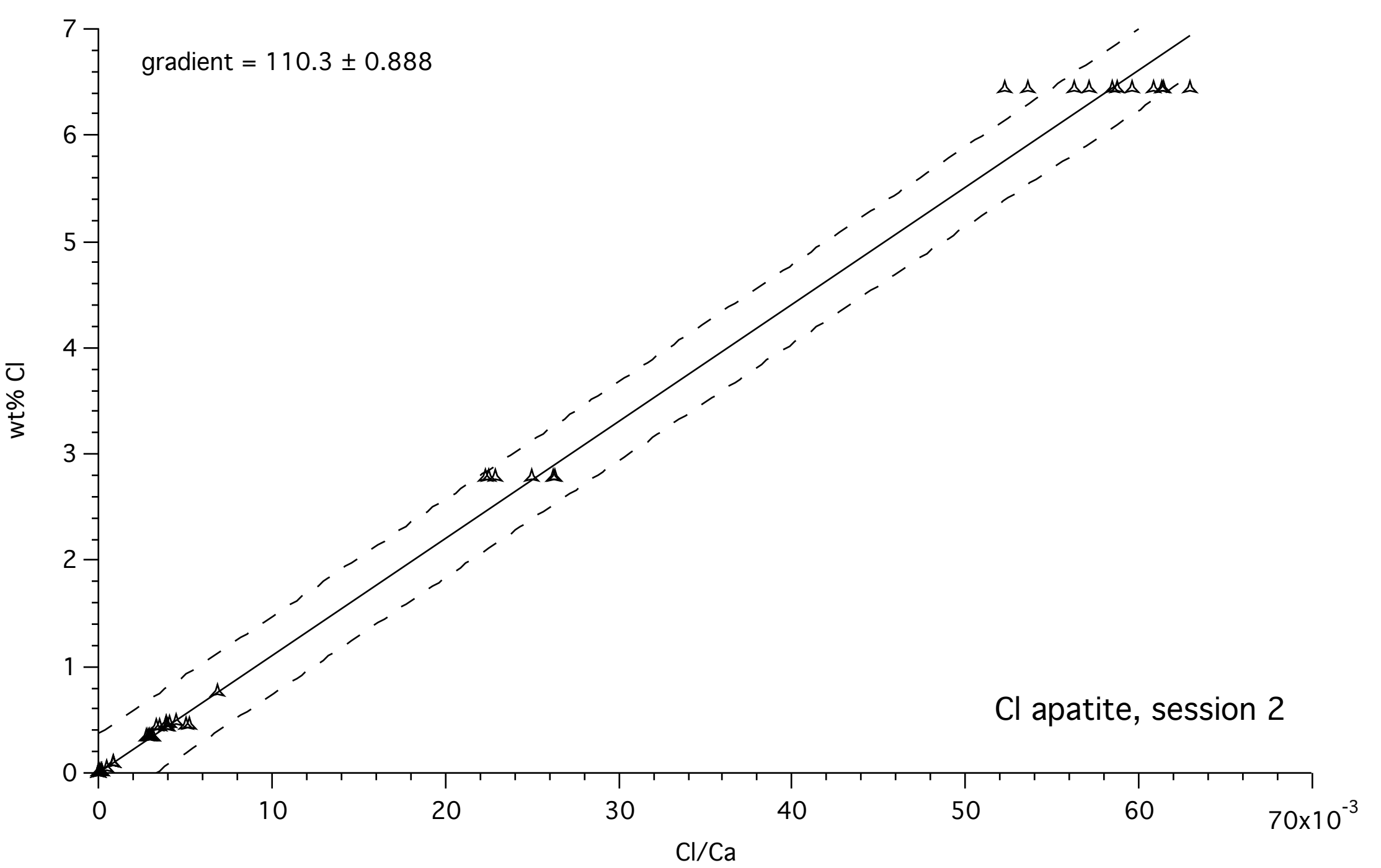
gradient = 110.3 ± 0.888
wt% Cl
Cl/Ca
Cl apatite, session 2
0
1
2
3
4
5
6
7
0
10
20
30
40
50
60
70x10-3

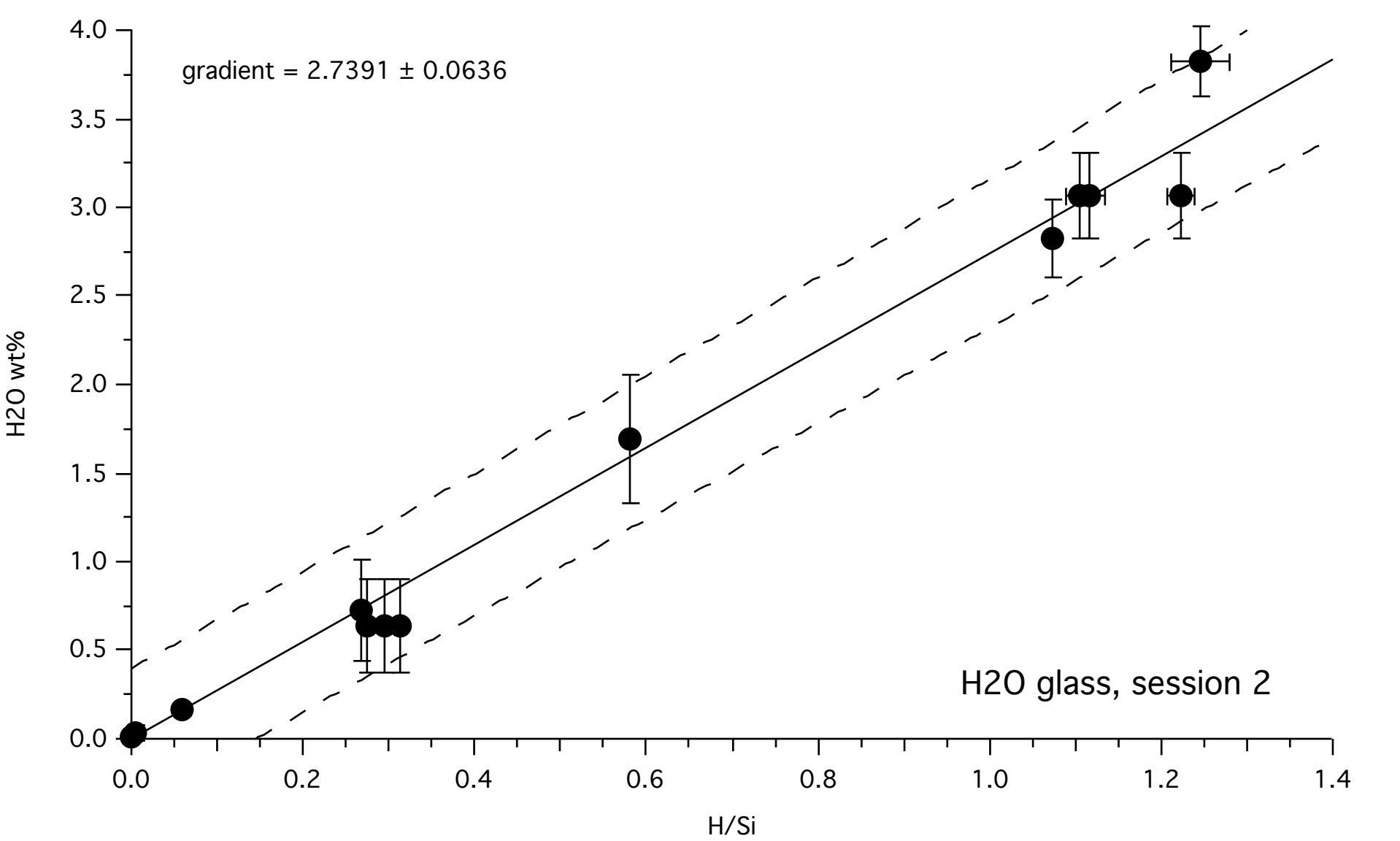
gradient = 2.7391 ± 0.0636
H2O glass, session 2
H2O wt%
H/Si
0.0
0.5
1.0
1.5
2.0
2.5
3.0
3.5
4.0
0.0
0.2
0.4
0.6
0.8
1.0
1.2
1.4

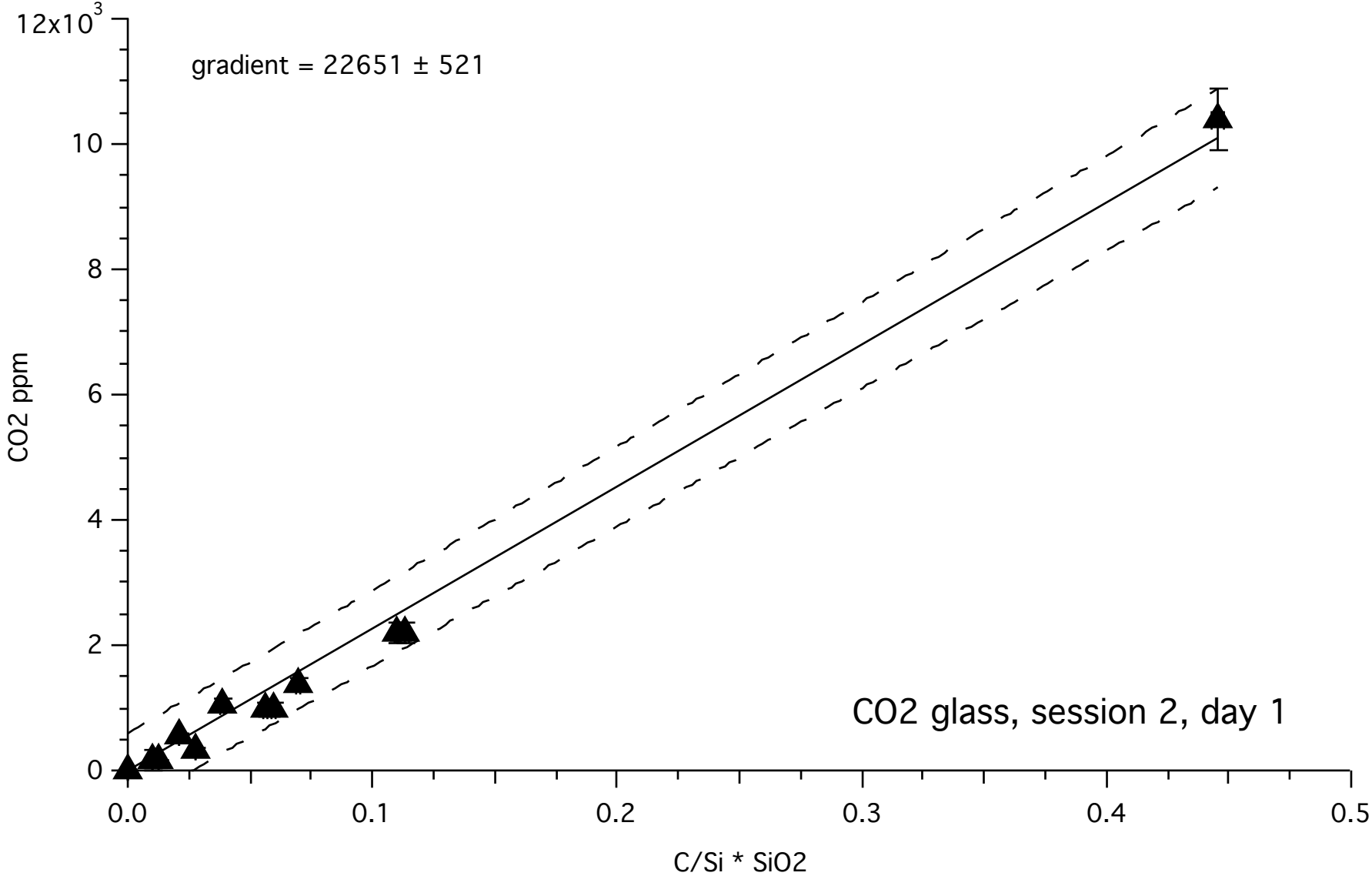
12x10^3
gradient = 22651 ± 521
10
8
6
4
2
0
CO2 ppm
0.0
0.1
0.2
0.3
0.4
0.5
C/Si * SiO2
CO2 glass, session 2, day 1

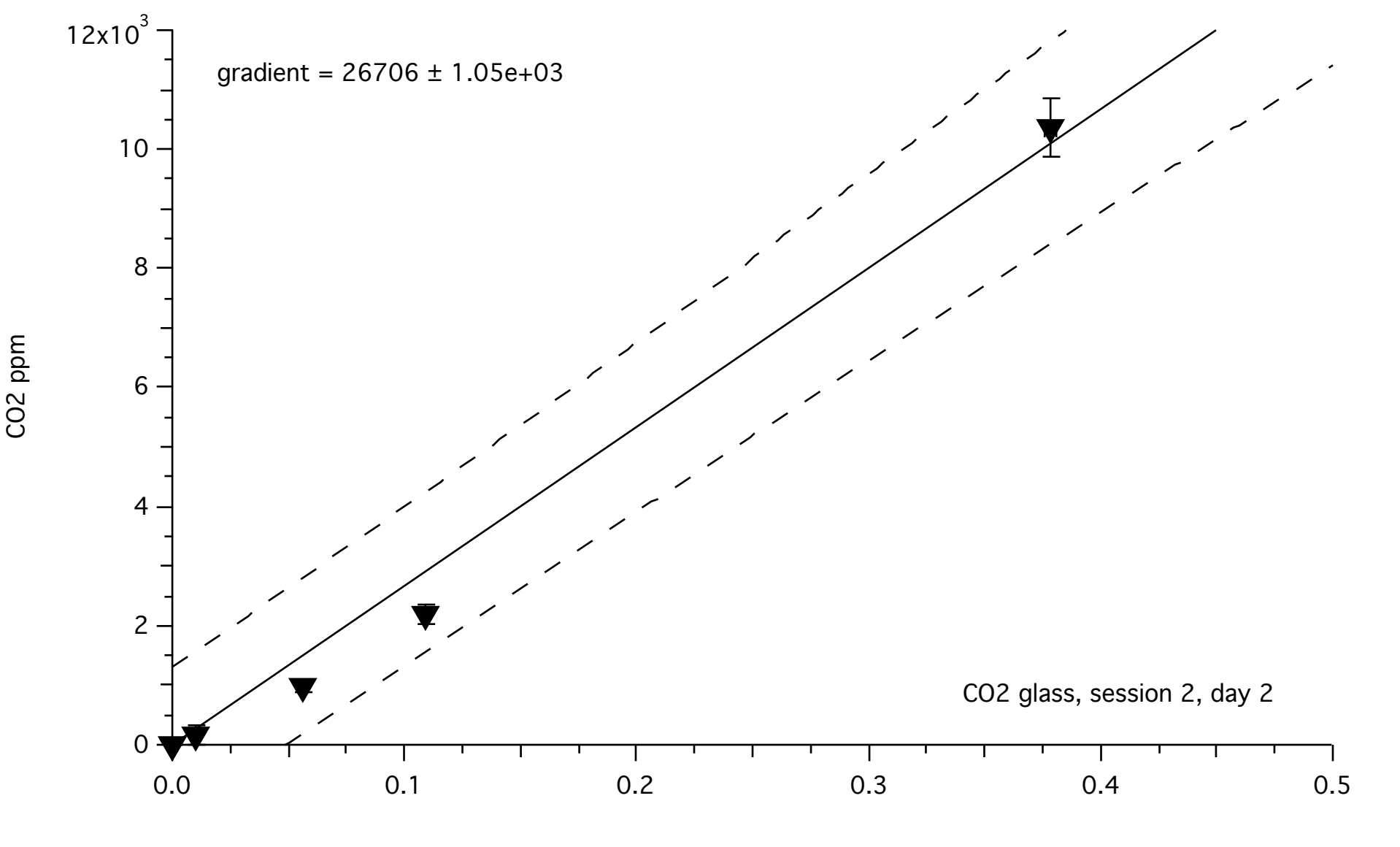
12x10^3
gradient = 26706 ± 1.05e+03
10
8
6
4
2
0
CO2 ppm
CO2 glass, session 2, day 2
0.0
0.1
0.2
0.3
0.4
0.5

Secondary ion mass spectrometry calibration lines for analytical session 3

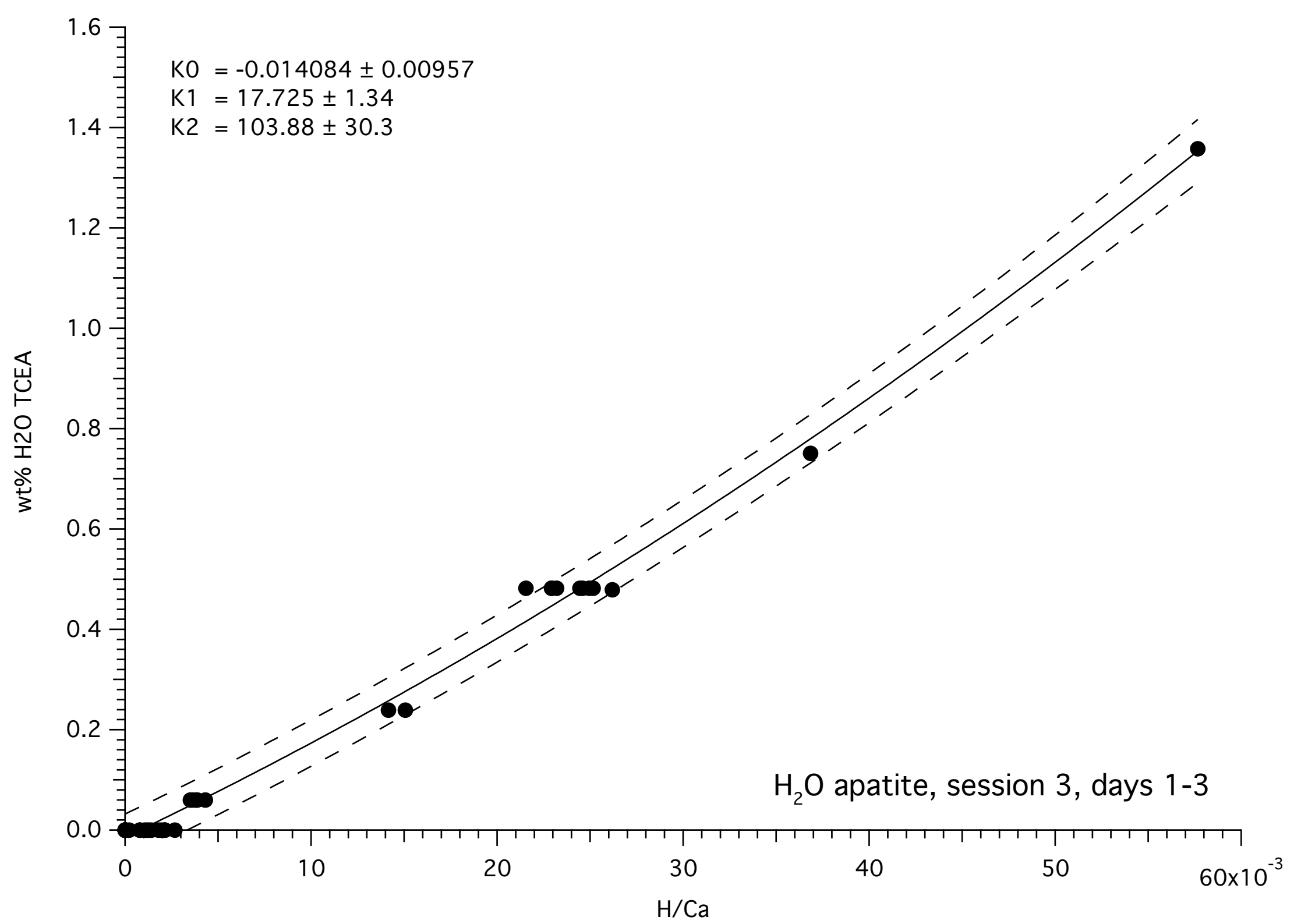
K0 = -0.014084 ± 0.00957
K1 = 17.725 ± 1.34
K2 = 103.88 ± 30.3
wt% H2O TCEA
H/Ca
60x10-3
H2O apatite, session 3, days 1-3
0.0
0.2
0.4
0.6
0.8
1.0
1.2
1.4
1.6
0
10
20
30
40
50

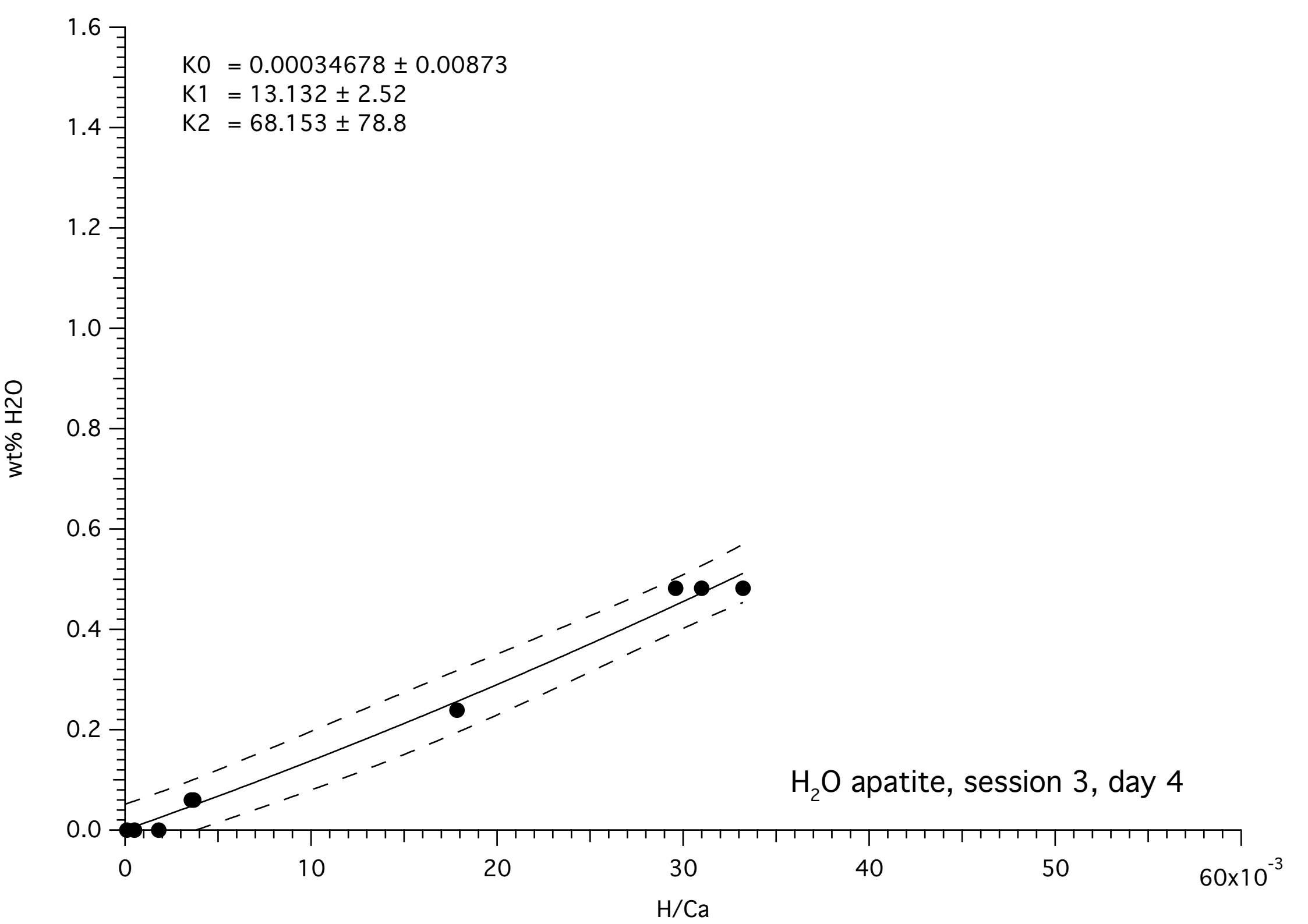
K0 = 0.00034678 ± 0.00873
K1 = 13.132 ± 2.52
K2 = 68.153 ± 78.8
wt% H2O
H/Ca
60x10-3
H2O apatite, session 3, day 4

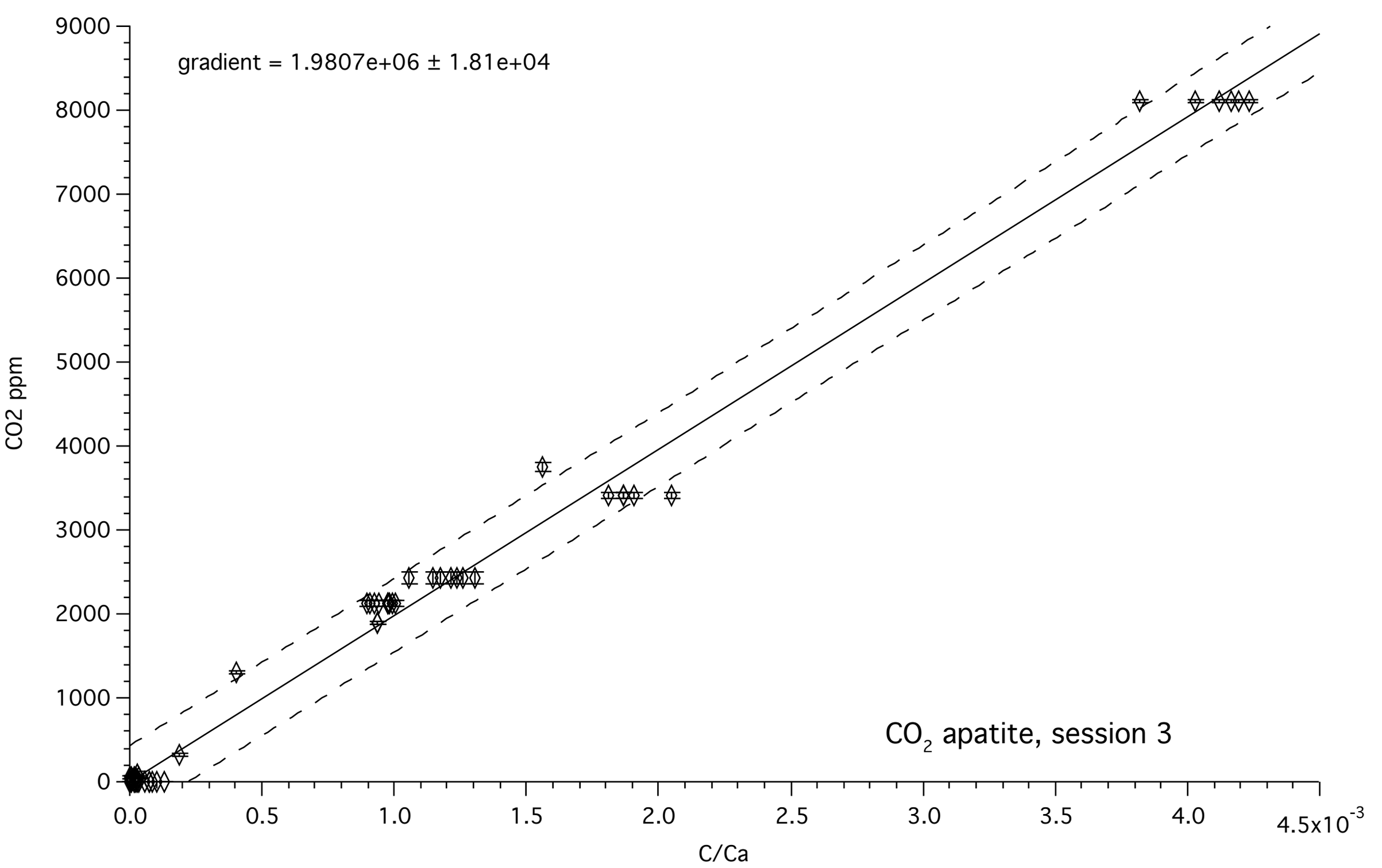
gradient = 1.9807e+06 ± 1.81e+04
CO2 ppm
C/Ca
4.5x10-3
CO2 apatite, session 3
9000
8000
7000
6000
5000
4000
3000
2000
1000
0
0.0
0.5
1.0
1.5
2.0
2.5
3.0
3.5
4.0

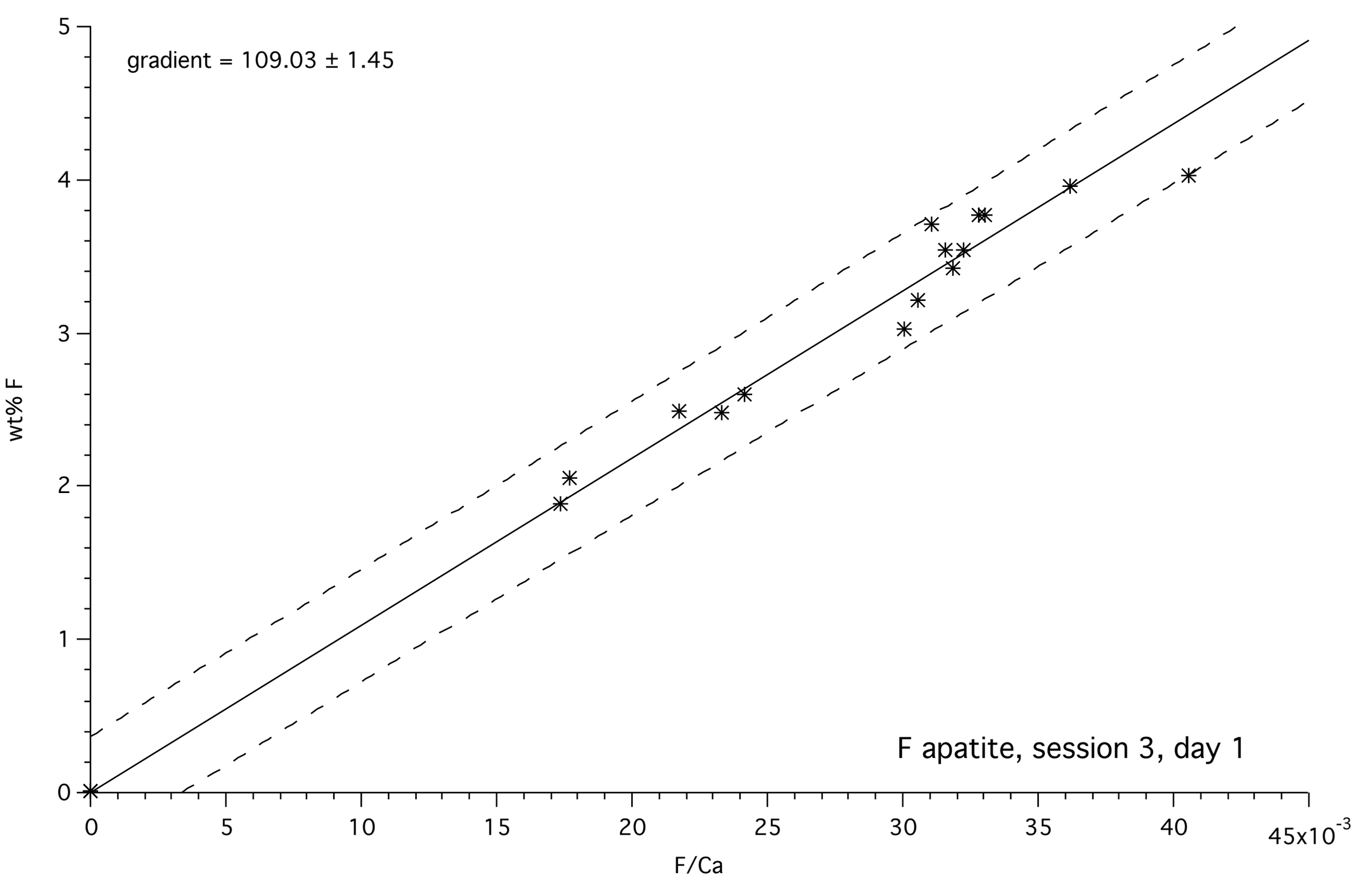
gradient = 109.03 ± 1.45
wt% F
F/Ca
45x10-3
F apatite, session 3, day 1
0
1
2
3
4
5
0
5
10
15
20
25
30
35
40

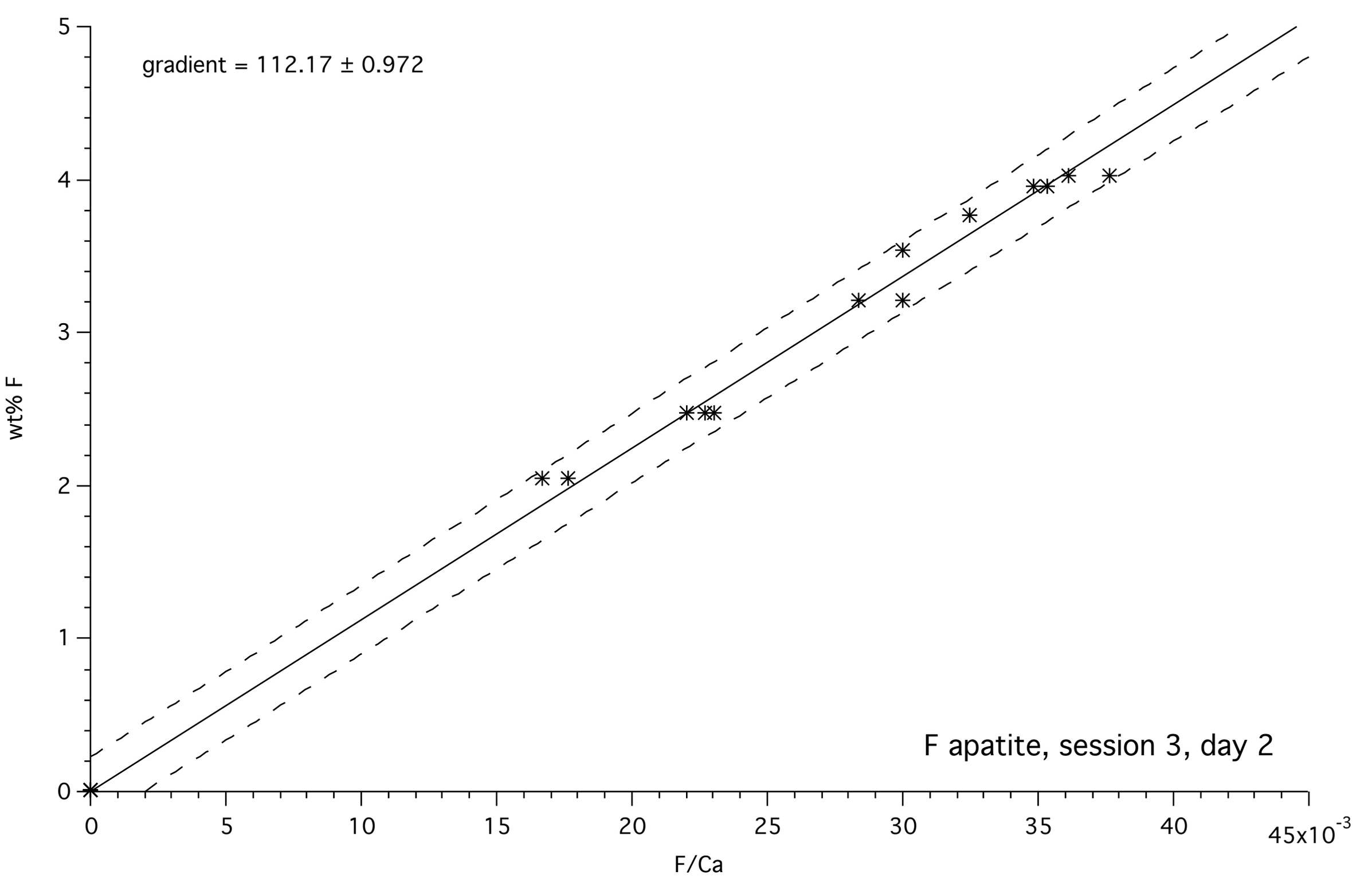
gradient = 112.17 ± 0.972
wt% F
F/Ca
45x10-3
F apatite, session 3, day 2
0
1
2
3
4
5
0
5
10
15
20
25
30
35
40

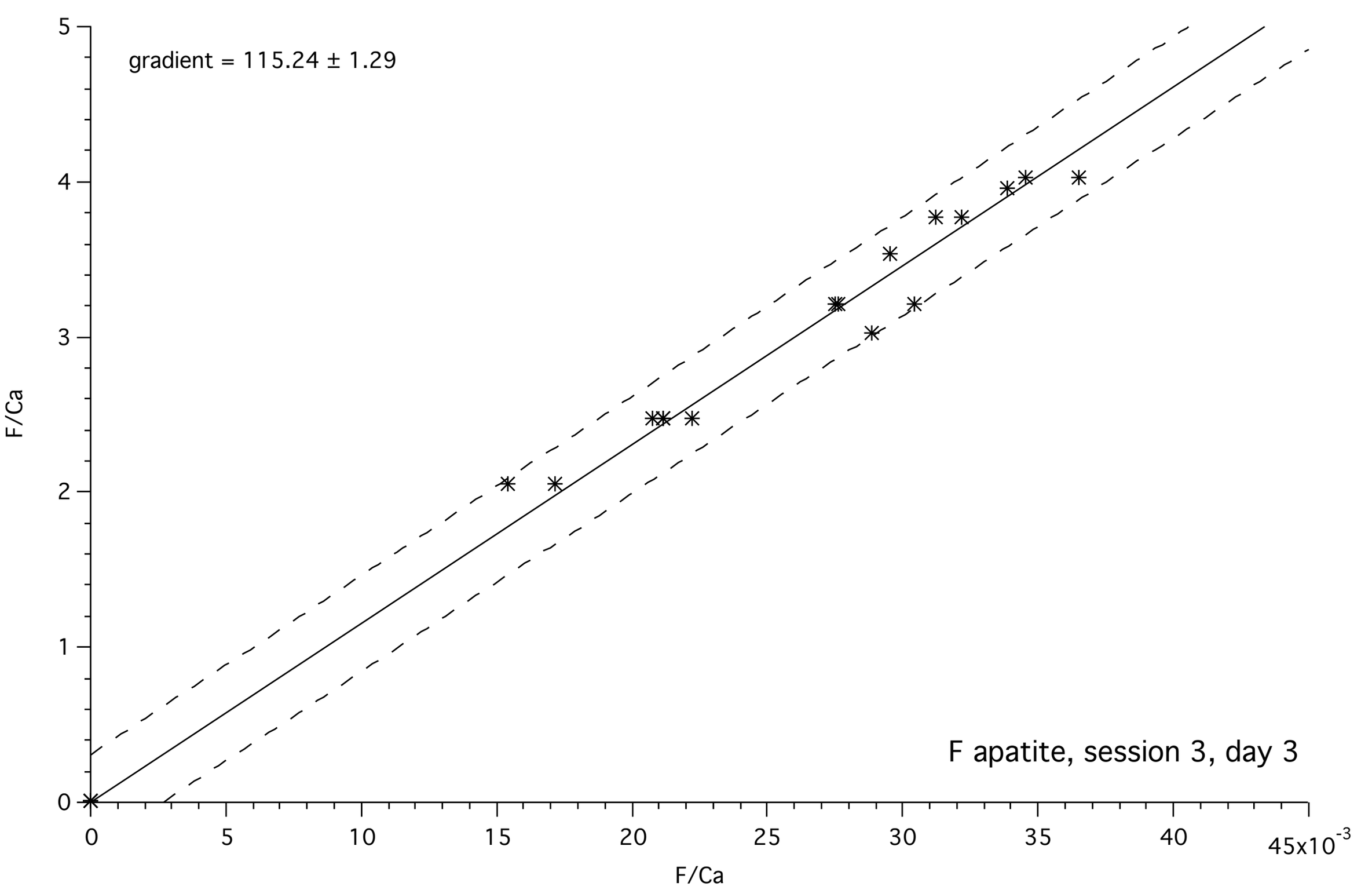
gradient = 115.24 ± 1.29
F apatite, session 3, day 3
F/Ca
F/Ca
0
1
2
3
4
5
0
5
10
15
20
25
30
35
40
45x10-3

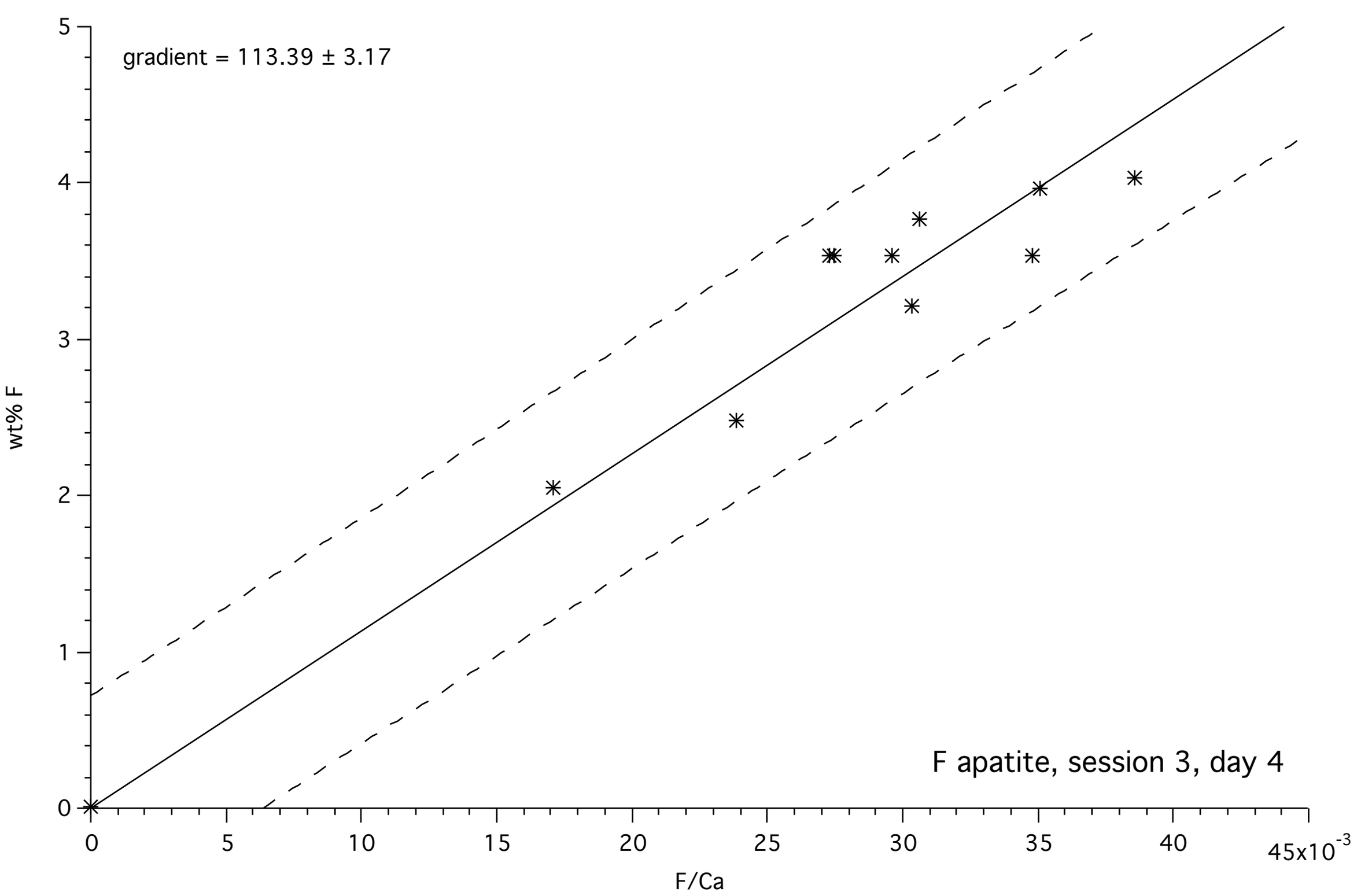
gradient = 113.39 ± 3.17
wt% F
F/Ca
45x10^-3
F apatite, session 3, day 4
0
1
2
3
4
5
0
5
10
15
20
25
30
35
40

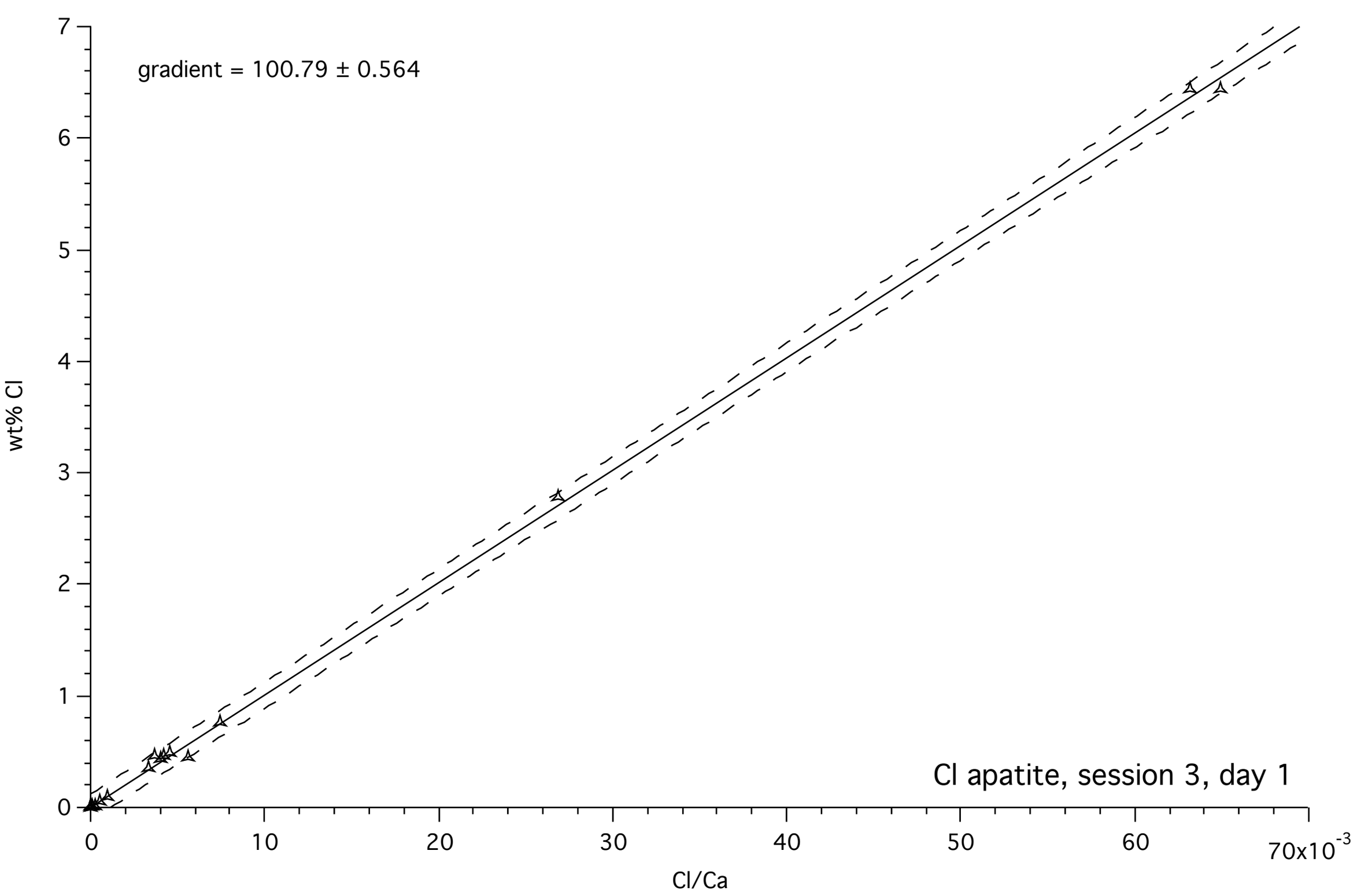
gradient = 100.79 ± 0.564
wt% Cl
Cl/Ca
70x10-3
Cl apatite, session 3, day 1
0
1
2
3
4
5
6
7
0
10
20
30
40
50
60

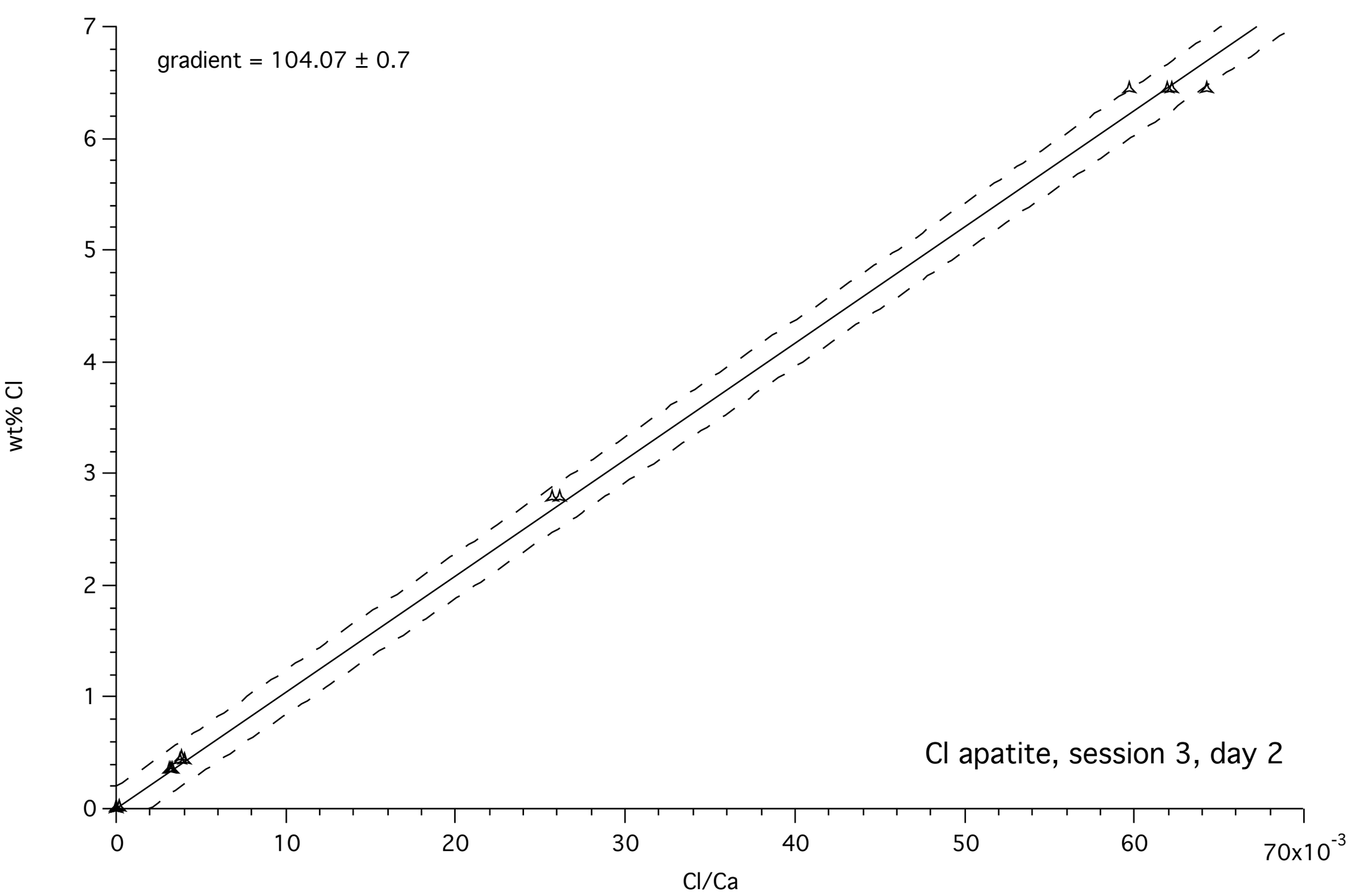
gradient = 104.07 ± 0.7
wt% Cl
Cl/Ca
0
1
2
3
4
5
6
7
0
10
20
30
40
50
60
70x10-3
Cl apatite, session 3, day 2

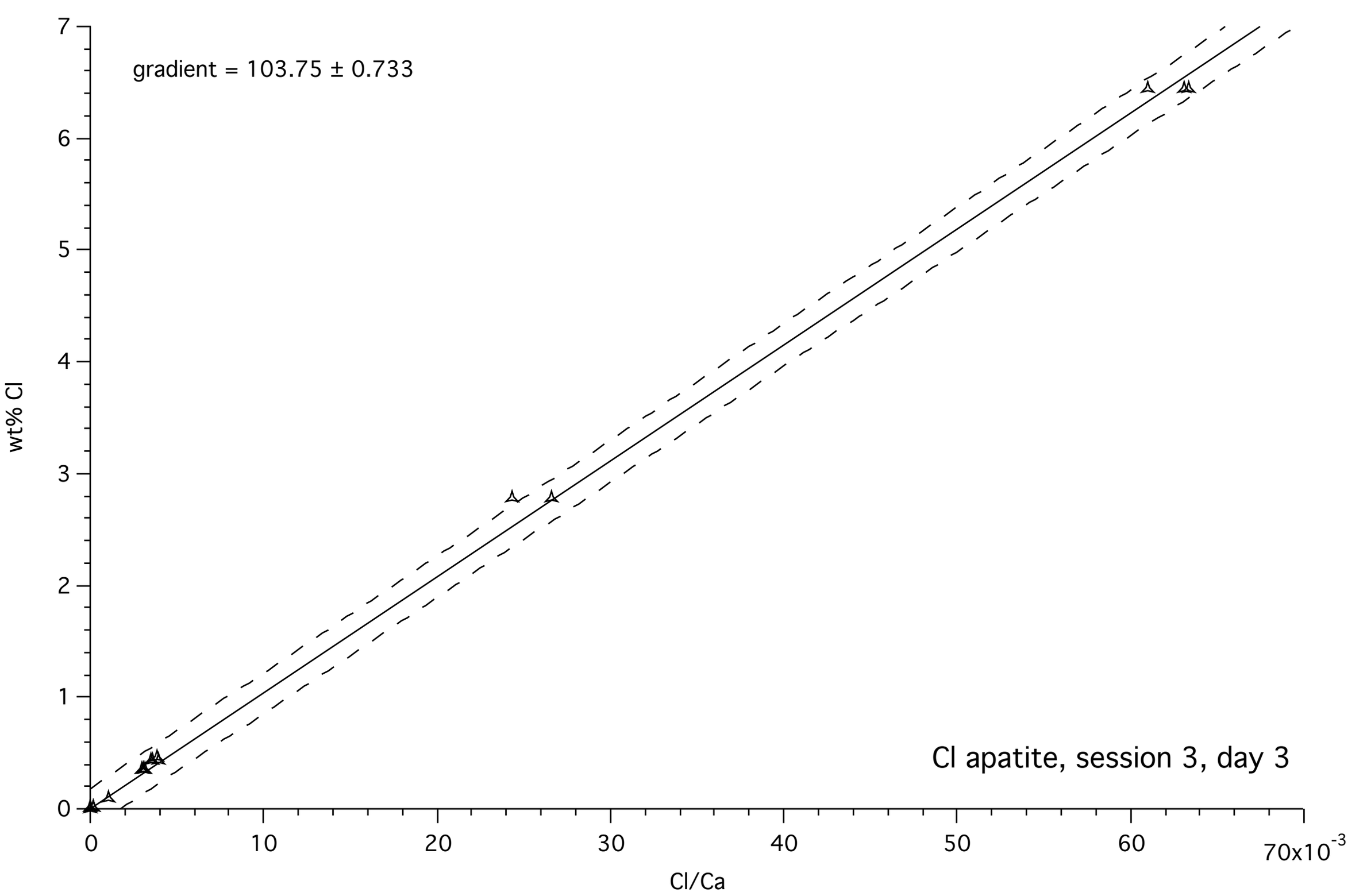
gradient = 103.75 ± 0.733
wt% Cl
Cl/Ca
70x10-3
Cl apatite, session 3, day 3
0
1
2
3
4
5
6
7
0
10
20
30
40
50
60

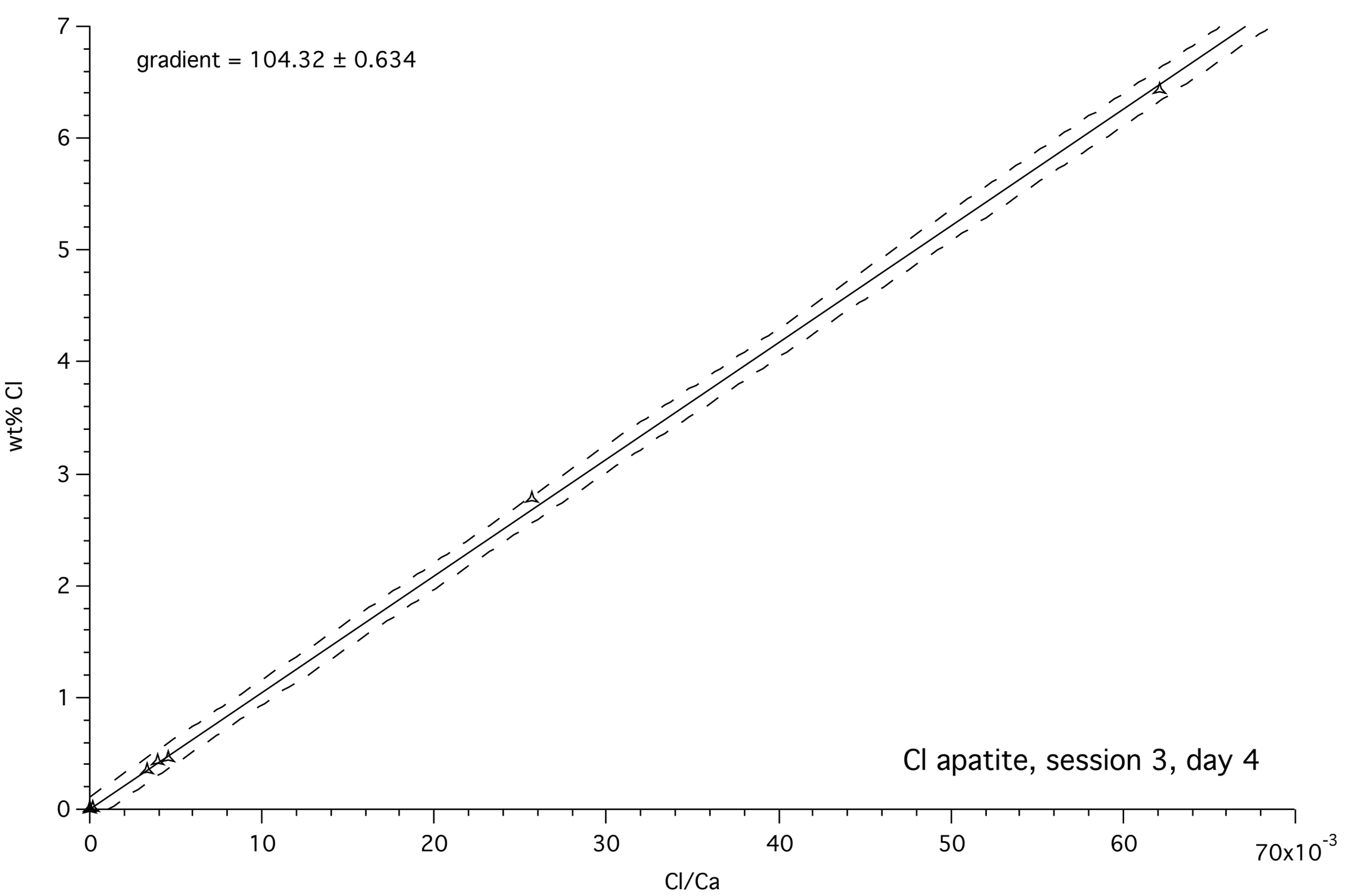
gradient = 104.32 ± 0.634
wt% Cl
Cl/Ca
0
1
2
3
4
5
6
7
0
10
20
30
40
50
60
70x10-3
Cl apatite, session 3, day 4

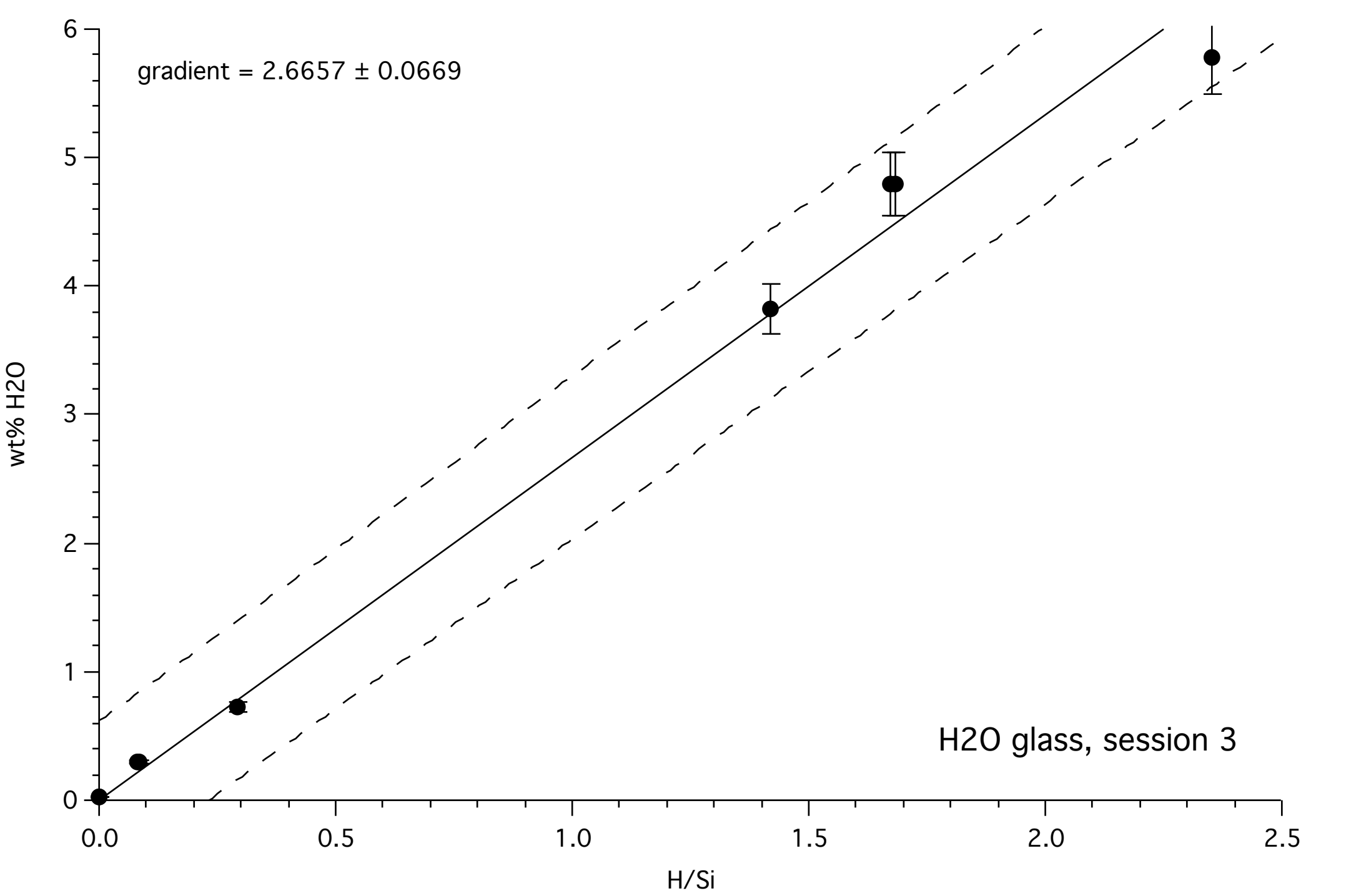
gradient = 2.6657 ± 0.0669
H2O glass, session 3
wt% H2O
H/Si
0
1
2
3
4
5
6
0.0
0.5
1.0
1.5
2.0
2.5

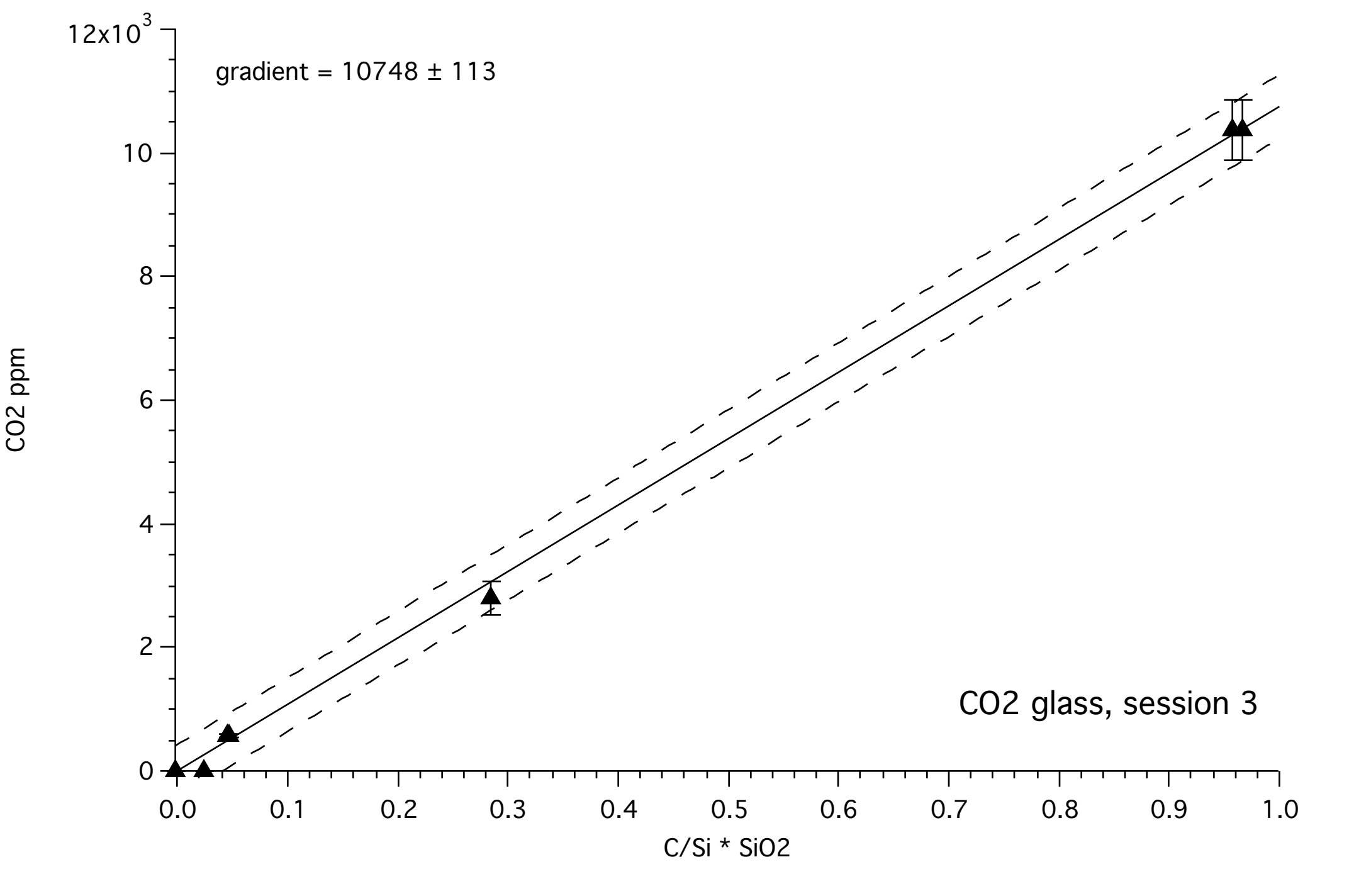
12x10^3
gradient = 10748 ± 113
10
8
6
4
2
0
CO2 ppm
0.0
0.1
0.2
0.3
0.4
0.5
0.6
0.7
0.8
0.9
1.0
C/Si * SiO2
CO2 glass, session 3